UNIVERSITY OF CALIFORNIA SAN DIEGO

Intravitreal Therapeutic Nanoparticles for the Treatment of Posterior Segment Ocular Diseases

A dissertation submitted in partial satisfaction of the requirements for the degree Doctor of Philosophy

in

Chemistry

by

Joel F. Grondek

Committee in charge:

Professor Michael J. Sailor, Chair
Professor Karen Christman
Professor Seth Cohen
Professor Daniel Donoghue
Professor Pieter Dorrestein
Professor Sylvia Evans

2022

The Dissertation of Joel F. Grondek is approved, and it is acceptable in quality and form for publication on microfilm and electronically.

University of California San Diego

2022

DEDICATION

To my son.

TABLE OF CONTENTS

LIST OF FIGURES

LIST OF TABLES

ACKNOWLEDGEMENTS

I would like to thank Professor Sailor and my committee for their support and guidance over the many years that have passed since we first met. I would also like to thank the many Sailor lab members, both past and present, and my who have help me along my journey. I would like to thank Professor Christman for making her laboratory and group members available to me for animal surgeries, for our work in MR imaging of myocardial infarction, and for always being open for questions and assistance. I would like to thank Dr. Freeman for helping to guide our retina project and donating the time and hands of several ophthalmology fellows who made this work possible. Also, for access to all the facilities and personnel. Finally, I would like to thank my wife and my family for all their love and support over the many years I have spent working to fulfill my personal and professional goals.

I would also like to acknowledge the contributions and efforts of my co-authors on the following chapters:

Chapter 2 is currently being prepared for submission for publication of the material. Grondek, J.F., Luo, C., Hu, D., Christman, K.L., Ruoslahti, E., and Sailor, M.J., Targeted Iron Oxide Nanoworms for Contrast Enhanced Magnetic Resonance Molecular Imaging of Fibrin Networks within Infarcted Myocardium. The dissertation author was the primary researcher and author of this material.

Chapter 3 is currently being prepared for submission for publication of the material. Grondek, J.F., Huffman, K., Cavichini, M., Warter, A., Kalaw, F.G.P., Lee, E.J., Fan, R., Cheng, L.,

Freeman, W.R., and Sailor, M.J., Treatment of Retinal Neovascularization in a Rabbit Model with a Fusogenic Porous Silicon Nanoparticle Containing Vascular Endothelial Growth Factor siRNA. The dissertation author was the primary researcher and author of this material.

VITA

Bachelor of Science in Biochemistry	Dec. 2002
Iowa State University, Ames, IA	
Master of Science in Biochemistry	Dec. 2004
Iowa State University, Ames, IA	
Doctor of Philosophy in Chemistry	March 2022
University of California San Diego, La Jolla, CA	

PUBLICATIONS

Grondek, J.F. and Culver, G.M. Assembly of the 30S ribosomal subunit: positioning ribosomal protein S13 in the S7 assembly branch. RNA. 2004 10(12):1861-6.

Dutcă, L., Jagannathan, I., **Grondek, J.F**. and Culver, G.M. Temperature-dependent RNP conformational rearrangements: analysis of binary complexes of primary binding proteins with 16S rRNA, J Mol Biol. 2007 386(3):853-6.

Kinsella, J.M., Ananda, S., Andrew, J.S., **Grondek, J.F**., Chien, M.P., Scadeng, M., Gianneschi, N.C., Ruoslahti E., and Sailor, M.J. Enhanced magnetic resonance contrast of Fe3O4 nanoparticle trapped in a porous silicon nanoparticle host. Adv. Mat. 2011 23(36) 248-53.

Joo, J., Cruz, J.F., Vijayakumar, S., **Grondek, J.F**., Sailor, M.J., Photoluminescent porous Si/SiO2 core/shell nanoparticles prepared by borate oxidation. Adv. Func. Mat. 2014 24(36), 5688-5694.

Grondek, J.F., Luo, C., Hu, D., Christman, K.L., Ruoslahti, E., and Sailor, M.J., Targeted Iron Oxide Nanoworms for Contrast Enhanced Magnetic Resonance Molecular Imaging of Fibrin Networks within Infarcted Myocardium, in preparation.

Grondek, J.F., Huffman, K., Cavichini, M., Warter, A., Kalaw, F.G.P., Lee, E.J., Fan, R., Cheng, L., Freeman, W.R., and Sailor, M.J., Treatment of Retinal Neovascularization in a Rabbit Model with a Fusogenic Porous Silicon Nanoparticle Containing Vascular Endothelial Growth Factor siRNA, in preparation.

ABSTRACT OF THE DISSERTATION

Intravitreal Therapeutic Nanoparticles for the Treatment of Posterior Segment Ocular Diseases

by

Joel F. Grondek

Doctor of Philosophy in Chemistry

University of California, San Diego, 2022

Professor Michael J. Sailor, Chair

Ocular therapeutic delivery affords challenges as unique as the diseases themselves. The human eye is anatomically compartmentalized, both within the organ itself and from the systemic vasculature typically used for drug delivery. Recent pharmaceutical developments have revolutionized the prognosis for ocular diseases, yet many therapies treating the posterior segment of the eye remain invasive and require frequent administration to maintain remission. Herein, we review the application of nanocarriers as intravitreally injected therapeutic delivery

vehicles working toward enhanced retinal uptake to further improve current therapeutic outcomes and for the development future therapies and we present a novel approach to the treatment of diabetic retinopathy and diabetic macular edema.

Chapter one provides introductory overview of the complex anatomy of the eye, routes of therapeutic administration, and current nanoparticle formulations designed to treat posterior segment diseases by intravitreal injection.

Chapter two demonstrates a novel application of fusogenic porous silicon nanoparticles for intravitreal delivery of vascular endothelial growth factor siRNA using a rabbit model for diabetic retinopathy and diabetic macular edema.

Chapter three summaries prior work focused on peptide targeted magnetic resonance imaging of myocardial infarction using a fibrin homing peptide. Here we demonstrate long circulating iron oxide nanoparticle chains call “nanoworms” can effectively target early fibrin associated with myocardial injury using a rat ischemia/reperfusion model.

Chapter 1

Introduction

1.1 Abstract

Diabetic retinopathy and age-related macular degeneration are two of the leading causes of blindness having a combined global prevalence surpassing 300 million people [1, 2]. In addition, glaucoma, retinitis pigmentosa, branch and central retinal artery and vein occlusions are just a subset of ocular diseases that can be treated but have no cure. While many of the recent advances in the treatment of ocular diseases have come from the development of novel therapeutics, it also apparent the development of alternative methods for therapeutic delivery will be a key component to widespread positive prognostic outcomes. The human eye is anatomically complex and offers a unique opportunity for the application of novel therapeutic delivery vehicles. Because the eye has barriers to systemic circulation similar to blood brain barrier direct injection is required to treat most posterior segment diseases. Intravitreal injection is the most common route of administration, yet most therapies are short lived and require repeat injections to maintain efficacy. This invokes the inherent risks associated with multiple, frequent intravitreal injections and of large therapeutic doses to offset the short intravitreal half-lives. Below we review the application of a wide variety of nanocarriers as intravitreally injected therapeutic delivery vehicles developed with the primary goals of enhancing retinal uptake and extending therapeutic windows.

1.2 Ocular Anatomy and Therapeutic Administration

1.2.1 Ocular Anatomy

To better understand intraocular therapeutic delivery it is useful to review the anatomy of the eye and the benefits and shortcomings of different routes of administration [3]. The eye can be viewed, for the most part, as an isolated system within the body. On a macroscopic scale the eye consists of two chambers (**Figure 1.1**). The posterior chamber, which extends from the choroid through the vitreous humor up to the lens, represents 80% of the eye's volume. The region from the lens to the cornea is called the anterior chamber. The reason for this distinction is two-fold. First, the anterior chamber contains the aqueous humor which is maintained by the vasculature of the ciliary process. The posterior chamber contains the vitreous humor and is maintained both the ciliary process and the retinal capillaries. Secondly, while there is nominal transfer of fluid from the vitreous to the aqueous, there is little to no propagation of anterior chamber aqueous fluid to the vitreous [4].

The eye is further isolated from systemic circulation by the blood-aqueous barrier and the blood retinal barrier [5, 6]. These barrier act in a similar manner to blood brain barrier by tightly regulating and protecting the intraocular systems. The ciliary epithelium of the blood-aqueous barrier is fenestrated for the movement of ions, small molecules and fluid but prevents the movement of large molecules between the choroidal vasculature and the aqueous humor. The ciliary body also functions to support the flux of fluid and waste from the vitreous and is primarily responsible for vitreous turnover. The posterior region of the vitreous is separated from the retina by the inner limiting membrane. Only water and molecules < 150kD can permeate from the vitreous through the inner limiting membrane by paracellular

movement [5]. The blood retinal barrier consists of two barriers. First, the inner blood retinal barrier (iBRB), formed by tight junctions between the retinal endothelial cells. The iBRB responsible for neural homeostasis and acts as an additional barrier between the vitreous humor and the retina. The second is the outer blood retinal barrier (oBRB) which made up by the retinal pigment epithelium (RPE) and Bruch's membrane [7]. The oBRB isolates the retina from the choroid vasculature and acts as a bidirectional transport. The oBRB brings glucose and other nutrients in form the choroid to support photo receptor function, modulates the release of water and electrolytes to maintain osmotic equilibrium, and aids in the removal of cellular waste.

1.2.2 Retina Structure

Understanding the basics of retina structure with help to appreciate its complexities. The retina itself can be subdivided into 10 layers (**Figure 1.2**) [8]. The RPE is considered the first layer. In addition to functions listed above, RPE absorbs scattered light which aids in visual acuity. The second layer is photoreceptor layer, which contains the rod and cone cells responsible for turning photons that have passed from the iris through the entire retina into electrical signals. Third is the external limiting membrane, semipermeable barrier made up the terminus of the Müller glial cells and of nerve fibers. The external limiting membrane helps to maintain the structural integrity of the retina and subdivides the neuronal photoreceptor layer from the outer nuclear layer which contains the photoreceptor nuclear body and is considered the fourth layer. The fifth layer is the outer plexiform layer and constitutes the region where the axons of the photoreceptor neurons contact the dendrites of the bipolar cells. The sixth

layer is the inner nuclear layer and contains the cell bodies of the bipolar neurons. The seventh layer is the inner plexiform where the axons of the bipolar cells contact the dendrites of the ganglion cells. The eight layer is the ganglion cell layer which houses the body of the ganglion neurons. The ninth is the nerve fiber layer. It contains the unmyelinated axons of the ganglion cells that act as the final neural output of visual information. Finally, the tenth layer is inner limiting membrane, which is made up of the basement membrane of Müller cells. Müller cells span from the external limiting membrane to the internal limiting membrane regulate neuronal activity through ion and neurotransmitter homeostasis. Additionally, there are two cell types not included above. First are the horizontal cells which transmit neural signals in between axons of the photoreceptors to the dendrites of the bipolar cells as a way concentrating signals. Second are the amacrine cells which play an indirect role in the connections between bipolar cells, ganglion cells, and other amacrine cells.

1.2.3 Routes of Ocular Therapeutic Administration

There are three common ocular therapeutic delivery routes: topical, systemic, and intravitreal, and several less-common routes discussed in brief below (**Figure 1.3**). Topical administration is the least invasive form of therapeutic delivery to the eye and is typically used to treat conditions in the anterior chamber, such as inflammation and infection [9]. For topical administration to be effective therapeutics must permeate the cornea to the aqueous humor, and thus are primary reserved for anterior segment delivery. This is limited to lipophilic therapeutic formulations, as proteins and hydrophilic molecules show little to no trans-corneal absorption. Topical administration results in the bioavailability of only 1-4% due to rapid

removal from the corneal surface by the lacrimal fluid, tear ducts, and absorption by the conjunctiva. Hydrophilic drugs have been successfully shown to penetrate the conjunctiva and reach the posterior segment by periocular movement, utilizing the fluid surrounding the exterior of the eye. These drugs can then diffuse through the sclera and have the potential to reach the choroid and retina, however the resulting therapeutic dose is generally <10%.

The second method is systemic. Administration is either oral or by injection (intravenous, intramuscular, subcutaneous) and used to deliver antibiotics to treat infection or small molecule inhibitors to treat elevated intraocular pressure. The therapeutics enter through the ocular artery to reach the choroidal capillaries. The intraocular penetration is limited by both the BRB, in the case of the retina, or the BAB for the anterior and posterior chambers, as previously discussed. This restricts systemic delivery to hydrophilic small molecular therapeutics.

The third method is by direct injection into the vitreous humor. The vitreous is an acellular structure and makes up ~80% of the volume of the eye. The vitreous is thought to give this internal cavity structural support and aid in homeostasis. Intravitreal injection (IVI) involves piercing the pars plana, a thin 4 mm band of the ciliary process between the iris and beginning sclera. The major benefit of this method is direct delivery of the therapeutic to the vitreous chamber while avoiding damage to the iris, lens, and retina for treatment of posterior segment disease. IVI allows for therapeutic injection by applying only topical anesthesia and is used for both small molecule and antibody drug delivery, and for drug eluting implants [10, 11].

Other injection sites are used as a method to reach the posterior chamber, choroid, and RPE that bypass the clearance from the lacrimal fluid on cornea that plagues topical administration. Extraocular injections consist of sub-conjunctiva, sub-Tenons, and retrobulbar. These injection sites are the most invasive but are clinically relevant and have been the focus drug delivery implant studies and can be used for extended drug release of hydrophilic small molecule drugs. Additionally, there are injections between the sclera and the choroid, suprachoroidal, and between the RPE and the photoreceptors, subretinal. Subretinal is the preferred method for studying gene therapy, as many inherited retinal diseases affect the photoreceptors and other delivery routes have been found to be ineffective.

1.3 Intravitreal Therapeutic Nanoparticles

Intraocular treatments require excessive therapeutic doses and continued repeat intravitreal injections to maintain remission which run the risk of intraocular inflammation, infection, and ocular hemorrhage [12]. Encapsulating drugs inside of nanoparticles can both extend the half-life and improve retinal penetration, reducing the required dose for disease remission. Herein, we explore vitreous nanoparticle formulations grouped by synthesis material (**Figure 1.4**) and discuss half-life, retinal up take and efficacy.

1.3.1 Vitreous Diffusion Studies

First we consider the structure of the vitreous and how it relates to particle size, composition and surface potential [13]. The vitreous is made up of >99% water; where collagen, hyaluronic acid, and peptidoglycans make up about 0.2% [14, 15]. In the vitreous, the

glycosaminoglycan hyaluronic acid, or hyaluronan, is highly cross-linked to itself and to collagen, where the highest density is found near the lens and lowest is adjacent to the retina. Type II collagen fibers, the most abundant subtype within the vitreous, are oriented conically anterior to posterior, where the posterior fibers anchor to the internal limiting membrane. There is also a high density of collagen fibers along the inner surface near the retina. The distance between collagen fibrils is on average ~ 2 mm, therefore the fibers themselves have little effect on molecular diffusion. It has been found that despite the viscous nature of the vitreous humor, diffusion rates of small molecules are on the order of free molecules in solution. Barza *et al.* looked at nano and microparticles dynamics in both the vitreous and retina [16]. They synthesized liposomes containing ^{125}I-p-hydroxybenzamidine-dihexadecylphosphatidylethanolamine (^{125}I-BPE) hydrated with ^{51}Cr-EDTA with and without cholesterol. They achieved monodispersed particles with diameters of 60 nm, 60 nm with cholesterol, 400 nm, or 600 nm with cholesterol and they found liposomes with cholesterol resulted in ^{51}Cr-EDTA payloads being detected in the vitreous for 24 and 29 days, for 60 nm and 600 nm respectively, verses 4 and 8 days for the 60 nm and 400 nm cholesterol free particles in normal rabbit eyes. They also found ^{125}I-BPE lipids could be detected for ~2-fold longer than ^{51}Cr-EDTA and eyes with larger liposome retained ^{125}I-BPE twice long both with and without cholesterol, suggesting smaller particles were eliminated at a faster rate. Finally, they found all particles injected into bacterial endophthalmitis induced eyes were eliminated at almost a 4-fold faster rate; suggesting the disease/disease model plays a pivotal role in nanoparticle pharmacokinetics. Sakurai *et al.* studied the half-life and biodistribution of intravitreal injected fluorescein loaded polystyrene spheres with diameters of 2 μm, 200 nm and 50 nm in healthy

rabbit eyes [17]. By measuring fluorescence intensity, they found the vitreous $t_{(1/2)}$ to be 5.4 ± 0.8 days for 2 µm, 8.6 ± 0.7 days for 200 nm, and 10.1 ± 1.8 days for 50 nm. For reference free sodium fluorescein had a $t_{(1/2)}$ of 7.8 ± 0.7 h. Fundus images of the retina showed a discrete deposit of 2 µm particles in the vitreous post-injection and a homogenous haze of 200 nm particles. The 200 nm polystyrene spheres could be detected in the retina one month after injection, however, 2 µm particles were no longer observed, suggesting an upper size limit on retinal uptake. Peeters *et al.* expanded on this study by testing several nanoparticle materials and diameters for diffusion in bovine vitreous *ex vivo* [18]. The particles were measure for differences diffusion by fluorescence recovery after photobleaching (FRAP). The naked polystyrene particles appeared to adhere to the collagen fibers and did not freely diffuse. Their zeta potential ranged from -42 to -54 mV, and it was hypothesized that a negative surface potential would allow for free diffusion due to the hyaluronic acid within the vitreous. It was hypothesized the polystyrene particles were attracted to the collagen via hydrophobic interactions. When coated with polyethylene glycol (PEG) these same particles were found to freely diffuse for all diameters < 500 nm, with zeta potentials of -8 to -17 mV. Another significant finding was a minimum of 16.7 mol% 1,2-distearoyl-sn-glycero-3-phosphoethanolamine (DSPE)-PEG was required for stability and free diffusion, where 9.1% or less was insufficient. Another group looked at amphipathic nanoparticles consisting of polyethyleneimine (PEI), glycol chitosan (GC), hyaluronic acid (HA), and human serum albumin (HAS), and three hybrid particles consisting of PEI/GC, GC/HAS, and HSA/HA, with discrete sizes ranging between 230 nm and 350 nm [19]. Interestingly, all particles showed some level of accumulation on the inner limiting membrane of naïve rat eyes, where PEI showed the least

amount of movement. However, only particles with a negative zeta-potential (HA and/or HSA) were able to pass through the inner limiting membrane, independent of their hydrodynamic radius, and were found to permeate throughout the retina. These results were later corroborated by Xu *et al* [20]. They confirmed PEG coated polystyrene particles of 500 nm or less will freely diffuse through the bovine vitreous *ex vivo.* PEG coated polystyrene particles of 1190 nm also would not diffuse, nor would polystyrene particles coated in primary amines. Using these data, the authors estimated the mesh size of the bovine vitreous to be ~550 ± 50 nm.

These studies indicate the upper size limit to free intravitreal diffusion of ~600 nm. Particles with large negative surface potentials and particles with positive potentials surrounded by PEG can freely diffuse. Particles larger than 1 μm and/or particles with positive potentials will remain localized within the vitreous, unless PEGylated. Finally, as illustrated by the work of Barza *et al.* discussed above, it is important to consider the effects of the disease, or disease model, itself with regard to *in vivo* nanoparticle half-life and efficacy. However, in studies discussed below, researchers have found particles with zeta potentials ranging from +15 to +35 mV also have high retinal uptake, even in absence of PEG, yet the size limitation appears to prevail. It is accepted that nanoparticles need a positive surface potential to fuse with the negatively charged cell membranes. This nanoparticle surface potential dichotomy suggests vitreous diffusion and retinal uptake might be more complex than previously assumed.

1.4 Liposomes

The first nanoparticle formulation we will discuss are liposomes as they are perhaps the most extensively studied and in turn, they represent the largest fraction of U.S. Food and Drug

Administration (FDA) approvals for nanoparticle therapeutic vehicles [21]. Liposomes have been widely investigated for the last half century for their potential as drug delivery vehicles [21-23]. Most recently liposome utility has realized as the delivery vehicle for two of the SARS-COVID-2 vaccines. Liposomes are phospholipid vesicles that self-assemble into a spherical bilayer in an aqueous environment, analogous to cell membranes, though unilamellar and multilamellar vesicles are also possible. Many methods have been developed for liposome synthesis and the most common of these in practice is thin-film hydration. Here, the desired lipid formulation is combined in a volatile solvent, typically chloroform, followed by evaporation to create a thinly layered film. An aqueous phase, frequently containing the therapeutic agent of interest, is then added and liposomes spontaneously form from rehydration of the film layers. The final liposome diameter can be controlled by mechanical means such as sonication, extrusion, lyophilization, freeze fracture, or combination thereof. The physical characteristics of liposomes can be modulated by selection of individual constituent parts and varying their respective mol ratios. Some variations include: the length, composition and number of hydrocarbon chains; the charge ratios of the polar head groups, as charge optimization can enhance both stability and cell uptake; the addition of cholesterol to hydrophobic inner region of the bilayer to aid in lipid packing and enhance stability; the incorporation of pegylated lipids which have been shown to improve biocompatibility; and finally the incorporation of lipids that contain a chemical functional group for ease of conjugation to fluorophores or biomolecules. While cholesterol is important for stability, excluding cholesterol and optimizing both surface potential and lipid composition, liposomes can be designed to fuse with cell membranes thereby avoiding the issue of endosomal escape or lysosomal degradation. Currently, there are 20 FDA approved

liposome formulated therapeutics including the recent COVID-19 vaccine. Although at present there are no approved liposome formulations for intraocular delivery, in 2002 Visudyne©, an intravenously injected phospholipid formulation for verteporfin delivery, was FDA approved for photodynamic therapy to treat choroidal neovascularization (CNV).

Early studies of intravitreal liposome drug delivery began by encapsulating antibiotics to extend their window of efficacy to treat endophthalmitis, which is intraocular inflammation. Clindamycin [24] and ciprofloxacin [25] intravitreal half-lives were extended from a few hours to a few days after liposomal coating in healthy rabbits. Later the focus turned to liposomal delivery of antiviral drugs to combat cytomegalovirus (CMV). Bourlais *et al*. demonstrated a combined therapy of free ganciclovir and liposome encapsulated ganciclovir, with an encapsulation efficiency (EE) of 41%. This approach extend the therapeutic window from ~2.5 days to 30-45 days [26]. Cheng *et al.* reported liposomes developed for intravitreal injection (IVI) [27]. The authors synthesized a lipid conjugated form of ganciclovir (HDP-ganciclovir) that were incorporated into liposomes. This formulation was tested *in vitro* against herpes simplex virus type-1 and human cytomegalovirus infected cells, which resulted in an IC_{50} of 0.02 and 0.6 µM, respectively. An IC_{50} between 1-10 µM is considered worthy of advancement in early drug screening [28]. Using an *in vivo* rabbit model, the HDP-ganciclovir liposome showed no toxicity by IVI at 10x the treatment concentration of 0.2 µM and resulted in protection of the retina up to 6 weeks post-treatment against IVI herpes simplex virus type 1. Claro *et al.* evaluated foscarnet, an anti-viral CMV inhibitor [29]. Lecithin is a naturally occurring mixture of phosphoglycerides including phosphatidyl-choline, -ethanolamine, -inositol, and -serine. The foscarnet liposome EE was 64 ±

1.0%. The particles were tested in healthy rabbit eyes and foscarnet levels in the vitreous and retina were found to be 2.5x and 5x higher, respectively, than free drug at 72 hr.

Over the last few decades there has also been great interest in the intravitreal delivery plasmid DNA (pDNA) for gene therapy. Free plasmids have difficultly penetrated the inner limiting membrane and viral capsids, e.g. adeno-associated virus (AAV), can induce intravitreal inflammation [30]. Toward this end, Kawakami *et al.* loaded luciferase pDNA into liposomes and optimized the charge ratios of pDNA electrostatically bound to cationic lipids to measure transfection efficacy in naïve rabbit eyes [31]. Peak luminescence was measured at day 3 with 85 mg plasmid loaded onto 1,2-di-O-octadecenyl-3-trimethylammonium propane (DOTMA)/cholesterol particles. Elevated luminescence was measured in the aqueous humor, ciliary body, lens, vitreous and retina. The authors calculated relative charge ratio of plasmid to cationic liposome and found 1.0:2.0 (- : +) to have the highest level of luciferase activity. Charge ratios of both 1.0:1.5 and 1.0:2.5 plasmid to cationic liposome resulted in lower levels of transfection. Alqawlaq *et al.* designed and tested liposome-based nanoparticles incorporating pH responsive polymers for optimal endosomal release [32, 33]. Different liposome formulations were assessed for *in vivo* distribution based on surface charge for the delivery of pCMV-td-Tomato DNA [33]. The surface charge was modulated with the addition of different ratios of 1,2-dioleoyl-sn-glycero-3-phosphoethanolamine (DOPE). All formulations resulted in particles 150-220 nm with a surface charge exceeding +30 mV. The transfection results showed the formulations with higher concentrations of positively charged DOPE had higher transfections efficiencies, with the optimum formulations resulting in ~50% of the efficiency the

lipofectamine control, $p < 0.05$. Using healthy mice, the particles were shown to accumulate from the inner limiting membrane through the ganglion cell layer of the retina, supporting the potential for intraretinal pDNA delivery.

Fattat *et al.* conducted one of the first studies looking at intravitreal liposomal RNA interference (RNAi) delivery having loaded isotopically labeled 16-mer oligo-thymidylate (^{33}P-pdT16) as a model phosphodiester oligonucleotide construct. The authors tested for biocompatibility, biodistribution and release after intravitreal injection in a naïve rabbit model [34]. The liposomes were formed by thin-film hydration, extrusion to 0.2 μm filters, followed by repeated free-thaw loading of the oligo under liquid nitrogen. The liposomes were measured to be 150 nm in diameter and had an EE of 18%. *In vivo* pharmacokinetic studies showed a $t_{(½)}$ of 7 days for the liposomes, as compared to < 6 hours for free oligo, with intact oligos found 14 days after administration. Liu *et al.* later evaluated VEGF receptor-1 (VEGFR1) siRNA in a hybrid of HA and protamine (small nuclear proteins with abundant arginine), that was applied to a liposome formulation containing PEG2000 [35]. The resulting nanoparticles appear polydisperse by TEM with a DLS size of 131.9 nm and zeta potential of +19.73 mV. The EE, however, was found to be > 95%. The nanoparticles were then injected one day after laser-induced choroidal neovascularization (L-CNV) in rats and found to reduce the area of CNV as compared to saline control at day 14, $p < 0.001$. Histology showed uptake of particles into the ganglion cell layer at 6 hr and predominately in the photoreceptor layer at 24 hr. Another group looked at the charge effects on Intravitreal injected liposome siRNA nanoparticles [36]. The authors also evaluated PEG2000 conjugated particles with zeta potentials ranging from +45 mV to -30 mV and a

hydrodynamic size of ~70 nm. They also found particles with +35 mV or +45 mV resided within the eye the longest having ~10% and ~35% remaining at 24 hr in healthy mice, while the particles with more negative surface potentials were >90% absent at 6 hours. Histology of the eyes injected with +35 mV particles showed at 6 hours most particles at the retinal inner limiting membrane and within the ganglion cell layer, and smaller fraction penetrating up the photoreceptor layer. At 24 hr the particles could only be detected a low level within the photoreceptor layer. In a recent study the authors tested a similar liposome formulation as describe above for siRNA knockdown of RNA-binding protein with multiple splicing (RBPMS) in the retina or RPE65 siRNA in the RPE/choroid in naïve mice [37]. After enucleation, separation of the retina from the RPE/choroid the authors found particles with +31 mV had the highest suppression RBPMS, ~25% *in vivo.* They did not see significant knockdown of RPE65, suggesting the nanoparticles do not reach the RPE, but reside mostly in the ganglion cell layer, confirmed by Cy5-siRNA histology.

Intravitreal liposomes have also been tested for the treatment of uveitis, inflammation of uvea, the region containing the choroid in the posterior segment, and the iris and ciliary body of the anterior segment. The immunosuppressive factor vasoactive intestinal peptide (VIP) was loaded into liposomes and studied in rat model of subcutaneous lipopolysaccharide endotoxin induced uveitis (EIU) [38]. The liposomes had diameters between 300 and 600 nm with an EE of 37%. Intravitreal release of VIP from liposomes in healthy rat eyes showed a burst release, however VIP was 15-fold higher at 24 hours in the liposome injected eyes verses free VIP, p = 0.03. In addition, no inflammation was observed from the empty liposomes. 24 hr after

injection a 2-fold reduction of EIU clinical score for inflammation was observed in the EIU rat eyes with VIP liposomes, p = 0.0002, whereas the free VIP control had no effect. This research group also examined rhodamine-conjugated liposomes loaded with VIP for biodistribution in healthy rats [39]. The resulting particle had the same size distribution with a zeta potential of -0.9 mV. The biodistribution was characterized at 24 hours and 14 days after injection. At 24 hours post injection majority of nanoparticles were found in the vitreous, taken up by resident ocular macrophages, and within Müller glial cells, resulting in a retinal distribution constrained to the inner limiting membrane. No uptake was found in the anterior segment. These data suggest the IVI VIP liposome nanoparticles may be an effective way to treat uveitis. A rat model of experimental autoimmune uveitis (EAU) was used to test liposome loaded tacrolimus, an immunosuppressive bacterial isolate [40]. The liposomes were synthesized using supercritical reverse phase evaporation (SCRPE) [41]. Although the specific phospholipid used was not provided, an optimal mol ratio of 10:1, lipid to cholesterol, was given liposomes, and the resulting liposomes were 202 ± 3 nm [40]. The particles had a tacrolimus EE of 27%. Rhodamine conjugated liposomes were shown to diffuse from the vitreous through the inner limiting membrane to the outer nuclear layer within 24 hr and remained detectable for 21 days, demonstrating prolonged retention within the retina. Vitreous levels of tacrolimus were reduced by 90% within 24 hr but remained above 50 ng/mL for 14 days, as compared to only 24 hours for free tacrolimus. Clinical scores of EAU showed effective suppression of ocular inflammation with greater efficacy of the nanoparticle formulation over free tacrolimus. Finally, HA-modified liposome coated red fluorescein (RITC)-chitosan nanoparticles were studied for retinal distribution after IVI [42]. HA has a natural affinity to cell surface adhesion receptor CD44

and has been used for targeting tumors. The chitosan nanoparticles were synthesized by first dissolving chitosan 0.15% (w/v) in 1% acetic acid and conjugating to RITC to its primary amines. Liposomes were rehydrated with the RITC-chitosan solution and with were covalently linked with HA NHS and EDC [43]. The resulting particles (HA-LCS) had a diameter of 320 nm and a surface charge -25 mV [42]. Chitosan (CS) only particles and liposome chitosan (LCS) particles had diameters of ~190 nm and zeta potentials of +36 mV and -11 mV respectively. Intravitreal injection experimental autoimmune uveitis (EAU) rats showed that the CS particles remained within the vitreous, where the LCS particles penetrated the inner limiting membrane, but resided mostly in the ganglion cell layer, while the HA-LCS particle could be see dispersed throughout the retina to the RPE cell layer at 12 hours. Histology further demonstrated a colocalization of HA-LCS particles with CD44 receptors on the RPE cells. After 7 days HA-LCS retained a RITC fluorescence intensity of ~75% in the RPE/Choroid layer, suggested the potential for sustained drug release.

Choroidal neovascularization (CNV) occurs in diseases such as wet age-related macular degeneration (AMD), where newly forming choroidal blood vessels can penetrate the RPE layer and damage the photoreceptor layer. Doxorubicin (DOX), used to suppress neo vessel growth, was encapsulated within a liposome and targeted the tyrosine kinase receptor EphA2 shown to be expressed on tumor neovascular cells as a potential treatment for CNV [44]. YSA is a 12–amino acid peptide consisting of YSAYPDSVPMMS that has been shown to selectively bind EphA2. The resulting particles were ~110 nm in diameter size and yielded an EE > 95% for DOX. The particles were tested by IVI in a rat model of L-CNV and were shown at week 2 to have a

reduced area of CNV as compared to non-targeted DOX particles, $p < 0.001$, and saline control, $p < 0.001$. Lee *at al*. investigated liposomes optimized for retinal penetration by looking at different phospholipid mol ratios [45]. The diameters ranged from 116 nm to 135 nm and surface charge from -1.1 mV to +46.8 mV. Here the authors found the formulation LDP20 with a final diameter of 118.4 nm and zeta potential +19.7 mV resulted in the highest level of retinal uptake. Hydrophobic DiI fluorophore labeled LDP20 were found to persist in naïve mouse retina at 5 days, with most of the fluorescence originating from the inner limiting membrane to the outer plexiform layer at day 3. Hydrophilic carboxyfluorescein (CF) loaded particles had limited retinal uptake, however when CF covalently linked to lipids a similar level of retinal penetration at 3 days as DiI describe above, where the fluorescence resided mostly in the RPE at day 7. Finally, fluorescently labeled ranibizumab, an anti-vascular endothelial growth factor (VEGF) antibody, was lipid conjugated, incorporated into the LDP20 formulation, and tested in a mouse model of L-CNV. The liposome delivered ranibizumab was present in the retinal for two week and had higher retention than free fluorophore labeled ranibizumab, $p < 0.001$, though no efficacy data was mentioned. The authors conclude their liposomes do not remain intact, rather they dissociate at the inner limiting membrane and permeate through the retina likely by lipid-endogenous cell membrane interactions and/or transport.

1.5 Solid Lipid Nanoparticles

Solid lipid nanoparticles (SLNs) are a broader class of lipid-based particles where the core is predominately a hydrophobic lipid matrix and is surrounded by an ionic lipid or surfactant coating [46, 47]. A major strength of SLN synthesis methods is that they allow for the

incorporation of many different biologically derived lipids resulting in innate biocompatibility. Advantages of having a relatively solid matrix core, when compared to common liposomes, are increased core stability, extended therapeutic release, and the potential for higher payload from hydrophobic drug stacking. Typical methods for synthesis include solvent emulsification-evaporation, homogenization by sonication, high shear, or high pressure, and microemulsions. Solvent emulsification-evaporation is one of the more widely used synthesis methods, where lipids are dissolved in an organic solvent that is immiscible in water. This mixture is then emulsified in an aqueous phase. The solvent is then evaporated, and nanoparticles precipitate out of solution. The second common method is melt-emulsification which requires heating the lipids at or above their melting temperature followed by emulsification in an aqueous phase by high shear or sonication. A sub-class of SLNs called niosomes which are non-ionic surfactant-based 'liposomes' where the phospholipids head groups are substituted by neutrally charged synthetic groups or saccharide moieties [48]. SLNs as a whole are attractive to industry due to the relative ease of manufacture and scaleup, however the major disadvantages are low hydrophilic drug loading capacities, polydispersity in both size and colloidal structure, and the possibility of undesirable lipid phase transitions that can lead to instability [46, 47].

Apaolaza *et al.* evaluated SLNs as DNA delivery vehicle for gene therapy of X-linked juvenile retinoschisis (XLRS) from a mutation in the *RS1* gene encoding retinoschisin [49]. Protamine and dextran (DX), or hyaluronic acid (HA) were used to complex a plasmid containing the *RS1* gene prior to SLP encapsulation by solvent emulsification-evaporation [50] and tested for transfection efficiency and therapeutic efficacy in *Rs1h* deficient mice [49]. The particle diameters

were 230 ± 21 nm for DX and 223 ± 20 nm for HA, with zeta potentials of +43.0 ± 0.4 mV and +31.5 ± 1.1 mV, respectively. The SLPs using HA induced a higher transfection level than DX for both a GFP and retinoschisin expressing plasmids *in vivo* in *Rs1h* deficient mice at two weeks measured by fluorescence histology. HA particles also resulted in a significant higher increase in the thickness of both retina and outer nuclear layer as compared to wildtype and untreated Rs1h-deficient controls, $p < 0.05$ for each.

Abrishami *et al*. tested SLNs for the intraocular delivery of diclofenac sodium, an analgesic and anti-inflammatory drug [51]. Using a melt-emulsification method resulted SLN size a 172.7 ± 6.3 nm with a zeta potential of -0.9 ± 2.0 and a diclofenac EE of 95%. The particles were injected into naïve rabbit eyes and the drug concentration was measured over 48 hours. The drug concentration in the particle injected eyes was significantly higher than the free drug eyes at 4 hours, $p < 0.05$. At 12 hours the drug concentration in both eyes had dropped >90%..

Two types of nanoparticles were evaluated for vitreous compatibility and release of the antiangiogenic receptor tyrosine kinase inhibitor sunitinib, SLNs and polymeric nano-capsules (NCs) [52]. The SLNs were prepared by microemulsion followed by emulsification-evaporation. The resulting particles were injected into healthy rabbits at 1 and 10 mg/mL concentrations of sunitinib and assessed 26 days after injection. It was found that the NCs induced retinal damage, as measured by a decrease in amplitude by electroretinogram (ERG), the animals had posterior lens opacification, and observed intraretinal edema. For the SLNs, both the ERG and histology were comparable with the control eyes, supporting the SLN formulation as a viable sunitinib intraocular delivery vehicle.

The chemotherapy drug etoposide was loaded into SLNs with a formulation optimized by computer modeling with Box-Behnken design of the constituents to generate the chemical ratio using the variables of particle size, polydispersity index (PDI), and EE [53]. First several reagents were prescreened for etoposide solubility and stability, and after modeling it was determined that a lipid mixture at 4% w/v of Gelucire 44/14 and Compritol ATO 888 in the ratio of 3:1 was ideal. Using melt-emulsification and ultrasonication technique they obtained a diameter of 239.43 nm, PDI of 0.261 and EE of 80.96%. The particle formulation was tested *in vivo* by injecting 100 µL of etoposide alone or nanoparticle loaded etoposide by IVI into healthy rat eyes, however because the high end of the vitreous volume of a rat eye is close to 20 µL, it is difficult to draw conclusions from their data using this approach.

Qin *et al.* evaluated niosomes optimized for plasmid delivery and tested the particles *in vivo* gene expression [54]. The niosomes were synthesized by solvent emulsification–evaporation and pCMS-EGFP, similar to green fluorescent protein (GFP), was added to each particle formulation for electrostatic loading. Interestingly the plasmid-HA-niosomes, which had a ~290 nm diameter, 0.545 PDI, and –41 mV zeta potential, exhibited the highest transfection efficiency both in ARPE-19 cell culture and by intravitreal injection into naïve rats. Puras *et al.* also studied niosomes as intraocular transfection delivery vehicles synthesized by solvent emulsification–evaporation [48]. The resulting particles had diameters ranging from 151 nm to 280 nm and zeta potential from +42 mV to +53 mV depending on composition. pCMS-EGFP was then electrostatically attached to the particle surface. *In vitro* transfection efficiency increased with increasing number of cationic lipids in both HEK-293 and ARPE-19 cells, with comparable

transfection efficiency to lipofectamine in ARPE-19 cells with the highest ratio of cationic lipids to DNA at (15:1 w/w). Particles with this same ratio were then tested by intravitreal injection into healthy rats. EGFP expression was found in the ganglion cell layer, inner plexiform layer, and inner nuclear layer and attributed to Müller cell uptake by histology. No expression was seen from the injection of free plasmid. This same group then looked at the effects of using protamine to aid in plasmid loading [55]. They tested different ratios and found that 1:1:5 protamine, plasmid, niosome gave the optimum formulation for plasmid binding and release by electrophoresis. This ratio resulted in particles of ~150 nm in diameter and +40 mV. These particles were tested against the previously described particles without protamine and having a plasmid to niosome ratio of 1:15 in ARPE-19 cells for in vitro expression of GFP. The protamine particles resulted in slightly better uptake by cell number, but almost 2-fold higher fluorescence per cell, suggesting better nuclear delivery with protamine.

1.6 Synthetic Polymer Nanoparticles

1.6.1 PLGA

Poly(lactic-co-glycolic acid) (PLGA) is one of the most widely studied polymers for therapeutic applications and has been approved for used by the FDA since 1989 [56], and the intraocular dexamethasone implant Ozurdex© was FDA approved in 2009. PLGA is attractive because its hydrolysis leads to monomers of lactic acid and glycolic acid which are intermediates in the tricarboxylic acid, or Krebs cycle, thus making the polymer highly biocompatible. PLGA nanoparticle synthesis methods can be designed to incorporate either hydrophobic or hydrophilic therapeutics. The most common method for loading hydrophobic

drugs is emulsification-solvent evaporation. Both PLGA and the drug of interest are dissolved in an organic solvent, e.g., dichloromethane or methylene chloride. The drug/polymer mixture is then added to solution containing a surfactant and water, followed by homogenization or sonication, and solvent evaporation. An extension of this technique is called the double emulsion method and allows for encapsulation of hydrophilic drugs. Here the drug is mixed with a surfactant in an aqueous phase and is then mixed by homogenization or sonication with an organic phase containing PLGA, followed by the addition to an aqueous phase containing polyvinyl alcohol (PVA). Limitations of PLGA based nanoparticle systems tend to burst release, have multiphasic drug release profiles, and aggregation. These problems complicate therapeutic biodistribution. Secondly, there have been issues with manufacturing of generic PLGA based drugs due to the complexities and proprietary nature of the formulation and synthesis processes. Over the last 10 years the FDA has been developing programs and provided funding specifically to address this, and to better understand and characterize the properties of PLGA [57]. Despite these shortcomings there is still considerable interest in the use of PLGA hybrid nanoparticle systems for intravitreal drug delivery.

Bejjani *et al.* sought to evaluate the use of PLGA nanoparticles as vectors for gene delivery in ARPE-19 cells and healthy rats [58]. The plasmids pIRES-EC-GFP or pDs-Red2-Nuc were loaded in to PLGA by double emulsion. The final particles with a diameter of 643 ± 74. Gene expression was observed *in vitro* for both plasmids after 48 hours and lasting up to 10 days. pDs-Red2-Nuc expression was observed within the RPE cells as soon as 4 days after intravitreal

injection and was predominately localized within the RPE cell layer at 7 days, with fluorescence intensity highest within the nuclei.

The anti-inflammatory corticosteroid drug dexamethasone (DEX) was encapsulated with PLGA, 50% w/w, by emulsification-evaporation [59]. Injection into a rat model of L-CNV demonstrated a dose dependent effect on reducing disease severity measured after 14 days by fluorescein fundus examination. The particles exhibited an initial burst release of DEX followed by a sustained 2 to 4 mg/L release form days 7 to 28, with no detectable retinal toxicity. Zhang *et al.* found similar pharmacokinetics in healthy rabbit vitreous that showed sustained release of DEX for 7 weeks, maintaining a concentration of 3.85 mg/L for the >30 days [60].

Zhang *et al.* studied the delivery of DNA plasmids coding for the co-expression of a short hairpin RNA, shown to inhibit hypoxia-inducible factor 1a (HIF-1a), and GFP as a transfection reporter [61]. The particles were 303.7 ± 38.5 nm with a zeta potential of -8.91 ± 3.2 mV. The particles were then tested for efficacy using a rat model for L-CNV. GFP expression was shown to predominate in the RPE and persisted for 4 weeks. The areas of CNV leakage were smaller in the nanoparticle group as compared to naked pDNA, $p < 0.01$, and the thickness of CNV was less as determined by histology, $p < 0.01$, with no signs of toxicity. These data show the potential for PLGA particles as intravitreal transfection agents and the efficacy of the HIF-1a inhibitory hairpin RNA in reducing angiogenesis in this model of CNV.

The epidermal growth factor receptor tyrosine kinase inhibitor 4-(3-chloroanilino)-6,7-dimethoxyquinazoline (AG1478) was loaded into PLGA nano- and microparticles and studied by intravitreal injection in a rat model for optic nerve crush injury [62]. The particles were

synthesized by single emulsion solvent evaporation [63]. The nanospheres had a mean diameter of 359 ± 54 nm and microspheres were 2.56 ± 1.90 µm. The EE of AG1478 in was 79% for nanospheres and 67% for microspheres. The nanospheres exhibited an *in vitro* burst release followed by a zero-order release over 150 days and the microspheres showed a burst release followed by a lag phase, and then a zero-order release extending from 25 days to over 250 days. The nanosphere showed a longer residence within the rat vitreous, up to 4 weeks as compared to 2weeks for the microspheres and the nanospheres had increased efficacy in inducing nerve fiber growth. The author mention difficultly with the injection of microspheres might have influenced these comparative results. However, these data support the potential for intravitreal drug delivery for optic nerve regeneration.

Connexin43 mimetic peptide (Cx43) has been shown to be a neural connexin antagonist that can reduce connexin induced vascular leakage and ganglion cell death after retinal ischemia [64]. Intravitreally injected PLGA encapsulated Cx43 nano- and microparticles were tested for ganglion cell protection in a retinal ischemia-reperfusion rat model [65]. The resulting particles were ~113 nm and ~9 µm, with Cx43 EEs of 70% and 97%, respectively. *In vitro* Cx43 release showed a triphasic profile over a period of up to four months. The nanoparticles and free Cx43 both showed a significant preservation in retinal ganglion cell density for 28 days when compared to the no ischemia, and ischemia only controls, $p < 0.05$. The microparticles showed no significant benefit when compared to the ischemia only cell densities. The nanoparticle group also resulted in a significant reduction of Cx43 upregulation at 28 days, $p < 0.05$.

Zhang *et al.* encapsulated bevacizumab in PLGA by double emulsion to study the potential for sustained release [66]. The final particles had a hydrodynamic radius of ~133 nm, EE of 80% and loading efficiency of 6.8% (w/w). The PLGA-bevacizumab particles had a maximum bevacizumab concentration at day 6, as compared to day 1 for free bevacizumab. The particles were also shown to reduce neovascularization in a mouse model of oxygen-induced retinopathy as compared to both the control and the free bevacizumab animals.

A connexin43 mimetic peptide was encapsulated in PLGA nanoparticle by double emulsion [67]. No particle size data was given. The resulting particles were tested by IVI as a therapy for light induced damage using a rat model. The nanoparticles, free peptide, or saline control were injected at 2 hr after the onset of light damage and the animals were monitored by ERG, optical coherence tomography (OCT), and postmortem histology. The nanoparticle animals retained higher ERG amplitudes and maintained thicker outer nuclear layer and choroid for up to 2 weeks post treatment. Histology sections presented show FITC fluorescence at 30 min post injection within the choroid that authors attribute to FITC labeled particles. They also show particles within the ganglion cell layer near the inner limiting membrane, which are more representative of retinal nanoparticle uptake within this time frame.

PEG-PLGA conjugated to the cyclic RGD integrin targeting peptide were combined with additional PLGA and dissolved DEX [68]. This solution was then emulsified into nanoparticles in the presence of PEI in 1% PVA, followed by solvent evaporation [68]. The anti-VEGF antibody bevacizumab was then electrostatically loaded onto the particle surface [68]. The hybrid particle was ~214 nm in diameter and a neutral zeta potential. The particles were intravitreally injected

into a rabbit model of L-CNV 4 weeks after disease induction. The disease progression was then imaged 4 weeks later by fluorescein fundus angiography. Particles containing only DEX showed a fluorescence leakage level of 62.53 ± 9.66%, where DEX + bevacizumab particles were 27.17 ± 8.82%, and cRGD + DEX + bevacizumab 12.58 ± 3.12% as compared to no-particle, but with disease control animals. These data demonstrate the combination therapy is better than DEX alone, and cRGD targeting further increases efficacy

1.6.2 Dendrimers

Dendrimers were first discovered in 1978 and named in Greek for their *dendron*, "tree" or "branch", morphology [69, 70]. They consist of highly branched, globular polymers. Dendrimers are typically given the prefix G for "generation" followed by a number. This equates to the rounds of synthesis used in the formulation of the dendrimer, with each generation marking a branching point for the subsequent generation. The specificity of the synthesis process lends to monodispersed nanoparticles. The synthesis methods and polymers used are very diverse, and by in large beyond the scope of this review. However, one of the most frequently used dendrimers, poly(amidoamine) (PAMAM), and synthesis method will be discussed in brief. PAMAM is synthesized by the divergent method starting from ammonia or ethylenediamine initiator. Each generation of the divergent method involves the activation of a functional group on the surface, followed by the addition of branching monomer subunit. Here there are subsequent additions of methyl acrylate onto a primary amine (and subsequently secondary amine), followed by the addition of ethylenediamine to each surface ester. This process is continued until the desired nanoparticle dendrimer size is obtained. One major advantage of

the divergent process is the final surface layer can be modified with an alternative functional group for further conjugation chemistry. One of the major disadvantages of dendrimers is *in vivo* toxicity. PAMAM, for example, is cytotoxic and can cause hemolysis due to the terminal amine groups, however work has been done to study effects of size, generation and to further functionalized these groups to mitigate this toxicity [71].

PAMAM (G3.5) and PAMAM (G4.5) were covalently linked with DEX and Alexa Fluor 488 and studied in healthy rats [72]. The particle synthesis resulted nanoparticles with hydrodynamic diameter of 131.8 ± 4.1 nm for G3.5 and 145.1 ± 9.2 nm for G4.5 with zeta potentials of -54.9 mV and -57.8 mV, respectively. Intravitreal injection of both formulations showed a decrease in fluorescence of ~50% at 4 hours in the vitreous and ~80% at 4 hours in for the retina, but with ~8 fold greater uptake of G3.5 into the retina, and retention for ~24 hours.

PAMAM (G6) was electrostatically complexed with neurotrophin 4 (NT4), a 55 kDa growth factor demonstrated to aid in photoreceptor rescue [73]. The NT4-PAMAM particles were determined to be 18 ± 5 nm. *In vitro* PBS NT4 release showed a constant release ~135 µg/L for 32 days after an initial burst release of 20%. The authors then studied the diffusion of NT4–PAMAM after intravitreal injection in a retroorbital sodium iodate mouse model of retinal injury. NT4 was a detected by ELISA in the vitreous for 28 days and within the retina for 14 days. The dendrimer was present in the vitreous, but not the retina, after 7 days, and no dendrimer was observed at 28 days.

PAMAM (G5) was reacted with 4-(bromomethyl)phenylboronic acid to make a boronic acid-rich dendrimer (BARD) and used to electrostatically bind FITC-conjugated superoxide

dismutase (SOD) [74]. SOD is an enzyme that catalyzes two superoxide molecules into elemental oxygen and hydrogen peroxide. These particles were tested in a rat model of retinal vein ischemia/reperfusion (I/R) achieved by a temporary increase in intraocular pressure with canulated saline. The goal of this work was to intravitreally deliver SOD and protect retinal ganglion cells from oxidative stress. The particles ranged 100-200 nm in sized depending on polymer/protein ratio with an average loading capacity 60% (w/w). The particle and controls injected 22 hours after ischemic injury and incubated for 6 hours. ERG demonstrated I/R eye retinal function after particle injection to be on par with healthy controls, where untreated and free SOD injected eyes showed the same high level of impaired retinal function. These data were confirmed by histology by TUNEL, a marker for apoptotic cells, showing a higher level of apoptosis within the ganglion cell layer in I/R and I/R + SOD eyes as compared to the healthy control and particle injected eyes. No evidence of particle induced intraocular inflammation was observed.

1.6.3 Alternative Synthetic Polymer Nanoparticles

Alternative synthetic polymer nanoparticles encompasses both new and previously describe polymers, or combinations thereof, and synthesis approaches that span one or more of the methods discussed above.

Polylactic acid (PLA), polymethyl methacrylate (PMMA), methacrylic acid (MA) PLA PMMA-co-MA encapsulated rhodamine-6G (Rho-6G) or PLA PVA encapsulated Nile red (Nr) were studied for biodistribution and toxicity after intravitreal injection [75]. The nanoparticles were synthesized by nanoprecipitation [76]. The resulting particles were 140 ± 20 nm in diameter

and a surface charge of -60 mV for Rho-6G particles and 310 ± 40 nm and -6 mV for the Nr particles. *In vitro* nanoparticle release showed rapid release of Rho-6G from the nanoparticle matrix and much slower release of Nr over 8 days, plateauing for up to 30 days. The particles were then intravitreally injected into healthy rats. The *in vivo* distribution kinetics of both particle types were found to be very similar showing little influence from their relative size and surface charge. The Rho-6G particles were shown to penetrate the retinal inner limiting membrane within 1 hour and were found at the RPE cells within 4 hours and persisted for up to 4 months. A mild inflammatory response was observed 6 hours after injection at the ciliary body and a few inflammatory cells could be seen at 18 to 24 hours in vitreous and retina but decreased by 48 hours.

PLA/PLA-PEO, where PEO is polyethylene oxide, was used to encapsulate the integrin antagonist peptide DFKLFAVYIKYR (C16Y) [77]. The particles had a diameter of 302 ± 85.1 nm. On day 12 after disease induction, 7 days after therapeutic injection, the nanoparticles effectively reduced the progression of L-CNV rat model when compared to peptide alone, $p < 0.05$. Fluorophore encapsulated particles were found to localize at the RPE, suggesting these particles could deliver therapeutics to treat CNV related diseases.

DEX-γ-PGA-L-phenylalanine nanoparticles were synthesized by grafting phenylalanine-ethylester to polyglycolic acid (PGA) using EDC chemistry, and then electrostatic attaching dexamethasone or Texas Red Ovalbumin (TR-OVA) to the surface [78]. The phenylalanine acts as a hydrophobic core and PGA the hydrophilic outer layer for the amphiphilic nanoparticle synthesis. The resulting particles were 220 ± 65 and 180 ± 45 nm, respectively, with a zeta

potential of −25 mV. TR-OVA particles were shown to accumulate in the microglia in a rat model of N-methyl-D-aspartate (NMDA)-induced glial cell excitotoxicity and after induced retinal detachment. DEX particles were then shown to suppress NMDA-induced retinal glial cell death as compared to no-DEX control particles, $p = 0.0209$, and retinal detachment induced photoreceptor degradation, $p = 0.0065$.

Tamoxifen, a non-steroidal estrogen receptor modulator, was tested for efficacy in an rat model of EAU [79]. The co-polymer poly[methoxy poly(ethylene glycol) cyanoacrylate-co-hexadecyl cyanoacrylate] (1:4) was used to encapsulate tamoxifen, forming nanosized particles using a biphasic nanoprecipitation method [79-81]. The particles were injected intravitreally into rat eyes prior to disease onset and were shown to reduce EAU. However, when the nanoparticles were co-injected with the 17β-estradiol, no effect on disease progression was observed. This result indicates tamoxifen is an antagonist with estradiol. Moreover, injection free tamoxifen was unable to mitigate EAU, suggesting the encapsulation plays a role in efficacy. It was also shown that these particles lead to the downregulation of several inflammatory cytokines attributing to their efficacy.

Doxorubicin (DXR), an inhibitor of hypoxia-inducible factor-1 (HIF-1), was conjugated to poly[(sebacic acid)-co-(polyethylene glycol)$_3$] (PSA-3PEG) nanoparticles as a method for sustained release to treat choroidal and retinal neovascularization [82]. The particles measured 650 nm in diameter with 23% DXR (w/w) and were tested in mouse models for laser induced CNV and OIR. CNV was significantly less in eyes injected with DXR-PSA-PEG3 nanoparticles with DXR content of 10, 1.0, or 0.1 μg, where free DXR showed CNV reduction only in 10 μg,

p<0.001, however free DXR at bolus concentrations as 1 µg induced retinal damage at 14 days, not seen in the DXR nanoparticle conjugates. In mice having undergone oxygen-induced retinopathy, DXR-PSA-PEG3 particles, totaling 1ug DXR, showed a significant reduction in retinal NV at postnatal day 12 (P12) compared to PBS injected control eyes, $p < 0.001$. Using a *Rho/VEGF* transgenic mouse model of rhodopsin promoter driven VEGF expression, particles showed a reduction in area of NV for up to 5 weeks. Intravitreal injection of particles into healthy rabbit eyes showed the presence of DXR for up to 3 months.

Huu *et al.* developed a unique ultraviolet light (UV) responsive polymer nanoparticle formulation as a method for controlled drug release [83]. A quinone-methide based polymer with a diamine spacer was loaded with antiangiogenic small molecule drug ninedanib by emulsification where release was triggered by diamine cyclization of the polymer subunits upon UV irradiation [84]. This nanoparticle system was tested by injection in a rat model of L-CNV 10 weeks prior to disease induction. The particle was found to reduce the size of CNV upon UV induced drug release comparable to a free ninedanib demonstrating extended nanoparticle and drug stability.

Wu *et al.* developed nanoparticles to improve the water solubility and retinal bioavailability of the immunosuppressant rapamycin [85]. The particle formulation consisted of rapamycin incorporated with mPEG- poly(ε-caprolactone) in acetone, followed by evaporation and rehydration. The resulting particles were filtered to 0.22 µm and were tested for efficacy in an experimental rat model for EAU. The particles had a diameter of 40 nm and zeta potential of -0.89 mV. After intravitreal injection, the rapamycin concentrations were shown to remain

elevated in the retina over free drug for at least 14 days. The 9 μg rapamycin containing particles showed better slit lamp EAU clinical scores than 9 μg free drug over the course of the 20-day study, $p < 0.05$, with no effects on the systemic immune system as compared to the control animals.

1.7 Naturally Occurring Polymers and Protein Nanoparticles

Naturally occurring polymer nanoparticles consist principally of polysaccharide chains that vary in saccharide structure and branching linkages. They are advantageous in nanoparticle development because they are biocompatible, nontoxic, nonimmunogenic, and biodegradable. Chitosan is β-(1-4)-D-glucosamine and N-acetyl-D-glucosamine polymer that is a deacetylated form of chitin sourced from the crustacean shells [86]. It has a positive surface potential at physiologic pH and has been used in a wide variety of nanoparticle formulations [86]. Dextran is a lactobacillus derived poly-α-D-glucoside polymer with α-(1-6) linkages and α-(1-3) or α-(1-4) branch points [87]. Dextran has most notably been used as a blood volume expander and widely studied as a potential iron carrier for severe anemia. Hyaluronic acid (HA) consists of β-(1→3)-D-glucuronic acid β-(1→4) N-acetyl-D-glucosamine as is prevalent throughout the human body and is a major component of the vitreous [88]. HA has an intrinsic affinity for CD44, which is overexpressed in tumors, making it appealing for targeted chemotherapeutic delivery. HA is also a constituent of the extracellular matrix, making it amendable to tissue engineering and other biological scaffolds. HA used in nanoparticle synthesis is usually complexed with other polymers or modified for crosslinking or other functionalization. There poly-L-lysine has been exists two forms, α and ε [89]. The α-poly-L-lysine is a polymer with traditional amino carboxylic

acid linkages, where ε -poly-L-lysine links to the amine on the lysine side chain to the carboxylic acid. The free amine groups on either type of polymer can readily complex with the negatively charged backbone of nucleic acids, making poly-L-lysine a logical tool for condensing pDNA. The residual amine groups can also enhance cell penetration and are amicable to further conjugation chemistries. Finally, there are several nanoparticle syntheses routes that monopolize on naturally occurring proteins [90]. Human serum albumin (HSA) is the most common protein used due to the abundance in systemic circulation. Typically, drugs are chemically crosslinked or electrostatically bound to the surface of HSA or several HSA proteins complexed. Other proteins utilized are bovine serum albumin (BSA) and collagen, both mentioned below, lipoproteins, ferritin, and gelatin, to name a few. Each of the above mentioned naturally occurring polymers and proteins also have the added advantage of being environmentally friendly, if harvested ethically and sustainably, and are biodegradable depending on what polymers they are complexed with.

1.7.1 Chitosan

NOVAFECT O15 (N-O15) is an ultrapure 5.7 kDa chitosan historically marketed for gene delivery [91]. Puras *et al.* complexed N-O15 with 5.5 kb GFP plasmid pCMS-EGFP (P) at different charge ratios, from 10:1 up to 60:1, N-O15:GFP, to measure effects on particle size, zeta potential and transfection efficiency. Ratios of 10:1, 20:1 and 30:1 exhibited sizes < 250nm to 150 nm with zeta potentials from +6 to +10 mV, respectively. These particles were then evaluated for GFP expression *in vitro* using HEK-293 cells and showed an increase in GFP fluorescence corresponding to an increase in ratio. This trend reversed with ARPE-19 cells with

the greatest expression with a 10:1 ratio. When the 10:1 ratio was injected into rat eyes IVI and sub-retinal to observe GFP expression. Sub-retinal yielded expression predominately in the RPE and localized to the injection site. IVI resulted in expression within Müller cells and could be seen throughout the retina by flat mount. The 30:1 ratio shown no evidence of expression by either route of administration.

Bevacizumab-chitosan nanoparticles were prepared by an emulsification evaporation method where bevacizumab is electrostatically attached to chitosan, resulting in particles 88.9 ± 106.7 nm in diameter with a zeta potential of +21.63 ± 2.4 mV [92]. The particles were injected intravitreally into 3-month-old Sprague-Dawley diabetic rat model. No specifics were given about the method for disease induction. Histology of control animals showed retinal pathology consistent with diabetic retina over the course of the treatment window of 8 weeks. RT-qPCR data for VEGF mRNA showed a ~50% decrease in the upregulation of VEGF expression for both free bevacizumab and bevacizumab-chitosan at 1 week and ~80% decrease at 4 weeks when compared to the saline injected control. At 8 weeks free bevacizumab showed a 55% reduction and bevacizumab-chitosan showed an 80% reduction, suggesting sustained release effects beyond free drug, and a potential therapeutic benefit from the nanoparticle formulation.

Chitosan-thiolate nanoparticles were synthesized and loaded with topotecan, a chemotherapeutic topoisomerase 1 inhibitor, and characterized as a potential treatment for retinoblastoma [93]. The particles were 25 ± 2 nm and had an EE of 85%. The particles were tested for efficacy by intravitreal administration in a xenograft rat model by intraocular

injection of Y79 retinoblastoma cells. The particles demonstrated a significant difference reduction in tumor size between the tumor control and treated group, $p < 0.035$.

Chitosan-PLGA nanoparticles were used for the intravitreal delivery of a DNA plasmid expressing the 80-amino acid proteolytic plasminogen fragment Kringle 5 (K5) previously demonstrated to have antiangiogenic properties and to inhibit the expression of VEGF [94, 95]. The particles were tested in an oxygen-induced retinopathy (OIR) rat model and exhibited a high level of K5 expression along with reduced vascular leakage for 6 days after injection [94]. A reduction in both VEGF and intracellular adhesion molecule-1 (ICAM-1) overexpression and reduced vascular leakage was seen 4 weeks after particle injection in the retina of streptozotocin induced diabetic rats [94]. These same particles were injected into a L-CNV rat model and K5 expression was detected in the retina at 2 weeks [95]. Both the total area of CNV and the level of VEGF expression was reduced in the K5 nanoparticle treated eyes when compared to nanoparticle control [95]. These studies demonstrate an alternative method to adenoviruses for compact delivery of plasmids into retinal cells for viral vector-based therapeutics.

1.7.2 Dextran

Cholesteryl dextran (CDEX) nanoparticles with 5 mol % cholesterol, resulting in 77 kDa CDEX, were conjugated with PEG-peptides having an L-Arg content ranging incrementally from 1 to 4 amino acids [96]. The goal of this work was to test the effects of the increasing positive charge from L-Arg on diffusion of these particles through the negatively charged HA within the vitreous. The surface formulations were as follow: amino-PEG12-carboxyamido-Ile-Thr-Arg-Trp-

amide (1-Arg), amino-PEG8-Gly-Val-Ile-Thr-Arg-Ile-Arg-amide (2-Arg), amino-PEG12-carboxyamido-Arg-Arg-Ser-Arg-amide (3-Arg), and amino-PEG12-carboxyamido-Arg-Arg-Ser-Arg-Arg-amide (4-Arg). It was found *ex vivo* in rat vitreous that the lowest number of L-Arg diffused the fastest, with rates decreasing with increasing numbers of L-Arg. It was also shown by fluorescence fundus imaging that particles containing 1-Arg per peptide were not detectable in the rat vitreous *in vivo* after 8 days, 2-Arg persisted up to 60 days, and 3-Arg showed little change in diffusion or fluorescence at 180 days, with no evidence of inflammation in all animals tested as determined by histology.

CDEX nanoparticles consisting of 70 kDa dextran and 4 mol % cholesterol were conjugated with the fluorophore Cyanine 7-amine (Cy7) and either pyrrolidine-3-carboxyamido-PEG8-carboxyamido-Tyr-Arg-Val-Arg-Ser-amide (2-Arg), pyrrolidine-3-carboxyamido-PEG8-carboxyamido-Arg-Arg-Tyr-Arg-Leu-amide (3-Arg), or no peptide PEG control (0-Arg) [97]. The resulting particles were 85 ± 15 nm with +3.9 ± 0.9 mV for 2-Arg, 82 ± 7 nm with +6.3 ± 1.3 mV for 3-Arg, and 150 ± 2 nm with -0.6 ± 1 mV for 0-Arg. The particles were injected into healthy rabbit eyes and imaged *in vivo* for Cy7 fluorescence over 6 weeks. The half-lives of the particles were measured by fluorescence and found to be 6.9 days for 2-Arg, 16.9 days for 3-Arg, and 5.1 days for 0-Arg, suggesting a correlation between an increase in positive surface charge and an increase in ocular nanoparticle retention. Histology showed no evidence of inflammation, supporting the used of these particles for sustained interocular drug delivery.

1.7.3 Hyaluronic Acid

Nanoparticles were formed from branched PEI complexed with chains VEGF-A siRNAs linked by disulfide bonds from 5' siRNA thiol groups, called poly-siRNA, and further coated with HA [98]. The nanoparticles were 260.7 ± 43.27 nm in size with a −4.98 ± 0.47 mV zeta potential. They demonstrated Cy3 labeled nanoparticle uptake in ARPE-19 cells and showed knockdown of gene expression using B16F10 murine carcinoma cells. They also showed a reduction in L-CNV area with nanoparticle treatment when compared to control non-injected mice, $p < 0.05$. This same group applied rolling circle replication using complementary DNA plasmids to produce siRNA strands targeted at mouse VEGF [99]. The as synthesized RNA was washed and formed into nanoparticles first by incubating with branched PEI under sonication, and then by HA addition. The resulting particles were 259.82 ± 33.35 nm with a −41.2 ± 2.8 mV zeta potential. The particles were injected intravitreally into a mouse model of laser induced CNV. At 2 weeks post injection the eyes were enucleated and flat mounted for imaging of vasculature or used for RT-qPCR analysis of VEGF expression. The area of reduction in choroidal neovascularization was determined to be ~26% and the reduction of VEGF mRNA was found to be 41% in the choroid, demonstrating the particles were able to reach the choroid via intravitreal injection and influence CNV by suppressing VEGF expression in this animal model. This study also demonstrated the particle could reduce the area of retinal angiogenesis and vascular branching in a neonatal mouse model of elevated oxygen-induced retinopathy (OIR), suggesting the potential application for the treatment of PDR.

1.7.4 Poly-L-lysine

Nanoparticles consisting of branched poly-L-lysine linked to a $C_{12}H_{25}$ hydrocarbon were synthesized and loaded with an RNAi anti-VEGF oligonucleotide [100]. After intravitreal injection in a rat model of L-CNV it was shown the dendrimer plus the oligo particles significantly inhibited vascular leakage for 2-4 months when compared to oligo alone, as measured by fluorescein leakage density with fundus photography, $p < 0.05$. At 6 months no significant difference was observed. Particles with oligo-6FAM were seen distributed throughout the retina at 2 months and persisted at a lower density through 4 months as compared to almost no fluorescence observed from oligo-6FAM alone at 2 months. These data indicate the nanoparticle formulation functions for sustained oligo release as a potential therapeutic vehicle.

A 30-mer poly-L-lysine polymer with a terminal cystine was conjugated to 10K PEG, (CK30PEG10K) and used to condense a DNA plasmid containing a sequence for the potential anti-angiogenic factor MiR200-b to form nanoparticles for *in vivo* gene delivery [101]. Intravitreal injection showed the down regulation of VEGFR 2 and suppressed angiogenesis in a transgenic mouse model for late-onset diabetic retinopathy, demonstrating the ability of this polymer to compact and deliver large DNA plasmids as an alternative to synthetic viral delivery.

Polyion-complex (PIC) nanoparticles were formulated with fluorescein isothiocyanate-labeled poly-L-lysine (FITC-P(Lys)) in a 1:1 amino acid mol ratio with polyethylene glycol-*block*-poly-α,β-aspartic acid [102]. The particles had a mean diameter of 50.7 nm and were tested in a rat model of L-CNV. The PIC nanoparticles accumulated within the choroidal lesions at 1 hour

and remained detectable for 14 days, however the FITC-P(Lys) control was found to be highly toxic suggesting the potential for toxic side effects upon particle degradation.

1.7.5 Protein Nanoparticles

Ganciclovir was loaded into bovine serum albumin (BSA) nanoparticles to test for toxicity and release characteristics as a potential treatment for cytomegalovirus retinitis [103]. The nanoparticles were prepared by crosslinking BSA with glutaraldehyde and resulting in diameters of 290 nm with a -28mV zeta potential and 26.2 % (w/w) loading. The particles were tested in naïve rats and were found to retained on the retinal surface and in the ciliary body for 2 weeks and were not found to induce an autoimmune or inflammatory response.

Mo *et al.* evaluated using crosslinked HSA nanoparticles for the intraocular delivery of a plasmid containing the Cu, Zn superoxide dismutase (SOD1) gene [104]. HSA was incubated with the SOD1 plasmid in Tris-EDTA buffer, followed by dropwise addition of this solution to ethanol stirring and immediate addition of different concentrations of glutaraldehyde to crosslink and stabilize the resulting particles [105, 106]. Increasing the glutaraldehyde content from 0.002 to 0.1 mg mg^{-1} condensed the particles from 160 to 120 nm and decreased the zeta potential from -20 to -44 mV [104]. The higher crosslinking also decreased the *in vitro* plasmid release from 2 days at low crosslinking to 6 days at high crosslinking. The particles resulted in a higher transfection efficiency *in vitro* RPE cells when compared to the control, $p < 0.01$, and a higher efficiency when compared to plasmid transfection with lipofectamine. After injection in healthy mice SOD1 was detected by western blot at day 2, but not in the free SOD1-plasmid injected animals.

However, no SOD1 was detected in either animal at 7 days, suggesting further optimization is needed.

Basic fibroblast growth factor (bFGF)-impregnated gelatin nanoparticles were tested for efficacy using Royal College of Surgeons (RCS) rats with inherited retinal degeneration [107]. Freeze dried crosslinked bovine collagen gelatin nanoparticles were synthesized and infused with bFGF by aqueous swelling. The resulting in particles had an average diameter of 585 nm. The gelatin was radioiodinated using $Na^{125}I$ for *in vivo* studies. The particles were shown to be rapidly cleared to ~40% during day 1, followed by a steady decline up to 30 days measured by ^{125}I. Rhodamine labeled particles were shown to reside in the retina for up to 8 weeks. Intravitreal injected nanoparticle injected RCS rats showed a greater number of photo receptors as compared to free bFGF injected eyes as compared to the empty nanoparticle, $p < 0.05$, and non-injected control eyes at 8 weeks. Also, treated eyes demonstrated enhanced ERG signals as compared free drug, $p < 0.05$, and control groups suggesting the preservation of retinal function at 8 weeks. In a later study, the same group looked at neurotrophic pigment epithelium-derived factor (PEDF) which has been shown to rescue photoreceptors against degradation but likely requires sustained release for therapeutic efficacy [108]. Crosslinked gelatin particles were synthesized as describe above. In this study PEDF, rather than the gelatin particles, was radioiodinated using $Na^{125}I$ for *in vivo* studies. The nanoparticles exhibited sustained release of PEDF for 30 days in healthy Wistar rats. RCS rats were then injected intravitreally with PBS, blank nanoparticles, free PEDF or PEDF nanoparticles. The mean number of photoreceptors were counted in each group. All the control groups showed approximately

the same number photoreceptors and the PEDF nanoparticle group showed a ~2.5-fold increase at 4 weeks. At 8 weeks all groups showed a significant decrease int the numbers of photoreceptors by >50%, however the nanoparticle group remained ~2 fold higher than the control groups. ERG data showed the preservation of retinal function from the PEDF nanoparticle over the free PEDF at 8 weeks, $p = 0.0339$. Histology data showed a significant retention of cell function for the nanoparticle group at 4 weeks, $p = 0.0007$. These data show PEDF nanoparticles effectively delay photoreceptor degeneration in RCS rats due to sustained release.

Bevacizumab loaded albumin-PLGA nanoparticles were synthesized using a double emulsion method and monitored for extended release by intravitreal injection into healthy rabbits [109]. The intravitreal levels of bevacizumab were found to persist above 500 ng/mL for 8 weeks [109], the minimal concentration required to suppress VEGF induced endothelial cell migration *in vitro* [110], and found to retain in an active antibody structure as determined by ELISA.

HSA nanoparticles were synthesized by glutaraldehyde cross linking and tested for the effects of surface charge on intravitreal and retinal distribution [111]. The HAS particles were tested either as synthesized -33.3 ± -6.1 mV zeta potential or were cationized by covalent coupling of hexamethylenediamine on the particle surface, +11.7 ± +7.2 mV. The particles were conjugated to Alexa Fluor 555 for postmortem histological imaging. The resulting particles were injected intravitreally into both normal and L-CNV rat models. At 5 hours post rabbit intravitreal injection the positively changed nanoparticles were found to remain in the vitreous, while the

negatively charged particles diffused throughout the retina, with immunohistochemical evidence suggesting retinal uptake by muller glial cells.

Brimonidine (Br), α_2-adrenergic receptor agonist with neuroprotective effects against retinal ganglion cell death, was combined with HSA, and added to glutaraldehyde in solution for nanoparticle formation [112].The HSA-Br particles had a diameter of 152.8 ± 51.1 nm and a zeta potential of −29.7 ± 7.5 mV. The particles were tested for prophylactic efficacy using a rat optic nerve crush model where the ganglion cell density was measured by histology at 5 days and 14 days after injury onset. The cell density in the HAS-Br particle injected animals was higher than BSS controls, $p < 0.001$, demonstrating the benefits of the nanoparticle sustained release. Also noteworthy, the HSA-only particles exhibited significant neuroprotective effects, $p = 0.002$, ~1.6 fold greater than free Br at day 14, but still ~20% less cell density than the HAS-Br treated eyes. The authors attribute the benefits of the HSA-only particles to HSA's innate ability to sequester amyloid-β peptide [113], and confirmed the presence of amyloid-β by immunohistochemistry on optic nerve crush histological sections with a reduction in amyloid-β in the HAS-only optic nerve crush animals.

Bevacizumab was loaded into HSA-PLGA particles by double-emulsion and tested in healthy rabbits [109]. The resulting particles were measured to be 190 ± 29 nm with a PDI of 0.17 ± 0.05 and zeta potential of -24.5 ± 3.1. The calculated EE was 84.1% ± 4.2% and the loading capacity was 7.4% ± 0.4%. The authors were able to detect bevacizumab in the vitreous at concentrations above 500 ng mL^{-1} for ~8 weeks. Moreover, fluorescence from cumarin-6 HSA-PLGA particles was detected in the posterior segment for up to 56 days.

Apatinib, a chemotherapeutic receptor tyrosine kinase inhibitor that selectively targets VEGFR 2, was loaded into HAS-PEG nanoparticles and tested for efficacy in a mouse model of streptozotocin-induced diabetes [114]. The final particle diameter was 267.5 ± 0.97 nm with an EE of 77.1% and a loading capacity of 5.4% (w/w). To test the efficacy of the nanoparticle formulation mice were injected with VEGF to induce neovascularization and leakage. Mice injected with both VEGF and particles significantly reduced vascular leakage over VEGF only mice, $p < 0.05$. It was then shown that apatinib nanoparticles resulted in a concentration dependent reduction of vascular leakage in the diabetic mouse model as compared to the contralateral control eyes, $p < 0.01$, demonstrating the therapeutic potential of apatinib HSA-PEG nanoparticles as a drug delivery vehicle.

Hyaluronic acid (HA) coated HSA glutaraldehyde crosslinked particles incorporating the neural connexin antagonist Connexin43 (Cx43) were synthesized in attempt to increase *in vivo* peptide stability and bioavailability [115]. The particles were injected in a rat elevated intraocular pressure model for retinal ischemic injury immediately after reperfusion. Cx43-particles diffused throughout the retina within 24 hours and were decreasing, but present for at least 7 days. The Cx43-particles also demonstrated the highest level of retinal protection of free Cx43 or 1:1 (free Cx43:Cx43-particles), when compared saline control, by fundus imaging of changes in blood vessel diameter, $p = 0.0001$, changes to INL thickness with OCT, $p = 0.0001$.

1.8 Metals, Metal Oxides, and Metalloids

Metallic, metal oxide, metalloid nanoparticles have been extensively studied as *in vivo* imaging contrast agents and for their theranostic potential [116] [117] [118]. Their application to

intravitreal drug delivery has been somewhat limited. Below are a few select articles highlighting some of their unique properties.

1.8.1 Gold

Kim et al. delivered 20 nm gold nanoparticles IVI that were shown to inhibit vascular angiogenesis in a mouse model of oxygen-induced retinopathy and it was demonstrated *in vitro* that the reduction of neo-vessels was likely due, at least in part, to the gold nanoparticles suppressing the phosphorylation of VEGFR 2 [119].

IVI 160 nm gold nanodisks were also shown to inhibit neovascularization of oxygen-induced retinopathy in mice in a dose dependent manner [120]. The gold nanodisks were synthesized by nanoimprint lithography of nano-sized disks followed by gold deposition and liftoff. The nanodisks were designed to resonate at the near infrared to be detectable by OCT *in vivo*. The particles could be seen on mouse OCT scans with intraviral 0.5 µL injections of 1 pM gold. Control, 1 pM and 3 pM of gold nanodisks were injected into oxygen-induced retinopathy mice at postnatal day 14 (P14, the eyes were enucleated at P17 and evaluated for NV tufts after staining with glial cell specific isolectin-B4. A 50% reduction in tufts was observed with 1 pM gold nanodisks and ~75% reduction for 3 pM, with $p < 0.01$ and $p < 0.001$, respectively, with no evidence of toxicity in heathy eyes at 5 weeks. The nanodisks were shown to bind VEGF *in vitro* and to inhibit VEGF-induce migration of endothelial cells, leading the authors to conclude that the reduction in NV tufts is likely do to nanodisks sequestering free VEGF *in vivo*.

1.8.2 Cerium oxide

Cerium oxide nanoparticles, called nanoceria, have been shown to be effective in scavenging reactive oxygen species (ROS) [121]. Zhou *et al.* employed this material in attempt to reverse angiogenesis in very low-density lipoprotein receptor knockout (*vldlr*-/-) mice, shown to exhibit abnormal retinal blood vessel growth from anterior ganglion region toward the choroid [122]. VEGF expression in postnatal day 7 (P7) nanoceria injected mice was markedly reduced up to day P28, as were the number of neovascular lesions when compared to saline injection control. These results suggest a correlation between ROS and the development of the *vldlr*-/- pathology. In a later study this same group injected of nanoceria in P28 *vldlr*-/- mice and showed sustained regression neovessels for 6 weeks (P70) when compared to both saline and non-injected control, $p < 0.0001$ [92]. RT-qPCR of nanoceria injected eyes showed an increase rod- and cone-opsin expression levels, a reduction of caspase 3 gene expression, a protein involved in apoptosis, and reduced photoreceptor death. They also show a down-regulation of genes associated with the ASK1-P38/JNK-NF-κB apoptosis signaling pathway induced by nanoceria ROS scavenging.

1.8.3 Iron oxide

Iron oxide nanoparticles were tested for intraocular toxicity using a healthy rat model [123]. Two particle formulations were purchased and tested, 50 nm dextran coated and 4 µm polystyrene coated at ~1.7 mg each. Neither particle formulation was found to induce toxicity by measuring intraocular pressure, ERG, and histology at different time points from 1 hour to 5

months post-injection. Iron deposits were shown on the inner limiting membrane resulting from the 4 μm particles at 1 week and out to 5 months, and with no toxic side effects.

Iron oxide nanoparticles of different diameters were purchased, ranging from 252 nm to 17 nm, and different surface charges, -28 mV to +30 mV, and were tested for biodistribution by intravitreal injection in *xenopus* embryos [124]. In all cases the particles were found only within the RPE cell layer within 24 hours from time of injection, by histology and Persian Blue staining, with no systemic distribution. The particles localized as ~4 μm aggregates that the authors attributed to magnetic clustering during RPE cell uptake. Iron oxide nanoparticles reached the RPE in as little as 6 minutes and were still detectable 20 days after injection. These results were also repeated by the same group in zebrafish embryos, thus showing RPE cell localization of these particles is not specific to *xenopus* embryos, and that they may have utility as drug delivery vehicles specific to the RPE. To further investigate their utility, 61 nm carboxylic acid coated iron oxide nanoparticles were conjugated to recombinant VEGF (rVEGF) or poly-Lys by EDC chemistry and tested for activity and biodistribution in zebrafish embryos [125]. They hypothesized VEGF will act in a choroid targeting capacity sending the particles beyond the RPE. They found that rVEGF particles induce a pro-angiogenic phenotype after two days as compared to a bevacizumab co-injected rVEGF nanoparticle control, demonstrating that the rVEGF retains a functional form. They then showed 50% of rVEGF particles in the choroid as compared to ~5% for poly-Lys coated particles and ~10% for carboxylic acid coated particles, where >50% of the control particles remain in the RPE, supporting their hypothesis for the choroidal targeting capacity of VEGF proteins.

1.8.4 Silica

Silicate nanoparticles were shown to inhibit vascular angiogenesis in a mouse model of oxygen-induced retinopathy, and it was demonstrated *in vitro* that the reduction of neo-vessels attributed to the nanoparticles suppressing the phosphorylation of VEGFR 2 [126]. Similar results were shown by this group using gold nanoparticles mentioned above [119].

The anti-VEGF antibody therapeutic bevacizumab was adsorbed to the surface of (3-aminopropyl)triethoxysilane (APTES) functionalized mesoporous silica nanoparticles and tested for efficacy in a mouse oxygen-induced retinopathy model [127]. The particle diameter was determined to be 140 ± 18 nm as measured by TEM. The mice were intravitreally injected on postnatal day 13 (P13) and euthanized on day P17. The retinal whole mounts were stained with angiogenic blood vessel binding glycoprotein isolectin B4 and imaged by a fluorescent microscope to analyze the retinal vasculature. The particles were shown to inhibit retinal angiogenesis as compared the PBS injected control, and to further reduce the neovessels as compared to free bevacizumab, $p < 0.05$.

Mesoporous silica nanoparticles were synthesized by the traditional route of TEOS condensation in the presence of the surfactant CTAB [128]. The particles were then aminated with APTES. The immunosuppressant tacrolimus was adsorbed onto the particle surface resulting in a final diameter of 103 ± 14. 2 nm as measured by SEM and 225 ± 10 nm by DLS, with a zeta potential of +33 mV. The particles were evaluated in healthy rat eyes and did not exhibit toxicity or inflammation for 15 days post injection by color fundus exam or have a negative impact on retinal function as determined by ERG.

1.9 Conclusions and Perspectives

While many of the above nanoparticle formulations demonstrated a therapeutic advantage over intraocular injection of free drug, these differences may not significant enough to warrant translation into the clinic. One reason is several of the polymers mentioned above have a history of toxic side effect, either form the polymers themselves or from residual the organic solvent used in their production. Polymers that have a high number of primary amines, e.g. PAMAM [129], PEI [130], poly-L-lysine [131], etc., have been shown to destabilize cell membranes and lead to apoptosis and inflammation. There are, however, many options discussed above that have been thoroughly vetted for biocompatibility, e.g., liposomes, PLGA, etc., and only with the combination of the correct drug and disease will translation be possible. Moving forward, nanoparticle intraocular therapeutics will likely capitalize on recent innovations, e.g., gene therapy, RNA interference and gene editing. Nanoparticles have the capacity of loading larger DNA constructs than the more conventional AAV capsid and their use will expand therapeutic potential and improve efficacy of gene therapies. Also, nano formulations can aid in protecting siRNA, antisense oligos, and other nucleic acid payloads from degradation. When combined with cell specific targeted aptamers or peptides with the ability to deliver therapeutics directly to the diseased cells, nanoparticles could reduce both off target effects and the required therapeutic dose, and further bridge the gaps between research and the clinic.

1.10 References

1. Lee, R., T.Y. Wong, and C. Sabanayagam, *Epidemiology of diabetic retinopathy, diabetic macular edema and related vision loss.* Eye Vis (Lond), 2015. **2**: p. 17.

2. Wong, W.L., X. Su, X. Li, C.M. Cheung, R. Klein, C.Y. Cheng, and T.Y. Wong, *Global prevalence of age-related macular degeneration and disease burden projection for 2020 and 2040: a systematic review and meta-analysis.* Lancet Glob Health, 2014. **2**(2): p. e106-16.

3. Kang-Mieler, J.J., C.R. Osswald, and W.F. Mieler, *Advances in ocular drug delivery: emphasis on the posterior segment.* Expert Opinion on Drug Delivery, 2014. **11**(10): p. 1647-1660.

4. Freddo, T.F., *A contemporary concept of the blood-aqueous barrier.* Prog Retin Eye Res, 2013. **32**: p. 181-95.

5. Cunha-Vaz, J., R. Bernardes, and C. Lobo, *Blood-retinal barrier.* Eur J Ophthalmol, 2011. **21 Suppl 6**: p. S3-9.

6. Diaz-Coranguez, M., C. Ramos, and D.A. Antonetti, *The inner blood-retinal barrier: Cellular basis and development.* Vision Res, 2017. **139**: p. 123-137.

7. Naylor, A., A. Hopkins, N. Hudson, and M. Campbell, *Tight Junctions of the Outer Blood Retina Barrier.* Int J Mol Sci, 2019. **21**(1).

8. Purnyn, H., *The Mammalian Retina: Structure and Blood Supply.* Neurophysiology, 2013. **45**.

9. Hughes, P.M., O. Olejnik, J.E. Chang-Lin, and C.G. Wilson, *Topical and systemic drug delivery to the posterior segments.* Adv Drug Deliv Rev, 2005. **57**(14): p. 2010-32.

10. Wang, J., A. Jiang, M. Joshi, and J. Christoforidis, *Drug Delivery Implants in the Treatment of Vitreous Inflammation.* Mediators of Inflammation, 2013. **2013**: p. 780634.

11. Johnson, A.R., S.P. Forster, D. White, G. Terife, M. Lowinger, R.S. Teller, and S.E. Barrett, *Drug eluting implants in pharmaceutical development and clinical practice.* Expert Opinion on Drug Delivery, 2021. **18**(5): p. 577-593.

12. Falavarjani, K.G. and Q.D. Nguyen, *Adverse events and complications associated with intravitreal injection of anti-VEGF agents: a review of literature.* Eye (Lond), 2013. **27**(7): p. 787-94.

13. Mains, J. and C.G. Wilson, *The vitreous humor as a barrier to nanoparticle distribution.* J Ocul Pharmacol Ther, 2013. **29**(2): p. 143-50.

14. Le Goff, M.M. and P.N. Bishop, *Adult vitreous structure and postnatal changes.* Eye (Lond), 2008. **22**(10): p. 1214-22.

15. Bishop, P.N., *Structural macromolecules and supramolecular organisation of the vitreous gel.* Prog Retin Eye Res, 2000. **19**(3): p. 323-44.

16. Barza, M., M. Stuart, and F. Szoka, *Effect of Size and Lipid-Composition on the Pharmacokinetics of Intravitreal Liposomes.* Investigative Ophthalmology & Visual Science, 1987. **28**(5): p. 893-900.

17. Sakurai, E., H. Ozeki, N. Kunou, and Y. Ogura, *Effect of particle size of polymeric nanospheres on intravitreal kinetics.* Ophthalmic Research, 2001. **33**(1): p. 31-36.

18. Peeters, L., N.N. Sanders, K. Braeckmans, K. Boussery, J. Van de Voorde, S.C. De Smedt, and J. Demeester, *Vitreous: A barrier to nonviral ocular gene therapy.* Investigative Ophthalmology & Visual Science, 2005. **46**(10): p. 3553-3561.

19. Koo, H., H. Moon, H. Han, J.H. Na, M.S. Huh, J.H. Park, S.J. Wood, K.H. Park, I.C. Kwon, K. Kim, and H. Kim, *The movement of self-assembled amphiphilic polymeric nanoparticles in the vitreous and retina after intravitreal injection.* Biomaterials, 2012. **33**(12): p. 3485-3493.

20. Xu, Q., N.J. Boylan, J.S. Suk, Y.Y. Wang, E.A. Nance, J.C. Yang, P.J. McDonnell, R.A. Cone, E.J. Duh, and J. Hanes, *Nanoparticle diffusion in, and microrheology of, the bovine vitreous ex vivo.* J Control Release, 2013. **167**(1): p. 76-84.

21. Large, D.E., R.G. Abdelmessih, E.A. Fink, and D.T. Auguste, *Liposome composition in drug delivery design, synthesis, characterization, and clinical application.* Advanced Drug Delivery Reviews, 2021. **176**: p. 113851.

22. Sercombe, L., T. Veerati, F. Moheimani, S.Y. Wu, A.K. Sood, and S. Hua, *Advances and Challenges of Liposome Assisted Drug Delivery.* Frontiers in Pharmacology, 2015. **6**(286).

23. Has, C. and P. Sunthar, *A comprehensive review on recent preparation techniques of liposomes.* Journal of Liposome Research, 2020. **30**(4): p. 336-365.

24. Fiscella, R., G.A. Peyman, and P.H. Fishman, *Duration of therapeutic levels of intravitreally injected liposome-encapsulated clindamycin in the rabbit.* Can J Ophthalmol, 1987. **22**(6): p. 307-9.

25. Wiechens, B., R. Krausse, J.B. Grammer, D. Neumann, U. Pleyer, and G.I. Duncker, *[Clearance of liposome-incorporated ciprofloxacin after intravitreal injection in rabbit eyes].* Klin Monbl Augenheilkd, 1998. **213**(5): p. 284-92.

26. Bourlais, C.L., F. Chevanne, P. Ropert, G. Bretagne, L. Acar, H. Zia, P.A. Sado, T. Needham, and R. Leverge, *Release kinetics of liposome-encapsulated ganciclovir after intravitreal injection in rabbits.* Journal of Microencapsulation, 1996. **13**(4): p. 473-480.

27. Cheng, L.Y., K.Y. Hostetler, S. Chaidhawangul, M.F. Gardner, J.R. Beadle, K.S. Keefe, G. Bergeron-Lynn, G.M. Severson, K.A. Soules, A.J. Mueller, and W.R. Freeman, *Intravitreal toxicology and duration of efficacy of a novel antiviral lipid prodrug of ganciclovir in liposome formulation.* Investigative Ophthalmology & Visual Science, 2000. **41**(6): p. 1523-1532.

28. Hughes, J.P., S. Rees, S.B. Kalindjian, and K.L. Philpott, *Principles of early drug discovery.* British journal of pharmacology, 2011. **162**(6): p. 1239-1249.

29. Claro, C., R. Ruiz, E. Cordero, M.T. Pastor, L.F. López-Cortés, M. Jiménez-Castellanos, and M. Lucero, *Determination and pharmacokinetic profile of liposomal foscarnet in rabbit ocular tissues after intravitreal administration.* Exp Eye Res, 2009. **88**(3): p. 528-34.

30. Timmers, A.M., J.A. Newmark, H.T. Turunen, T. Farivar, J. Liu, C. Song, G.-j. Ye, S. Pennock, C. Gaskin, D.R. Knop, and M.S. Shearman, *Ocular Inflammatory Response to*

Intravitreal Injection of Adeno-Associated Virus Vector: Relative Contribution of Genome and Capsid. Human Gene Therapy, 2019. **31**(1-2): p. 80-89.

31. Kawakami, S., A. Harada, K. Sakanaka, K. Nishida, J. Nakamura, T. Sakaeda, N. Ichikawa, M. Nakashima, and H. Sasaki, *In vivo gene transfection via intravitreal injection of cationic liposome/plasmid DNA complexes in rabbits.* Int J Pharm, 2004. **278**(2): p. 255-62.

32. Donkuru, M., S.D. Wettig, R.E. Verrall, I. Badea, and M. Foldvari, *Designing pH-sensitive gemini nanoparticles for non-viral gene delivery into keratinocytes.* Journal of Materials Chemistry, 2012. **22**(13): p. 6232-6244.

33. Alqawlaq, S., J.M. Sivak, J.T. Huzil, M.V. Ivanova, J.G. Flanagan, M.A. Beazely, and M. Foldvari, *Preclinical development and ocular biodistribution of gemini-DNA nanoparticles after intravitreal and topical administration: towards non-invasive glaucoma gene therapy.* Nanomedicine, 2014. **10**(8): p. 1637-47.

34. Bochot, A., E. Fattal, V. Boutet, J.R. Deverre, J.C. Jeanny, H. Chacun, and P. Couvreur, *Intravitreal delivery of oligonucleotides by sterically stabilized liposomes.* Investigative Ophthalmology & Visual Science, 2002. **43**(1): p. 253-259.

35. Liu, H.A., Y.L. Liu, Z.Z. Ma, J.C. Wang, and Q. Zhang, *A lipid nanoparticle system improves siRNA efficacy in RPE cells and a laser-induced murine CNV model.* Invest Ophthalmol Vis Sci, 2011. **52**(7): p. 4789-94.

36. Huang, X.N. and Y. Chau, *Investigating impacts of surface charge on intraocular distribution of intravitreal lipid nanoparticles.* Experimental Eye Research, 2019. **186**.

37. Huang, X. and Y. Chau, *Enhanced Delivery of siRNA to Retinal Ganglion Cells by Intravitreal Lipid Nanoparticles of Positive Charge.* Mol Pharm, 2021. **18**(1): p. 377-385.

38. Lajavardi, L., A. Bochot, S. Camelo, B. Goldenberg, M.C. Naud, F. Behar-Cohen, E. Fattal, and Y. de Kozak, *Downregulation of endotoxin-induced uveitis by intravitreal injection of vasoactive intestinal peptide encapsulated in liposomes.* Investigative Ophthalmology & Visual Science, 2007. **48**(7): p. 3230-3238.

39. Camelo, S., L. Lajavardi, A. Bochot, B. Goldenberg, M.C. Naud, E. Fattal, F. Behar-Cohen, and Y. de Kozak, *Ocular and systemic bio-distribution of rhodamine-conjugated*

liposomes loaded with VIP injected into the vitreous of Lewis rats. Mol Vis, 2007. **13**: p. 2263-74.

40. Zhang, R., R. He, J. Qian, J. Guo, K. Xue, and Y.F. Yuan, *Treatment of experimental autoimmune uveoretinitis with intravitreal injection of tacrolimus (FK506) encapsulated in liposomes.* Invest Ophthalmol Vis Sci, 2010. **51**(7): p. 3575-82.

41. Otake, K., T. Shimomura, T. Goto, T. Imura, T. Furuya, S. Yoda, Y. Takebayashi, H. Sakai, and M. Abe, *Preparation of liposomes using an improved supercritical reverse phase evaporation method.* Langmuir, 2006. **22**(6): p. 2543-50.

42. Gan, L., J. Wang, Y. Zhao, D. Chen, C. Zhu, J. Liu, and Y. Gan, *Hyaluronan-modified core-shell liponanoparticles targeting CD44-positive retinal pigment epithelium cells via intravitreal injection.* Biomaterials, 2013. **34**(24): p. 5978-87.

43. Yerushalmi, N. and R. Margalit, *Hyaluronic acid-modified bioadhesive liposomes as local drug depots: Effects of cellular and fluid dynamics on liposome retention at target sites.* Archives of Biochemistry and Biophysics, 1998. **349**(1): p. 21-26.

44. Wang, J.L., Y.L. Liu, Y. Li, W.B. Dai, Z.M. Guo, Z.H. Wang, and Q. Zhang, *EphA2 Targeted Doxorubicin Stealth Liposomes as a Therapy System for Choroidal Neovascularization in Rats.* Investigative Ophthalmology & Visual Science, 2012. **53**(11): p. 7348-7357.

45. Lee, J., U. Goh, H.J. Lee, J. Kim, M. Jeong, and J.H. Park, *Effective Retinal Penetration of Lipophilic and Lipid-Conjugated Hydrophilic Agents Delivered by Engineered Liposomes.* Mol Pharm, 2017. **14**(2): p. 423-430.

46. Mehnert, W. and K. Mäder, *Solid lipid nanoparticles: Production, characterization and applications.* Advanced Drug Delivery Reviews, 2012. **64**: p. 83-101.

47. Duan, Y., A. Dhar, C. Patel, M. Khimani, S. Neogi, P. Sharma, N. Siva Kumar, and R.L. Vekariya, *A brief review on solid lipid nanoparticles: part and parcel of contemporary drug delivery systems.* RSC Advances, 2020. **10**(45): p. 26777-26791.

48. Puras, G., M. Mashal, J. Zarate, M. Agirre, E. Ojeda, S. Grijalvo, R. Eritja, A. Diaz-Tahoces, G. Martinez Navarrete, M. Aviles-Trigueros, E. Fernandez, and J.L. Pedraz, *A novel cationic niosome formulation for gene delivery to the retina.* J Control Release, 2014. **174**: p. 27-36.

49. Apaolaza, P.S., A. Del Pozo-Rodriguez, M.A. Solinis, J.M. Rodriguez, U. Friedrich, J. Torrecilla, B.H. Weber, and A. Rodriguez-Gascon, *Structural recovery of the retina in a retinoschisin-deficient mouse after gene replacement therapy by solid lipid nanoparticles.* Biomaterials, 2016. **90**: p. 40-9.

50. del Pozo-Rodriguez, A., D. Delgado, M.A. Solinis, A.R. Gascon, and J.L. Pedraz, *Solid lipid nanoparticles: Formulation factors affecting cell transfection capacity.* International Journal of Pharmaceutics, 2007. **339**(1-2): p. 261-268.

51. Abrishami, M., M. Abrishami, A. Mahmoudi, N. Mosallaei, M. Vakili Ahrari Roodi, and B. Malaekeh-Nikouei, *Solid Lipid Nanoparticles Improve the Diclofenac Availability in Vitreous after Intraocular Injection.* J Drug Deliv, 2016. **2016**: p. 1368481.

52. Freitas, L.G.A., D.L.C. Isaac, E.M. Lima, L.G. Souza, M.A. Abud, R.G.D. Reis, W.T. Tannure, and M.P. Avila, *Retinal changes in rabbit after intravitreal injection of sunitinib encapsulated into solid lipid nanoparticles and polymeric nanocapsules.* Arq Bras Oftalmol, 2018. **81**(5): p. 408-413.

53. Ahmad, I., J. Pandit, Y. Sultana, A.K. Mishra, P.P. Hazari, and M. Aqil, *Optimization by design of etoposide loaded solid lipid nanoparticles for ocular delivery: Characterization, pharmacokinetic and deposition study.* Materials Science and Engineering: C, 2019. **100**: p. 959-970.

54. Qin, Y., Y. Tian, Y. Liu, D. Li, H. Zhang, Y. Yang, J. Qi, H. Wang, and L. Gan, *Hyaluronic acid-modified cationic niosomes for ocular gene delivery: improving transfection efficiency in retinal pigment epithelium.* J Pharm Pharmacol, 2018. **70**(9): p. 1139-1151.

55. Puras, G., G. Martinez-Navarrete, M. Mashal, J. Zarate, M. Agirre, E. Ojeda, S. Grijalvo, R. Eritja, A. Diaz-Tahoces, M. Aviles-Trigueros, E. Fernandez, and J.L. Pedraz, *Protamine/DNA/Niosome Ternary Nonviral Vectors for Gene Delivery to the Retina: The Role of Protamine.* Molecular Pharmaceutics, 2015. **12**(10): p. 3658-3671.

56. Danhier, F., E. Ansorena, J.M. Silva, R. Coco, A. Le Breton, and V. Préat, *PLGA-based nanoparticles: an overview of biomedical applications.* J Control Release, 2012. **161**(2): p. 505-22.

57. Wang, Y., B. Qin, G. Xia, and S.H. Choi, *FDA's Poly (Lactic-Co-Glycolic Acid) Research Program and Regulatory Outcomes.* The AAPS Journal, 2021. **23**(4): p. 92.

58. Bejjani, R.A., D. BenEzra, H. Cohen, J. Rieger, C. Andrieu, J.C. Jeanny, G. Gollomb, and F.F. Behar-Cohen, *Nanoparticles for gene delivery to retinal pigment epithelial cells.* Mol Vis, 2005. **11**: p. 124-32.

59. Xu, J., Y. Wang, Y. Li, X. Yang, P. Zhang, H. Hou, Y. Shi, and C. Song, *Inhibitory efficacy of intravitreal dexamethasone acetate-loaded PLGA nanoparticles on choroidal neovascularization in a laser-induced rat model.* J Ocul Pharmacol Ther, 2007. **23**(6): p. 527-40.

60. Zhang, L., Y. Li, C. Zhang, Y. Wang, and C. Song, *Pharmacokinetics and tolerance study of intravitreal injection of dexamethasone-loaded nanoparticles in rabbits.* Int J Nanomedicine, 2009. **4**: p. 175-83.

61. Zhang, C., Y.S. Wang, H. Wu, Z.X. Zhang, Y. Cai, H.Y. Hou, W. Zhao, X.M. Yang, and J.X. Ma, *Inhibitory efficacy of hypoxia-inducible factor 1α short hairpin RNA plasmid DNA-loaded poly (D, L-lactide-co-glycolide) nanoparticles on choroidal neovascularization in a laser-induced rat model.* Gene Therapy, 2010. **17**(3): p. 338-351.

62. Robinson, R., S.R. Viviano, J.M. Criscione, C.A. Williams, L. Jun, J.C. Tsai, and E.B. Lavik, *Nanospheres delivering the EGFR TKI AG1478 promote optic nerve regeneration: the role of size for intraocular drug delivery.* ACS Nano, 2011. **5**(6): p. 4392-400.

63. Robinson, R., J.P. Bertram, J.L. Reiter, and E.B. Lavik, *New platform for controlled and sustained delivery of the EGF receptor tyrosine kinase inhibitor AG1478 using poly(lactic-co-glycolic acid) microspheres.* J Microencapsul, 2010. **27**(3): p. 263-71.

64. Danesh-Meyer, H.V., N.M. Kerr, J. Zhang, E.K. Eady, S.J. O'Carroll, L.F.B. Nicholson, C.S. Johnson, and C.R. Green, *Connexin43 mimetic peptide reduces vascular leak and retinal ganglion cell death following retinal ischaemia.* Brain, 2012. **135**: p. 506-520.

65. Chen, Y.S., C.R. Green, K. Wang, H.V. Danesh-Meyer, and I.D. Rupenthal, *Sustained intravitreal delivery of connexin43 mimetic peptide by poly(D,L-lactide-co-glycolide) acid micro- and nanoparticles--Closing the gap in retinal ischaemia.* Eur J Pharm Biopharm, 2015. **95**(Pt B): p. 378-86.

66. Zhang, X.P., J.G. Sun, J. Yao, K. Shan, B.H. Liu, M.D. Yao, H.M. Ge, Q. Jiang, C. Zhao, and B. Yan, *Effect of nanoencapsulation using poly (lactide-co-glycolide) (PLGA) on anti-angiogenic activity of bevacizumab for ocular angiogenesis therapy.* Biomed Pharmacother, 2018. **107**: p. 1056-1063.

67. Nor, N.M., C.X. Guo, I.D. Rupenthal, Y.S. Chen, C.R. Green, and M.L. Acosta, *Sustained Connexin43 Mimetic Peptide Release From Loaded Nanoparticles Reduces Retinal and Choroidal Photodamage.* Investigative Ophthalmology & Visual Science, 2018. **59**(8): p. 3682-3693.

68. Liu, J., L. Luo, F. Xu, G. Li, J. Chen, L. Teng, Y. Li, and F. Sun, *Cyclic RGD Peptide Targeting Coated Nano Drug Co-Delivery System for Therapeutic Use in Age-Related Macular Degeneration Disease.* Molecules, 2020. **25**(21).

69. Abbasi, E., S.F. Aval, A. Akbarzadeh, M. Milani, H.T. Nasrabadi, S.W. Joo, Y. Hanifehpour, K. Nejati-Koshki, and R. Pashaei-Asl, *Dendrimers: synthesis, applications, and properties.* Nanoscale Research Letters, 2014. **9**(1): p. 247.

70. Boas, U. and P.M.H. Heegaard, *Dendrimers in drug research.* Chemical Society Reviews, 2004. **33**(1): p. 43-63.

71. Luong, D., P. Kesharwani, R. Deshmukh, M.C.I. Mohd Amin, U. Gupta, K. Greish, and A.K. Iyer, *PEGylated PAMAM dendrimers: Enhancing efficacy and mitigating toxicity for effective anticancer drug and gene delivery.* Acta Biomaterialia, 2016. **43**: p. 14-29.

72. Yavuz, B., S. Bozdag Pehlivan, B. Sumer Bolu, R. Nomak Sanyal, I. Vural, and N. Unlu, *Dexamethasone - PAMAM dendrimer conjugates for retinal delivery: preparation, characterization and in vivo evaluation.* J Pharm Pharmacol, 2016. **68**(8): p. 1010-20.

73. Dabkowska, M., D. Roginska, P. Klos, A. Sobus, M. Adamczak, Z. Litwinska, A. Machalinska, and B. Machalinski, *Electrostatic complex of neurotrophin 4 with dendrimer nanoparticles: controlled release of protein in vitro and in vivo.* Int J Nanomedicine, 2019. **14**: p. 6117-6131.

74. Zhou, X., J. Lv, G. Li, T. Qian, H. Jiang, J. Xu, Y. Cheng, and J. Hong, *Rescue the retina after the ischemic injury by polymer-mediated intracellular superoxide dismutase delivery.* Biomaterials, 2021. **268**: p. 120600.

75. Bourges, J.L., S.E. Gautier, F. Delie, R.A. Bejjani, J.C. Jeanny, R. Gurny, D. BenEzra, and F.F. Behar-Cohen, *Ocular drug delivery targeting the retina and retinal pigment epithelium using polylactide nanoparticles.* Invest Ophthalmol Vis Sci, 2003. **44**(8): p. 3562-9.

76. Gautier, S., N. Grudzielski, G. Goffinet, S.H. de Hassonville, L. Delattre, and R. Jerjme, *Preparation of poly(D,L-lactide) nanoparticles assisted by amphiphilic poly(methyl methacrylate-co-methacrylic acid) copolymers.* J Biomater Sci Polym Ed, 2001. **12**(4): p. 429-50.

77. Kim, H. and K.G. Csaky, *Nanoparticle-integrin antagonist C16Y peptide treatment of choroidal neovascularization in rats.* J Control Release, 2010. **142**(2): p. 286-93.

78. Ryu, M., T. Nakazawa, T. Akagi, T. Tanaka, R. Watanabe, M. Yasuda, N. Himori, K. Maruyama, T. Yamashita, T. Abe, M. Akashi, and K. Nishida, *Suppression of phagocytic cells in retinal disorders using amphiphilic poly (gamma-glutamic acid) nanoparticles containing dexamethasone.* Journal of Controlled Release, 2011. **151**(1): p. 65-73.

79. de Kozak, Y., K. Andrieux, H. Villarroya, C. Klein, B. Thillaye-Goldenberg, M.C. Naud, E. Garcia, and P. Couvreur, *Intraocular injection of tamoxifen-loaded nanoparticles: a new treatment of experimental autoimmune uveoretinitis.* European Journal of Immunology, 2004. **34**(12): p. 3702-3712.

80. Brigger, I., P. Chaminade, V. Marsaud, M. Appel, M. Besnard, R. Gurny, M. Renoir, and P. Couvreur, *Tamoxifen encapsulation within polyethylene glycol-coated nanospheres. A new antiestrogen formulation.* Int J Pharm, 2001. **214**(1-2): p. 37-42.

81. Peracchia, M.T., D. Desmaele, P. Couvreur, and J. dAngelo, *Synthesis of a novel poly(MePEG cyanoacrylate-co-alkyl cyanoacrylate) amphiphilic copolymer for nanoparticle technology.* Macromolecules, 1997. **30**(4): p. 846-851.

82. Iwase, T., J. Fu, T. Yoshida, D. Muramatsu, A. Miki, N. Hashida, L. Lu, B. Oveson, R. Lima e Silva, C. Seidel, M. Yang, S. Connelly, J. Shen, B. Han, M. Wu, G.L. Semenza, J. Hanes, and P.A. Campochiaro, *Sustained delivery of a HIF-1 antagonist for ocular neovascularization.* J Control Release, 2013. **172**(3): p. 625-33.

83. Huu, V.A., J. Luo, J. Zhu, J. Zhu, S. Patel, A. Boone, E. Mahmoud, C. McFearin, J. Olejniczak, C. de Gracia Lux, J. Lux, N. Fomina, M. Huynh, K. Zhang, and A. Almutairi,

Light-responsive nanoparticle depot to control release of a small molecule angiogenesis inhibitor in the posterior segment of the eye. J Control Release, 2015. **200**: p. 71-7.

84. Fomina, N., C. McFearin, M. Sermsakdi, O. Edigin, and A. Almutairi, *UV and near-IR triggered release from polymeric nanoparticles.* J Am Chem Soc, 2010. **132**(28): p. 9540-2.

85. Wu, W., Z.F. He, Z.L. Zhang, X.X. Yu, Z.M. Song, and X.Y. Li, *Intravitreal injection of rapamycin-loaded polymeric micelles for inhibition of ocular inflammation in rat model.* International Journal of Pharmaceutics, 2016. **513**(1-2): p. 238-246.

86. Cheung, R.C.F., T.B. Ng, J.H. Wong, and W.Y. Chan, *Chitosan: An Update on Potential Biomedical and Pharmaceutical Applications.* Marine drugs, 2015. **13**(8): p. 5156-5186.

87. Hu, Q., Y. Lu, and Y. Luo, *Recent advances in dextran-based drug delivery systems: From fabrication strategies to applications.* Carbohydrate Polymers, 2021. **264**: p. 117999.

88. Tiwari, S. and P. Bahadur, *Modified hyaluronic acid based materials for biomedical applications.* International Journal of Biological Macromolecules, 2019. **121**: p. 556-571.

89. Manouchehri, S., P. Zarrintaj, M.R. Saeb, and J.D. Ramsey, *Advanced Delivery Systems Based on Lysine or Lysine Polymers.* Molecular Pharmaceutics, 2021. **18**(10): p. 3652-3670.

90. Hong, S., D.W. Choi, H.N. Kim, C.G. Park, W. Lee, and H.H. Park, *Protein-Based Nanoparticles as Drug Delivery Systems.* Pharmaceutics, 2020. **12**(7).

91. Puras, G., J. Zarate, M. Aceves, A. Murua, A. Diaz-Tahoces, M. Aviles-Triguero, E. Fernandez, and J.L. Pedraz, *Low molecular weight oligochitosans for non-viral retinal gene therapy.* European Journal of Pharmaceutics and Biopharmaceutics, 2013. **83**(2): p. 131-140.

92. Lu, Y., N. Zhou, X. Huang, J.W. Cheng, F.Q. Li, R.L. Wei, and J.P. Cai, *Effect of intravitreal injection of bevacizumab-chitosan nanoparticles on retina of diabetic rats.* Int J Ophthalmol, 2014. **7**(1): p. 1-7.

93. Delrish, E., M. Jabbarvand, F. Ghassemi, F.A. Amoli, F. Atyabi, A. Lashay, M. Soleimani, L. Aghajanpour, and R. Dinarvand, *Efficacy of topotecan nanoparticles for intravitreal chemotherapy of retinoblastoma.* Exp Eye Res, 2021. **204**: p. 108423.

94. Park, K., Y. Chen, Y. Hu, A.S. Mayo, U.B. Kompella, R. Longeras, and J.X. Ma, *Nanoparticle-mediated expression of an angiogenic inhibitor ameliorates ischemia-induced retinal neovascularization and diabetes-induced retinal vascular leakage.* Diabetes, 2009. **58**(8): p. 1902-13.

95. Jin, J., K.K. Zhou, K. Park, Y. Hu, X. Xu, Z. Zheng, P. Tyagi, U.B. Kompella, and J.X. Ma, *Anti-inflammatory and antiangiogenic effects of nanoparticle-mediated delivery of a natural angiogenic inhibitor.* Invest Ophthalmol Vis Sci, 2011. **52**(9): p. 6230-7.

96. Li, H., W. Liu, C.M. Sorenson, N. Sheibani, D.M. Albert, T. Senanayake, S. Vinogradov, J. Henkin, and H.F. Zhang, *Sustaining Intravitreal Residence With L-Arginine Peptide-Conjugated Nanocarriers.* Invest Ophthalmol Vis Sci, 2017. **58**(12): p. 5142-5150.

97. Melgar-Asensio, I., I. Kandela, F. Aird, S.R. Darjatmoko, C. de Los Rios, C.M. Sorenson, D.M. Albert, N. Sheibani, and J. Henkin, *Extended Intravitreal Rabbit Eye Residence of Nanoparticles Conjugated With Cationic Arginine Peptides for Intraocular Drug Delivery: In Vivo Imaging.* Invest Ophthalmol Vis Sci, 2018. **59**(10): p. 4071-4081.

98. Lee, J., N.K. Ryoo, H. Han, H.K. Hong, J.Y. Park, S.J. Park, Y.K. Kim, C. Sim, K. Kim, S.J. Woo, K.H. Park, and H. Kim, *Anti-VEGF PolysiRNA Polyplex for the Treatment of Choroidal Neovascularization.* Mol Pharm, 2016. **13**(6): p. 1988-95.

99. Ryoo, N.K., J. Lee, H. Lee, H.K. Hong, H. Kim, J.B. Lee, S.J. Woo, K.H. Park, and H. Kim, *Therapeutic effects of a novel siRNA-based anti-VEGF (siVEGF) nanoball for the treatment of choroidal neovascularization.* Nanoscale, 2017. **9**(40): p. 15461-15469.

100. Marano, R.J., I. Toth, N. Wimmer, M. Brankov, and P.E. Rakoczy, *Dendrimer delivery of an anti-VEGF oligonucleotide into the eye: a long-term study into inhibition of laser-induced CNV, distribution, uptake and toxicity.* Gene Ther, 2005. **12**(21): p. 1544-50.

101. Mitra, R.N., C.A. Nichols, J. Guo, R. Makkia, M.J. Cooper, M.I. Naash, and Z. Han, *Nanoparticle-mediated miR200-b delivery for the treatment of diabetic retinopathy.* J Control Release, 2016. **236**: p. 31-7.

102. Ideta, R., Y. Yanagi, Y. Tamaki, F. Tasaka, A. Harada, and K. Kataoka, *Effective accumulation of polyion complex micelle to experimental choroidal neovascularization in rats.* FEBS Lett, 2004. **557**(1-3): p. 21-5.

103. Merodio, M., J.M. Irache, F. Valamanesh, and M. Mirshahi, *Ocular disposition and tolerance of ganciclovir-loaded albumin nanoparticles after intravitreal injection in rats.* Biomaterials, 2002. **23**(7): p. 1587-94.

104. Mo, Y., M.E. Barnett, D. Takemoto, H. Davidson, and U.B. Kompella, *Human serum albumin nanoparticles for efficient delivery of Cu, Zn superoxide dismutase gene.* Mol Vis, 2007. **13**: p. 746-57.

105. Weber, C., C. Coester, J. Kreuter, and K. Langer, *Desolvation process and surface characterisation of protein nanoparticles.* International Journal of Pharmaceutics, 2000. **194**(1): p. 91-102.

106. Wartlick, H., B. Spankuch-Schmitt, K. Strebhardt, J. Kreuter, and K. Langer, *Tumour cell delivery of antisense oligonucleotides by human serum albumin nanoparticles.* Journal of Controlled Release, 2004. **96**(3): p. 483-495.

107. Sakai, T., N. Kuno, F. Takamatsu, E. Kimura, H. Kohno, K. Okano, and K. Kitahara, *Prolonged protective effect of basic fibroblast growth factor-impregnated nanoparticles in royal college of surgeons rats.* Invest Ophthalmol Vis Sci, 2007. **48**(7): p. 3381-7.

108. Akiyama, G., T. Sakai, N. Kuno, E. Kimura, K. Okano, H. Kohno, and H. Tsuneoka, *Photoreceptor rescue of pigment epithelium-derived factor-impregnated nanoparticles in Royal College of Surgeons rats.* Mol Vis, 2012. **18**: p. 3079-86.

109. Varshochian, R., M. Riazi-Esfahani, M. Jeddi-Tehrani, A.R. Mahmoudi, S. Aghazadeh, M. Mahbod, M. Movassat, F. Atyabi, A. Sabzevari, and R. Dinarvand, *Albuminated PLGA nanoparticles containing bevacizumab intended for ocular neovascularization treatment.* J Biomed Mater Res A, 2015. **103**(10): p. 3148-56.

110. Wang, Y., D. Fei, M. Vanderlaan, and A. Song, *Biological activity of bevacizumab, a humanized anti-VEGF antibody in vitro.* Angiogenesis, 2004. **7**(4): p. 335-45.

111. Kim, H., S.B. Robinson, and K.G. Csaky, *Investigating the movement of intravitreal human serum albumin nanoparticles in the vitreous and retina.* Pharm Res, 2009. **26**(2): p. 329-37.

112. Kim, K.E., I. Jang, H. Moon, Y.J. Kim, J.W. Jeoung, K.H. Park, and H. Kim, *Neuroprotective Effects of Human Serum Albumin Nanoparticles Loaded With Brimonidine on Retinal Ganglion Cells in Optic Nerve Crush Model.* Investigative Ophthalmology & Visual Science, 2015. **56**(9): p. 5641-5649.

113. Stanyon, H.F. and J.H. Viles, *Human Serum Albumin Can Regulate Amyloid-beta Peptide Fiber Growth in the Brain Interstitium IMPLICATIONS FOR ALZHEIMER DISEASE.* Journal of Biological Chemistry, 2012. **287**(33): p. 28163-28168.

114. Jeong, J.H., H.K. Nguyen, J.E. Lee, and W. Suh, *Therapeutic effect of apatinib-loaded nanoparticles on diabetes-induced retinal vascular leakage.* Int J Nanomedicine, 2016. **11**: p. 3101-9.

115. Huang, D., Y.S. Chen, C.R. Green, and I.D. Rupenthal, *Hyaluronic acid coated albumin nanoparticles for targeted peptide delivery in the treatment of retinal ischaemia.* Biomaterials, 2018. **168**: p. 10-23.

116. Ehlerding, E.B., P. Grodzinski, W. Cai, and C.H. Liu, *Big Potential from Small Agents: Nanoparticles for Imaging-Based Companion Diagnostics.* ACS Nano, 2018. **12**(3): p. 2106-2121.

117. Lei, Q., J.M. Guo, A. Noureddine, A.X. Wang, S. Wuttke, C.J. Brinker, and W. Zhu, *Sol-Gel-Based Advanced Porous Silica Materials for Biomedical Applications.* Advanced Functional Materials, 2020. **30**(41).

118. Kumeria, T., S.J.P. McInnes, S. Maher, and A. Santos, *Porous silicon for drug delivery applications and theranostics: recent advances, critical review and perspectives.* Expert Opinion on Drug Delivery, 2017. **14**(12): p. 1407-1422.

119. Kim, J.H., M.H. Kim, D.H. Jo, Y.S. Yu, T.G. Lee, and J.H. Kim, *The inhibition of retinal neovascularization by gold nanoparticles via suppression of VEGFR-2 activation.* Biomaterials, 2011. **32**(7): p. 1865-71.

120. Song, H.B., J.S. Wi, D.H. Jo, J.H. Kim, S.W. Lee, T.G. Lee, and J.H. Kim, *Intraocular application of gold nanodisks optically tuned for optical coherence tomography: inhibitory effect on retinal neovascularization without unbearable toxicity.* Nanomedicine, 2017. **13**(6): p. 1901-1911.

121. Karakoti, A.S., N.A. Monteiro-Riviere, R. Aggarwal, J.P. Davis, R.J. Narayan, W.T. Self, J. McGinnis, and S. Seal, *Nanoceria as Antioxidant: Synthesis and Biomedical Applications.* JOM (1989), 2008. **60**(3): p. 33-37.

122. Zhou, X., L.L. Wong, A.S. Karakoti, S. Seal, and J.F. McGinnis, *Nanoceria inhibit the development and promote the regression of pathologic retinal neovascularization in the Vldlr knockout mouse.* PLoS One, 2011. **6**(2): p. e16733.

123. Raju, H.B., Y. Hu, A. Vedula, S.R. Dubovy, and J.L. Goldberg, *Evaluation of magnetic micro- and nanoparticle toxicity to ocular tissues.* PLoS One, 2011. **6**(5): p. e17452.

124. Giannaccini, M., M. Giannini, M.P. Calatayud, G.F. Goya, A. Cuschieri, L. Dente, and V. Raffa, *Magnetic nanoparticles as intraocular drug delivery system to target retinal pigmented epithelium (RPE).* Int J Mol Sci, 2014. **15**(1): p. 1590-605.

125. Giannaccini, M., L. Pedicini, G. De Matienzo, F. Chiellini, L. Dente, and V. Raffa, *Magnetic nanoparticles: a strategy to target the choroidal layer in the posterior segment of the eye.* Scientific Reports, 2017. **7**.

126. Jo, D.H., J.H. Kim, Y.S. Yu, T.G. Lee, and J.H. Kim, *Antiangiogenic effect of silicate nanoparticle on retinal neovascularization induced by vascular endothelial growth factor.* Nanomedicine, 2012. **8**(5): p. 784-91.

127. Sun, J.G., Q. Jiang, X.P. Zhang, K. Shan, B.H. Liu, C. Zhao, and B. Yan, *Mesoporous silica nanoparticles as a delivery system for improving antiangiogenic therapy.* Int J Nanomedicine, 2019. **14**: p. 1489-1501.

128. Paiva, M.R.B., G.F. Andrade, L.F.N. Dourado, B.F.M. Castro, S.L. Fialho, E.M.B. Sousa, and A. Silva-Cunha, *Surface functionalized mesoporous silica nanoparticles for intravitreal application of tacrolimus.* J Biomater Appl, 2021. **35**(8): p. 1019-1033.

129. Bodewein, L., F. Schmelter, S. Di Fiore, H. Hollert, R. Fischer, and M. Fenske, *Differences in toxicity of anionic and cationic PAMAM and PPI dendrimers in zebrafish embryos and cancer cell lines.* Toxicol Appl Pharmacol, 2016. **305**: p. 83-92.

130. Taranejoo, S., J. Liu, P. Verma, and K. Hourigan, *A review of the developments of characteristics of PEI derivatives for gene delivery applications.* Journal of Applied Polymer Science, 2015. **132**(25).

131. Alinejad-Mofrad, E., B. Malaekeh-Nikouei, L. Gholami, S.H. Mousavi, H.R. Sadeghnia, M. Mohajeri, M. Darroudi, and R.K. Oskuee, *Evaluation and comparison of cytotoxicity, genotoxicity, and apoptotic effects of poly-l-lysine/plasmid DNA micro- and nanoparticles.* Hum Exp Toxicol, 2019. **38**(8): p. 983-991.

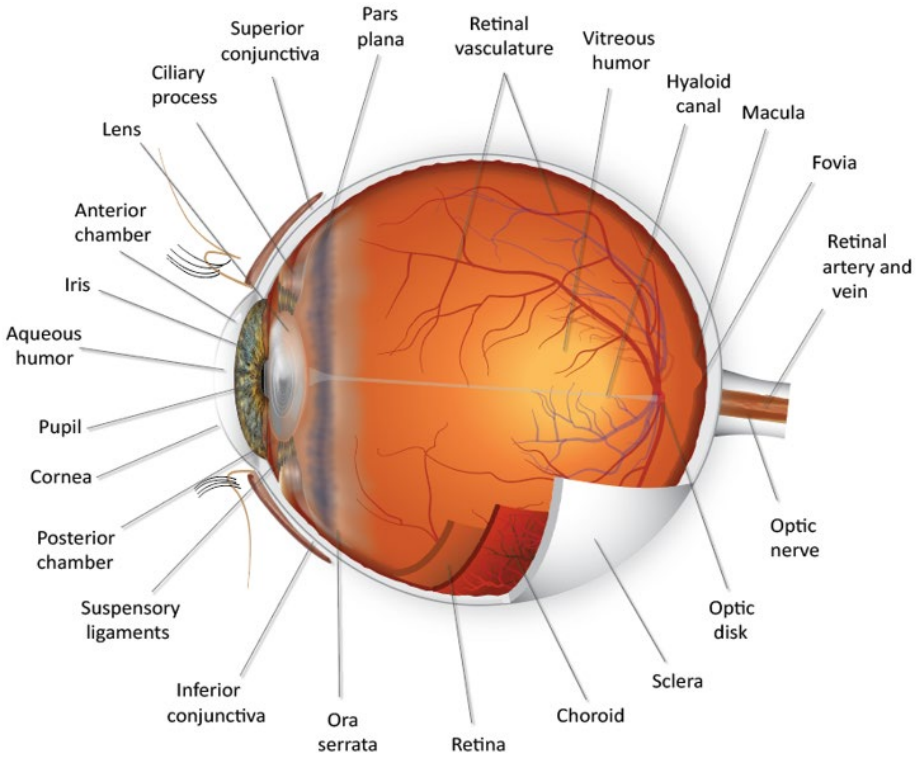

Figure 1.1. A pictorial representation of the anatomy of the eye.

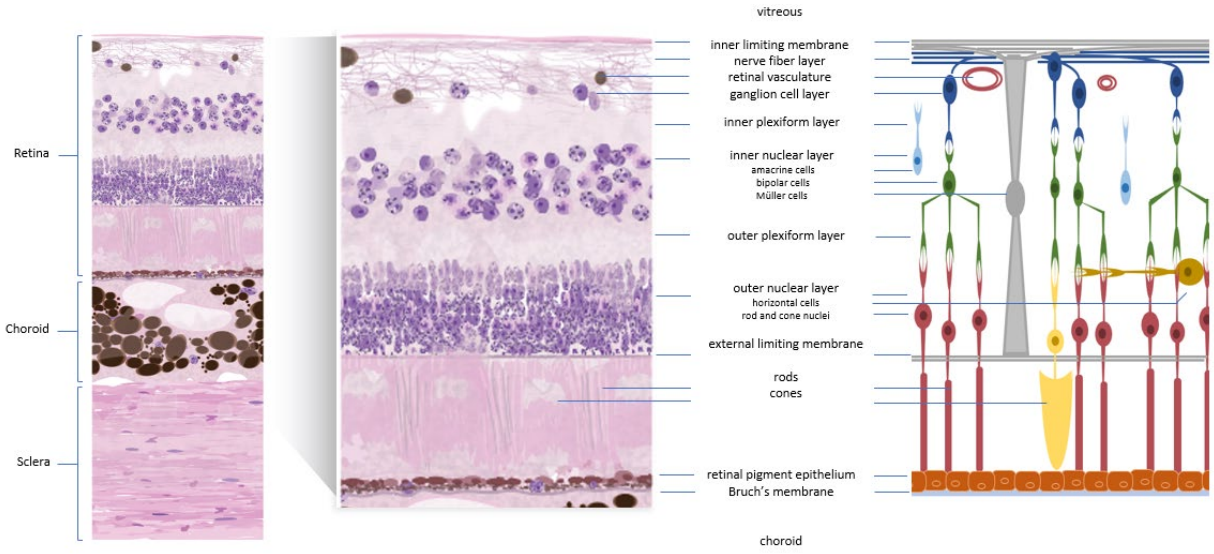

Figure 1.2. A pictorial representation of the anatomy of the retina.

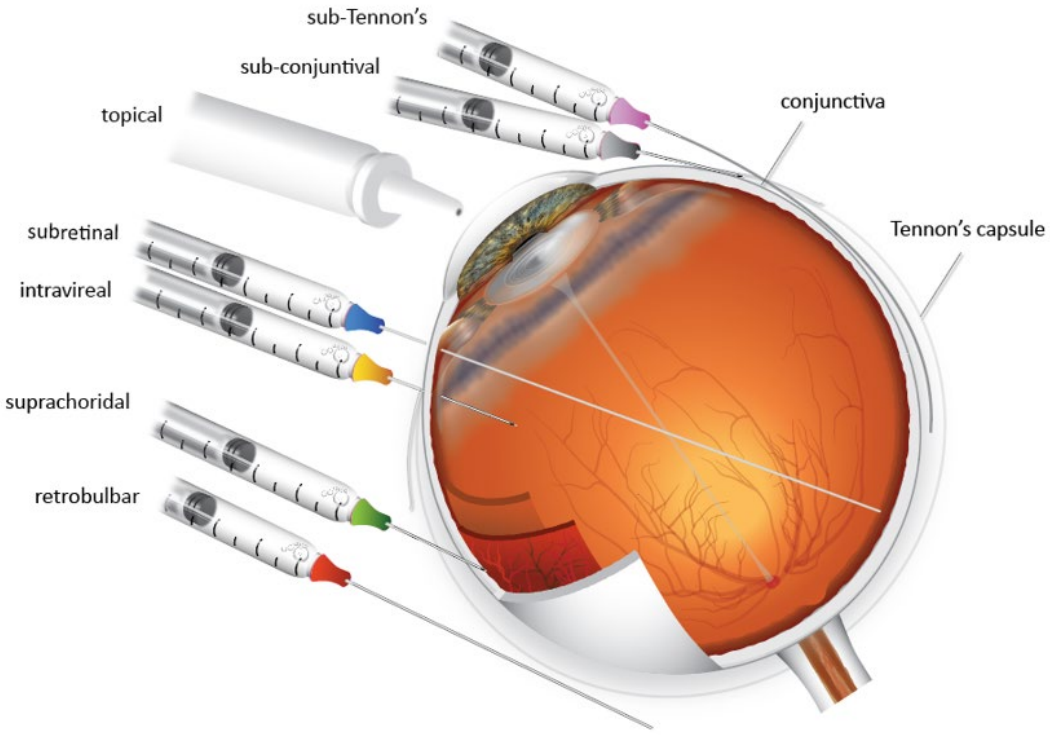

Figure 1.3. A pictorial representation of ocular therapeutic administration.

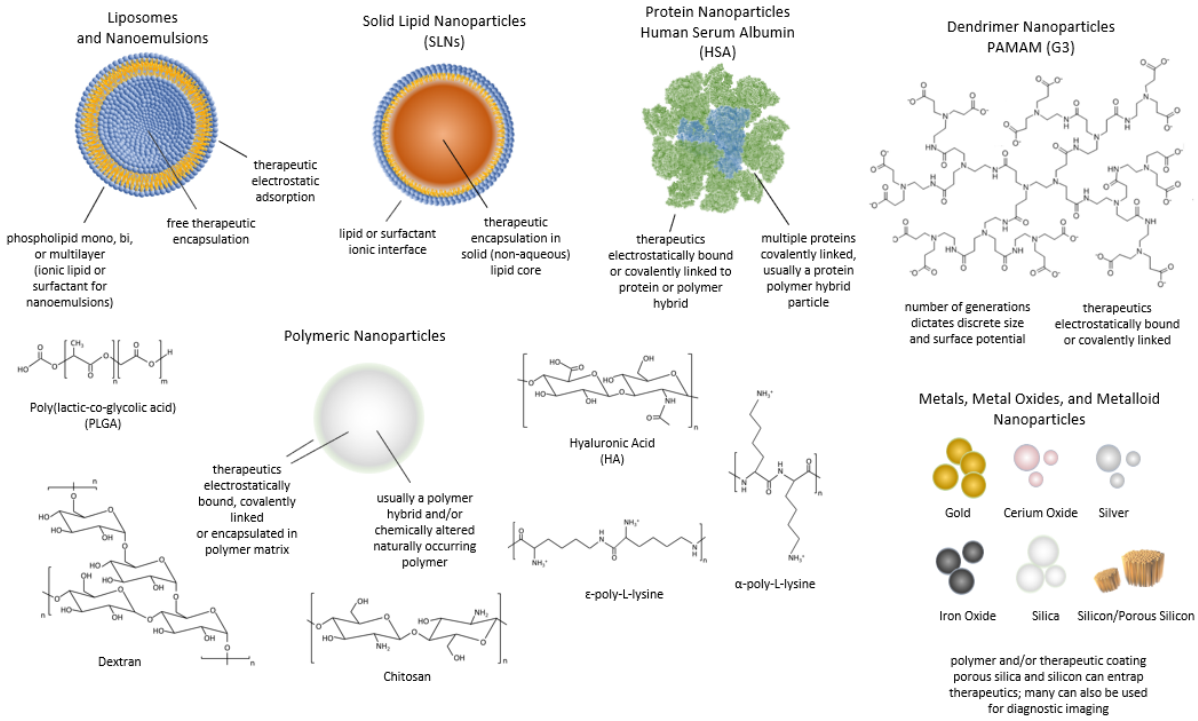

Figure 1.4. A pictorial representation of nanoparticle formulations discussed in the text.

Chapter 2

Treatment of Retinal Neovascularization with Fusogenic Porous Silicon Nanoparticles Containing Vascular Endothelial Growth Factor siRNA

2.1 Abstract

The purpose of this study was to evaluate an intravitreally injected nanoparticle platform that delivers siRNA targeting vascular endothelial growth factor (VEGF) for its ability to inhibit neovascular leakage in a rabbit model. Porous silicon nanoparticles loaded with rabbit VEGF-A siRNA were coated with a fusogenic lipid composition (F-pSiNPs) which incorporated the targeting and internalization peptide iRGD that homes to angiogenic retina integrins. The F-pSiNPs were evaluated by intravitreal injection (IVI) for toxicity and pharmacodynamics in healthy rabbit eyes, and for efficacy in DL-α-aminoadipic acid rabbit model of retinal neovascularization. Efficacy was measured by a reduction of leakage using fluorescein angiography (FA) as compared to sham injection controls and confirmed with VEGF-A ELISA of the vitreous and histology. A statistically significant reduction in rabbit ocular FA leakage was observed for treated diseased eyes as compared to the control sham eyes $p = 0.00137$, which persisted for 12 weeks. A corresponding reduction in concentration of vitreous VEGF-A protein was observed for 12 weeks post treatment. No toxicity or inflammation was observed in the healthy F-pSiNP-injected eyes and normal function was observed with ERG. Histological sections from 72 hr post-injection revealed penetration of the F-pSiNPs throughout the inner retina and up to the retinal pigment epithelium. The siRNA-loaded F-pSiNP constructs were able to provide a persistent knockdown of VEGF gene expression and reduce leakage in a rabbit model of retinal neovascularization as a potential new intraocular therapeutic.

2.2 Introduction

Diabetic retinopathy is a leading cause of blindness in the industrialized world with a global prevalence of an estimated 95 million people [1]. Administration of anti-vascular endothelial growth factor (anti-VEGF) therapies is the standard of care for the treatment of proliferative diabetic retinopathy (PDR) and diabetic macular edema (DME) [2, 3]. In 2015, there were over 2.6 million anti-VEGF injections in the United States [4], with a conservative estimate of 3.5 million annual injections by 2022. The chronic pathology of the disease requires a protracted level of therapeutic intervention to maintain remission. Due to the high turnover of anti-VEGF in the vitreous, repeated monthly injections are required [5-9]. In the Horizon study of community based anti-VEGF injections in wet age-related macular degeneration (AMD), the vision gain attained from repeated 4-week injections of the anti-VEGF drug ranibizumab was lost once the patients transitioned to an as-needed regimen [10]. This result was also seen in the Seven-Year Outcomes follow up study of ranibizumab [11]. However, continued repeat intravitreal injections run the risk of intraocular inflammation, infection, and ocular hemorrhage [12]. Repeated high concentration injections of anti-VEGF can result in retinal geographic atrophy [13] and can result in adverse reactions from systemic circulation [14]. There are similar issues in PDR where premature discontinuation of anti-VEGF may result in resurgence of disease [15]. To treat or prevent PDR, it has been suggested that anti-VEGF drugs be used chronically and that this likely produces less retinal damage than panretinal photocoagulation therapy [16]. Monthly injections however are not practical for many and a more permanent or

long-acting treatment is desired. An alternative approach is to use RNA interference (RNAi) to silence VEGF mRNA expression.

Small interfering RNA (siRNA) therapeutics have a catalytic advantage over their antibody-based counterparts. Once the siRNA-RNA induced silencing complex is formed it can cleave multiple VEGF messenger RNAs, as opposed to anti-VEGF which stoichiometrically sequesters a single VEGF protein [17]. Approximately ten years ago, phase 3 clinical trials tested the free drug VEGF-siRNA bevasiranib in combination with the anti-VEGF drug ranibizumab to treat neovascularization-linked AMD [18]. The results of this study suggested that free siRNA is efficacious in inhibiting neovascularization, however the combination therapy did not outperform ranibizumab alone [18]. In addition, while bevasiranib was being evaluated for clinical use, other researchers demonstrated that extracellular VEGF-siRNA can indiscriminately arrest AMD neovascularization by binding the extracellular toll-like receptor 3 (TLR3), in lieu of its intracellular target VEGF mRNA, and can induce apoptosis [19, 20]. Subsequent years have seen many advances in development of siRNA as a therapeutic. There are currently three U.S. Food and Drug Administration (FDA)-approved siRNA therapeutics, 9 in phase 3 clinical trials and 13 in phase 2 clinical trials (clinicaltrials.gov). One key factor leading to the surge of recent clinical activity is the substantially greater stability of the latest siRNA constructs. This enhanced stability is provided by a number of specific modifications on individual ribose sugars, which reduce the susceptibility to nuclease cleavage and enhance gene knockdown [21]. While these modifications have increased the *in vivo* half-life of siRNAs by over three orders of magnitude [22], an obstacle for intraocular applications of siRNA therapy remains: how to effectively deliver

functional siRNA through the vitreous and inner limiting membrane and target the diseased retinal cells. We hypothesized that these obstacles could be overcome by utilizing recent advances in nanomedicine, in particular: (1) nanoparticles with the ability to carry high quantities of siRNA; (2) peptides capable of selectively targeting and penetrating cells; and (3) fusogenic coatings that avoid endosomal uptake to enhance cytosolic delivery.

The nanoparticle system chosen for this study was composed of mesoporous silicon, a material that has been shown to be well tolerated by tissues of the eye [23-27] and that can protect the siRNA payload from RNase degradation [28]. Nucleic acid therapeutics such as siRNA possess a high negative charge due to their phosphate backbone, and generally this charge must be neutralized in order to load sufficient quantities into a nanoparticle. While surface modification with a positively charged species such as a cationic lipids or polymers is a common solution that has also been used for silicon nanoparticles [29-33], for this work a biocompatible calcium-silicate condenser chemistry was used. When applied to porous silicon nanoparticles (pSiNPs), this chemistry has been shown to yield mass loadings of nucleic acid in excess of 20% [34, 35] and to prolong delivery of the siRNA payload [34], while retaining the ability of nanophase silicon to dissolve into harmless byproducts *in vivo* [36]. In order to bypass endosomal uptake/degradation, the pSiNPs were coated with a fusogenic lipid coating [35, 37, 38]. We chose to target retinal angiogenesis using the tumor-homing and internalization peptide iRGD that has been widely studied and shown to penetrate deep into tumor vasculature [39-42]. Like its progenitor, the RGD peptide, iRGD targets cell-surface αv integrins *via* the RGD peptide sequence. The i-prefix on iRGD indicates “internalizing” and this relates to the affinity of the

RGDK sequence in iRGD for the cell surface receptor neuropilin-1, which enables cellular internalization [39-42]. Both αv integrins and neuropilin-1 are known to be expressed on the surface of cells associated with choroidal neovascularization [43, 44], although their upregulation in retinal angiogenesis is not known. This study sought to test the ability of this targeted nanocarrier system to deliver VEGF-siRNA within the retina.

The *in vivo* rabbit model chosen for PDR and DME exhibits retinal neovascularization and vascular leakage indicative of pathologic vessel growth associated with these diseases. The Müller cell toxin DL-a-aminoadipic acid (DL-AAA) is injected intravitreally and has been shown to induce the pathology of the model within 2 weeks of injection [45-47]. Müller glial cells are specific to the retina and are responsible for protecting neurons, maintaining homeostasis and neuronal metabolic support [48]. They have been shown to undergo gliosis in PDR and in doing so contribute to the progression of the disease by the release of angiogenic cytokines such as VEGF [48, 49]. VEGF in turn promotes neovascular growth and induces vascular leakage [2, 3]. A single injection of DL-AAA exhibited a retinal neovascular pathology in rabbits from 2 to 65 weeks post-injection [45, 46]. This DL-AAA rabbit model of retinal neovascularization presents vascular leakage that can be readily monitored by fluorescein angiography (FA), and its relevance to the disease pathology has been validated by demonstration of attenuation of FA leakage upon injection of the anti-VEGF drug aflibercept [45, 46].

In this study we loaded pSiNPs with rabbit VEGF-siRNA using the above calcium silicate condensation chemistry, then applied the fusogenic lipid coating (F-pSiNP) and conjugated iRGD to the exterior of the nanoparticle *via* a 2 kDa poly(ethylene glycol)-maleimide linker. To test

the efficacy of the resulting VEGF-siRNA F-pSiNPs by single intravitreal injection, we monitored the DL-AAA rabbit model over a 12-week period by FA, VEGF assays of vitreous eye taps, and histology. To our knowledge this is the first demonstration of targeted intravitreal delivery of siRNA utilizing iRGD to successfully treat an animal model of retinal neovascularization.

2.3 Methods

Materials: Highly boron-doped *p*++ type silicon wafers,~1 mΩ cm resistivity, polished on the (100) face (Sil'tronix, Inc., Archamps, France); hydrofluoric acid, 48% aqueous, ACS grade (Thermo Fisher Scientific Inc., Waltham, MA); anhydrous calcium chloride, (Spectrum Chemicals, New Brunswick, NJ); 1,2-dimyristoyl-sn-glycero-3-phosphocholine (DMPC), 1,2-dioleoyl-3-trimethylammonium-propane (DOTAP), and 1,2-distearoylsn-glycero-3-phosphoethanolamine-N-[maleimide(polyethyleneglycol)-2000] (DSPE-PEG-maleimide), (Avanti Polar Lipids); 1,1'-dioctadecyl-3,3,3',3' -tetramethylindocarbocyanine perchlorate (DiI), and Lipofectamine 2000, (Thermo Fisher Scientific Inc.); iRGD peptide: 5-FAM-C[X]CRGDKGPDC-NH2, from (AnaSpec, Freemont, CA), where (X) = 6-amino hexanoic acid; s-s bonds between C3 and C11; rabbit VEGF-A siRNA [50] was modified with the addition of 2' methoxy to the first two 5' nucleosides of the antisense strand: 5'mA.mU.G.U.C.C.A.C.C.A.A.G.G.U.C.U.C.G.A.dT.dT3'; sense: 5'U.C.G.A.G.A.C.C.U.U.G.G.U.G.G.A.C.A.U.dT.dT3'; . (Horizon-Dharmacon Inc., Chicago, IL); human ARPE-19 cells, (American Type Culture Collection, ATCC.org); rabbit primary retinal microvasculature endothelial cells, endothelial cell growth supplement (500X), gelatin-based coating solution (Cell Biologics Inc., Chicago, IL); New Zealand Pigmented rabbits (males and

females), 3-4 months old (Western Oregon Rabbitry, Philomath, OR); balanced salt solution (BSS), DL-α-aminoadipic acid (DL-AAA), (MilliporeSigma, Burlington, MA); RNeasy Mini Kit (Qiagen, Germantown, MD); ToxinSensor Chromogenic LAL Endotoxin Assay Kit, (GenScript, Piscataway, NJ).

Preparation of Fusogenic Porous Silicon Nanoparticles: The fusogenic porous silicon nanoparticles (F-pSiNPs) were synthesized as previously described [37].Porous silicon was produced by electrochemical anodization of highly boron-doped *p*++ type silicon wafers (exposed area ~ 9 cm^2) using a square waveform consisting of a current density of 50 mA cm^{-2} applied for 0.6 s followed by a current density 400 mA cm^{-2} for 0.36 seconds, repeated for 500 cycles in an electrolyte consisting of 3:1 aqueous 48% HF:absolute ethanol (CAUTION: HF is highly toxic and proper care should be exerted to avoid contact with skin or lungs). The resulting porous layer was removed from the crystalline silicon substrate by application of a current density pulse of 3.7 mA cm^{-2} for 250 s in an electrolyte consisting of 1:20 aqueous 48% HF:absolute ethanol. The porous layer was washed with ethanol and ultrasonicated in a 50T ultrasonic bath (Avantor VWR, Radnor, PA) in 2 mL of ethanol for 16 hr to generate pSiNPs by ultrasonic fracture. The particles were centrifuged at 3200 x g for 5 min and the supernatant, containing the nano-sized particles, was adjusted to 2 mg mL^{-1} by dried mass and stored in ethanol at room temperature. 24 hr before use the particles were centrifuged at 20,000 x g for 30 min to pellet, transferred to RNAse-free water, and dispersed in the liquid by ultrasonication. This process was repeated one time and the particles were adjusted to a final concentration of 1 mg mL^{-1} and maintained at room temperature until further use. The siRNA

was loaded into the pSiNPs as previously described [34]. All procedures were performed in a biosafety hood using sterile technique wherever possible. siRNA was resuspended in RNAse-free water to a final concentration of 150 nM by shaking gently at room temperature for 20 min. All reagents were stored on water ice. 150 µL of 1 mg mL^{-1} pSiNPs was mixed with 150 µL of 150 nM siRNA on ice. This mixture was placed in an ultrasonic bath at ~4-6 ^{o}C. While being subjected to ultrasonication, 700 µL of 2M calcium chloride was added and gently mixed and the mixture was ultrasonicated for an additional 15 min. The resulting particles were pelleted at 5000 x g in a centrifuge at 4 C for 10 min. The supernatant was removed and assayed by absorbance for siRNA loading. The particles were resuspended in 1 mL of BSS, briefly ultrasonicated into solution, and immediately transferred for lipid coating. The fusogenic coating was prepared by adding DOTAP:DMPC:DSPE-PEG2000-Malemide at a mole ratio of 20:76:4 respectively. The lipids were mixed by adding 19.6 µL DOTAP, 72.6 µL DMPC and 15.2 µL DSPE-PEG2000-Malemide from 10 mg mL^{-1} stock solutions in chloroform and dried overnight at room temperature, (20 µL of the membrane dye DiI, 1.25 mg mL^{-1} in ethanol, was added to the lipid mixture before drying for the histology and *in vitro* imaging studies). The siRNA-loaded pSiNPs were added to the dried lipid mixture, briefly ultrasonicated, and heated to an extrusion temperature of 40-45 ˚C while stirring. The particles were extruded through a 0.2 µm membrane 20 times. 100 µL of the iRGD or control peptide at 1 mg mL^{-1} was then added and the mixture was stored at 4 ^{o}C for 16 hr to effect coupling of free thiol on the peptide to the maleimide on the DSPE-PEG2000-Malemide lipid component. The resulting particles (siRNA-loaded, F-pSiNPs) were then washed with BSS using 30 kDa molecular weight cutoff Amicon Ultracel centrifuge filter (MilliporeSigma) at 4500 x g for 30 min repeated 3 times to a final

volume less than 200 µL. The flowthrough was saved and assayed by absorbance for siRNA loading using a NanoDrop (Thermo Fisher Scientific). The final particle volume was adjusted to equal 500 µg mL^{-1} siRNA based on encapsulation efficiency. Particle morphology and charge was analyzed with dynamic light scattering (DLS) using a Zetasizer (Malvern Panalytical, Malvern, UK) and transmission electron microscopy (TEM).

Cryogenic electron microscopy: Titan Krios G3 microscope with an X-Feg electron source, a Gatan K2 Summit with Bio-Quantum energy filter using a slit with of 20eV. Samples were prepared on 2/1 quantifoil grids with the surface prepared using the Solarus plasma cleaner. 3.5 µL of sample was aliquoted onto the grid and plunge frozen in the Vitrobot Mark IV. High resolution imaging was performed at a nominal magnification of 33,000x with a calibrated pixel size of 4.33 Angstrom.

***In vitro* release studies:** In vitro release was performed by incubating the siRNA-loaded F-pSiNPs in 500 µL PBS (pH 7.4) at 500 µg mL^{-1} or 1 mg mL^{-1} at 37 ^{o}C in an orbital shaker (Gyromax 737 shaker/incubator, Amerex instruments). The particles were transferred to a 30 kDa molecular weight cutoff Amicon Ultracel centrifuge filter and centrifuged at 4500 x g for 30 min. The flowthrough was measured for both volume by mass (assuming 1 g = 1 mL) and for siRNA absorbance using a NanoDrop (Thermo Fisher Scientific). The remaining particles were resuspended with PBS buffer and returned to 37 ^{o}C shaking until the next timepoint.

***In vitro* cell studies:** Human retinal pigmented epithelial cells (ARPE-19) were grown to 75% confluency in DMEM-F12, 10% fetal bovine serum, 1% penicillin/streptomycin media to a density of 300k cells mL^{-1} in a 6 well plate at 37 ^{o}C, 5% CO_2. The media was replaced with media

containing 100 µM $CoCl_2$ and incubated for 16 hr to induce hypoxia [51]. The cells were washed one time with fresh media followed by the addition of media containing nanoparticles or controls at concentrations specified in the text. After 24 hr of incubation the cells were trypsin digested and prepared for RT-qPCR as described below. Rabbit primary retinal microvasculature endothelial cells were treated as described above except the media contained 1x endothelial cell growth supplement and the plates were coated with gelatin-based coating solution prior to use. Sections were imaged using a Nikon A1R Confocal STORM super-resolution system (Nikon Instruments Inc., Melville, NY).

Animal studies: All animal studies were performed using New Zealand pigmented rabbits, which were treated in accordance with the University of California, San Diego, IACUC standards of practice and the ARVO statement for the use of animals in ophthalmic and vision research. Intraocular injections, aqueous taps, and fluorescein angiography (FA) were performed under 25-30 mg/kg ketamine and 5mg/kg xylazine administered by subcutaneous injection. For intraocular injections the eye was surgically prepped with ophthalmic betadine, then sterilely irrigated with BSS. 1-2 drops of proparacaine were administered to numb the cornea. All intraocular injections were performed under an Alcon ophthalmic operating microscope (Alcon, Fort Worth, TX).

***In vivo* toxicity:** Fusogenic pSiNP toxicity and inflammation was tested by injecting 50 µL of siRNA-loaded F-pSiNPs into one healthy rabbit eye with the contralateral injected with balanced salt solution (BSS) as control. Both eyes were assessed by fundus exam, imaged, and measured for function by electroretinography (ERG) prior to injection, and on days 0, 14, and

28 post injection. After sacrificing the animals, globes were enucleated and processed for histology.

DL-AAA model: 80 µL of an 80 mM DL-a-aminoadipic acid (DL-AAA) solution was injected in one eye of a rabbit to initiate the retinal neovascularization model, as previously described (9, 10). The contralateral eye was injected with 80 µL BSS as control. The DL-AAA solution was prepared on the day of use under sterile conditions by dissolving 128.9 mg of DL-AAA in 1 mL 1M HCl, diluted with BSS to a final volume of 10 mL, pH adjusted to 7.4 with 2M NaOH and filtered with 0.22 µm syringe filter. DL-AAA eyes that resulted in partial retinal detachment at two weeks post disease induction were excluded from the FA study because the leakage could no longer be assessed with FA imaging (~50% of animals injected). These animals were used for analyzing nanoparticle efficacy by measuring VEGF-A from both the vitreous and aqueous humor taps were analyzed by ELISA for both treated and sham n = 4 each at time points of 1-, 4 -, and 12-weeks post-treatment. Three animals were excluded because disease did not develop, and one animal was excluded due to an occlusion that prevented FA perfusion.

Nanoparticle efficacy measured by fluorescein angiography (FA) image analysis: The progression of the pathology was evaluated by optical coherence tomography (OCT) (data not shown) and fluorescein angiography (FA) at the early (0–3 minutes), mid (4-6 minutes), and late (10–13 minutes) phases. 50 µL of F-pSiNPs-iRGD containing a total of 25 µg of VEGF-A siRNA or a BSS-only sham was then injected into the disease model DL-AAA eye of a rabbit. The contralateral eye was left untreated. FA imaging and 50 µL aqueous taps were preformed every two weeks until 14 weeks post disease induction and stored at -80 ^{o}C for ELISA VEGF-A analysis.

The FA images were montaged using the “mid” timepoint, described above, to include the optic never, nasal and temporal medullary rays using Heidelberg Eye Explorer imaging software. The FA images were then exported as TIFF files and analyzed using ImageJ [52] by masked ophthalmologists at each time point to determine the pathologically observable effects of neovascularization: leakage area and intensity, vessel tortuosity and intraretinal microvascular anomalies (IRMA). The area of leakage was circled and measured for area and mean pixel intensity. This mean pixel intensity was corrected for gain, *i.e.*, exposure, by using the mean pixel intensity within the optic nerve contained by that image. The resulting corrected intensity was multiplied by the pixel area of leakage circled to give a quantitative measure for leakage. These recorded measurements were collected from each ophthalmologist and averaged. For the final analysis, the leakage measured on the day of treatment, prior to treatment, was used as baseline for all subsequent leakage assessments following the relationship: [(leakage timepoint - baseline leakage)/(baseline leakage) +1] x 100% = percentage of leakage increase. Retinal vessel tortuosity was graded 0 to 3 (0 = not tortuous, 1 = vessels reach visual streak, 2 = vessels exceed visual streak, and 3 = 2 plus neo-vessel development). Intraretinal microvascular abnormalities (IRMAs) were graded 1 to 3 (1 = 0-25 lesions, 2 = 25-50 lesions, and 3 = >50 lesions).

ELISA: Rabbit VEGF-A aqueous and/or vitreous concentrations were determined by rabbit-specific 96 well VEGF-A ELISA (MyBiosource, San Diego, CA). Aqueous samples were tested directly, and vitreous samples were centrifuged at 10000 x g for 10 min at 4 ^{o}C and the

supernatant was tested. The absorbance was read at 450 nm on a SpectraMax iD5 plate reader (Molecular Devices, Downingtown, PA).

Histology: Enucleated eyes were punched at 3 and 9 o'clock locations with a 1 mm diameter biopsy punch, at a distance 1 mm from the limbus. The eyes were placed in 25 mL 10% formalin for 72 hr at 4 °C, then placed in 10%, 20% and 30% sucrose at 4 °C for ~24 hr each in order of increasing concentration. Finally, the eyes were bisected in the sagittal plane with a razor blade and mounted in Neg-50 Frozen Section Medium (Thermo Fisher Scientific) in an isobutane/dry ice bath. The eyes were sectioned at a maximum thickness of 10 µm and either mounted with Pro-long Gold with DAPI (Thermo Fisher Scientific) or stained with hematoxylin and eosin. Sections were imaged using Nikon A1R Confocal STORM super-resolution system.

Statistical Analysis: FA leakage data was analyzed using SAS (SAS Institute Inc.), using GLM repeated measures analysis of variance. ELISA data was analyzed by one-way ANOVA.

2.4 Results

The pSiNPs were prepared by electrochemical etch of silicon wafers (**Figure 2.1A**) [53]. The porosity, the average mesopore size, and the average nanoparticle size are precisely controlled by the electrochemical waveform used in the synthesis [54]. This provides a systematic means to tailor the material for a specific drug molecular size, loading capacity and/or final particle diameter. To effectively protect and deliver siRNA *in vivo,* the siRNA drug payload was condensed within the pores of the nanoparticles using a calcium silicate sealant chemistry [34]. This condensation chemistry capitalizes on the unique ability of calcium ion to both stabilize

siRNA *via* ion pairing and to form a precipitate with silicic acid [34]. The silicic acid species, primarily in the form $Si(OH)_4$, is locally generated at the surface of the oxidized porous silicon nanoparticles *via* aqueous dissolution; reaction with excess calcium ion creates an insoluble calcium silicate phase (idealized as dicalcium orthosilicate, Ca_2SiO_4) effectively trapping the siRNA within the pores of the nanoparticle [34] (**Figure 2.1B**).

The necessity of the silicic acid species to effect the sealing of the pores limits the reaction proximity to the silicon surface. Once formed, the insoluble calcium silicate sealant slows degradation of the porous silicon particles, and thus the release of siRNA. To avoid engaging the endocytosis pathway, which inhibits the effectiveness of siRNA, the siRNA-loaded pSiNPs were coated with a fusogenic lipid coating (F-pSiNP) as previously described [35, 37], and conjugated to a 5FAM-labeled iRGD targeting peptide (**Figure 2.1B**). This combination of targeting peptide and fusogenic coating has been shown to act by first engaging the nanoparticle with the cellular surface and then fusing with the cellular membrane, at which point the lipid coating is shed and the nanoparticle with its siRNA payload is released directly into the cytosol [37]. For the siRNA payload, rabbit VEGF-A-siRNA was used. The antisense sequence was: 5'mAmUGUCCACCAAGGU- CUCGAdTdT3' [50], where the 2’ methoxy groups at the 5’ end were introduced to protect the siRNA against exonucleolytic digestion. The iRGD targeting peptide construct consisted of 5-FAM-C(X)CRGDKGPDC, where 5-carboxyfluorescein (5-FAM) was conjugated to the N-terminus, followed by a free cysteine for nanoparticle conjugation, a hexanoic acid linker (X), and the nine amino acid iRGD cyclized with a disulfide bond between C3 and C11. As a control, a scrambled peptide consisting of 5-FAM-

C(X)CRGEDGPKC was used; here the aspartic acid from the integrin-targeting sequence RGD was substituted with glutamic acid, previously shown to inhibit targeting, and the adjacent lysine, required for neuropilin-1 internalization, was substituted with aspartic acid [42] (**Figure 2.2**). The F-pSiNPs had a core of diameter 68.6 +/- 10.0 nm consisting of the pSiNPs loaded with VEGF-A-siRNA and sealed with calcium silicate, and the average final diameter after lipid coating/extrusion and peptide conjugation was 145 +/- 6.6 nm, with a polydispersity index of 0.12 +/- 0.05 and positive zeta potential of +17.8 +/- 1.2 mV measured by dynamic light scattering (**Figure 2.3A**). The F-pSiNPs had an average siRNA encapsulation efficiency of 20.3 +/- 6.4%, which corresponds to a mean mass loading of 28.8 wt.%, defined as mass of siRNA divided by the total mass of pSiNP + siRNA combined, and efficiency of conjugation of peptide to the particles was 17.3 +/- 4.3%, based on 5-FAM absorbance (**Figure 2.3B**). The particle morphology was confirmed by cryogenic electron microscopy (cryo-EM) (**Figure 2.3C**) and measured by ImageJ to have diameter of 113.9 +/- 23.8 nm. Endotoxin level in the final F-pSiNP formulation was 0.365 +/- 0.04 EU mL^{-1}, below the threshold for detectable ocular inflammation in rabbit vitreous of 1.0 EU mL^{-1} [55]. The particles were tested for *in vitro* release of siRNA by incubating samples containing 0.5 mg mL^{-1} and 1.0 mg mL^{-1} siRNA in PBS (pH 7.4) at 37 °C, in an orbital shaker. These concentrations are equivalent to 1x and 2x of the intended *in vivo* injection concentration based on the average volume of a rabbit eye of 1.5 mL. The results showed a day 1 siRNA burst release of 42% +/- 15% for 8 µg (1x) and 56% +/- 6% for 16 µg (2x), n = 4 each (**Figure 2.3D**) and essentially 100% of siRNA was released after 13 days for both concentrations tested (**Figure 2.3E**).

To test *in vitro* uptake, the F-pSiNPs were incubated with human retinal pigment epithelial cells (ARPE-19) and primary rabbit retinal microvascular endothelial cells, and uptake was assessed by confocal microscopy (**Figure 2.4A-B**). The fusogenic properties of the nanoparticles are apparent in the confocal images, as the transfer of the DiI lipid stain (from the lipid coating of the nanoparticle) and the 5FAM label (attached to the iRGD targeting peptide) to the cell membranes was observed after 20 min incubation at 37 °C. Some evidence of whole particle uptake was also observed (**Figure 2.4A-B**).

For *in vivo* tolerability studies, 50 µL of nanoparticles at two concentrations, 0.5 mg mL^{-1} siRNA and a 1:10 dilution in balanced salt solution (BSS), were injected into the right eye of New Zealand pigmented rabbits and tested for inflammation and toxicity. The left contralateral eye was injected with 50 µL of BSS as a control. Color fundus images of the eyes were obtained before injection, at 1 week, 2 weeks and 6 weeks, followed by enucleation and histology. No evidence of ocular inflammation or toxicity was observed. Treated eyes displayed comparable electroretinogram (ERG) flicker β-amplitude values compared to fellow (control) eyes at each time point. Diffusion and uptake of the intravitreally injected iRGD-F-pSiNPs were evaluated at 24 and 72 hr post-injection, in DL-AAA rabbit eyes using F-pSiNPs that included DiI or sham injection controls (**Figure 2.5A-C**). At 24 hr most of the particles resided in the vitreous (data not shown), whereas at 72hr particles were observed to have been taken up by Müller cells and had migrated toward the outer nuclear layer (**Figure 2.5C-D**).

Finally, efficacy of the iRGD-F-pSiNP formulation was tested in the DL-AAA retinal angiogenesis rabbit model, and leakage was measured by fluorescein angiography (FA) imaging

at two weeks post injection to obtain a baseline (**Figure 2.6A**). Only one eye of each animal was injected with DL-AAA (80 uL 80 mM DL-AAA, pH 7.4) and the contralateral eye of each animal was injected with BSS as an injection control. By week 2, the formation of tortuous vessels and substantial vascular leakage was evident (**Figure 2.7**), characteristic of the disease model as previously described [45, 46]. At week 2, 50 µL of the F-pSiNP treatment (or BSS control) was injected, equivalent to 10 µg kg^{-1} VEGF-siRNA, into the DL-AAA disease model eyes. A dose of 10 µg kg^{-1} siRNA was selected, based on the bevasiranib siRNA concentration used in the age-related macular degeneration clinical trial [56] which equates to 25 µg in a 50 µL injection volume for a 2.5 kg rabbit. The treatment and control animals were imaged by FA every two weeks thereafter to monitor changes in vascular leakage. A substantial reduction in leakage was observed (**Figure 2.6B**). The animals were followed for 12 weeks post-treatment (**Figure 2.6D**). The images were montaged, masked, and measured using ImageJ for leakage area and intensity at each time point by two ophthalmologists. The identities of the montaged images were masked from the ophthalmologists to avoid bias. The relative intensity of each image was corrected to the intensity of the optic nerve and compared to baseline using the equations in **Figure 2.6C**. The results showed a statistically significant difference in fluorescein leakage over time for treated verses control animals (p = 0.0137, n = 5 treated and n = 4 sham, **Figure 2.6D**). Both degree of tortuosity and number of intraretinal microvascular abnormalities (IRMAs) were evaluated, and while both tortuosity and IRMAs were observed in both the BSS and treated eyes, no statistically significant change was seen over the course of the 12-week treatment (data not shown). The effect of the F-pSiNP treatment on VEGF-A expression was assessed by VEGF-A ELISA performed on the aqueous humor and the vitreous humor 1, 4 and 12 weeks

after treatment (**Figure 2.6E**). Significant reduction in the concentration of VEGF-A was observed in the vitreous fluid of treated eyes at 1-, 4- and 12-weeks post-treatment (p = 0.0348, p = 0.0014, and p = 0.0262, respectively, n = 3 or 4), compared to each animal's untreated, naïve fellow eye. This animal model has been shown to produce elevated levels of VEGF-A in both the vitreous and aqueous compartments [46]. However, the VEGF-A concentrations measured in the aqueous humor were at or near the limit of detection of the ELISA assay (data not shown), so no comment can be made on the difference in VEGF-A expression in the aqueous compartment for treated *vs* untreated eyes.

2.5 Discussion

The goal of this project was to demonstrate the possibility of transforming the current standard of care in treatment of proliferative diabetic retinopathy (PDR) and diabetic macular edema (DME) by using a targeted VEGF-siRNA nanoparticle therapy that might be able to inhibit retinal neovascularization for substantially longer periods of time than is achieved with the current standard of care. By shutting down VEGF production, rather than binding it after secretion, this approach offers the potential for more complete inhibition of disease progression. Other groups have recently demonstrated similar approaches to intravitreal injected nanoparticle siRNA therapeutics. Huang and Chau evaluated liposome nanoparticles containing non-specific FAM-siRNA for differences in retinal uptake associated with lipid surface charge and found nanoparticles with +35 mV zeta potential showed the optimal uptake in the mouse retina [57]. Nanoparticles containing VEGF receptor-1 siRNA complexed with hyaluronic

acid and protamine, followed by lipid coating, were found to protect against choroidal neovascularization in a laser-induced choroidal neovascularization (L-CNV) rat model [58]. Another group linked several VEGF-A siRNA strands together using 5' terminal disulfide bonds and condensed the poly-siRNA constructs into nanoparticles using polyethylene amine (PEI) [59]. Their work demonstrated a reduction in CNV size using a mouse model of L-CNV [59]. While the above "soft" delivery systems based on liposomal or polymeric constituents have shown great promise, the present work evaluated if a delivery system based on a solid nanoparticle component might be engineered to more effectively enhance intracellular delivery and extend the duration of action of the siRNA therapeutic.

While this work illustrates a new use of iRGD targeting peptide technology for the delivery of nanoparticles to retinal neovascular cells, it relies on key prior work that explored the concept of directing nanoparticles to ocular tissues, either by intravitreal injection or by topical administration. Cyclic-RGD, the predecessor of iRGD, was conjugated to PEG-polyethylene glycol-poly(lactic-co-glycolic acid) (PLGA)-dexamethasone grafted with PEI and the anti-VEGF antibody bevacizumab [60]. These particles were tested by intravitreal injection in a rabbit model of L-CNV and shown to be more efficacious than non-targeted particles [60]. Doxorubicin (DOX) was encapsulated within a liposome and targeted to the tyrosine kinase receptor EphA2 that is expressed on tumor neovascular cells as a potential treatment for CNV [61]. That work employed the YSA peptide conjugated to the surface of the nanoparticle, and intravitreal injection of the construct reduced neovascularization in a rat model of L-CNV [61]. TAT peptide-linked PLGA particles were used to deliver the anti-inflammatory drug flurbiprofen to a

rabbit model of anterior chamber inflammation and demonstrated corneal penetration and efficacy [62]. Chu *et al.* further demonstrated a topical corneal application of iRGD-TAT PLGA nanoparticles had some success targeting choroidal neovascularization, most likely by periocular absorption [63]. These studies taken as a whole support the rationale for the focus of the present work: to use iRGD-targeted nanoparticles to deliver siRNA targeting retinal angiogenesis by intravitreal administration.

Cryo-EM showed that the F-pSiNPs take on a spherical liposome-like morphology (**Figure 2.3C**) with overall dimensions comparable to liposomes (100-200nm). The mass loading of siRNA in the nanoparticles was higher than typical polymer or liposomal formulations due to the beneficial electrostatics and aqueous chemistry of the calcium-silicate system [37], and the release kinetics *in vitro* resulted in an initial burst of approximately half of the siRNA payload, followed by slow release for an additional 10-12 days (**Figure 2.3D**). For the ophthalmic applications of interest, release over several weeks to months might be more appropriate, and so extending release of these formulations over longer periods of time and tailoring the temporal release profile are future goals.

Another avenue of pursuit for extending therapeutic action into timescales of several months is in the design of the nucleic acid therapeutic. While an advantage of RNA-based gene modification is that it provides a more reversible effect than DNA, restriction enzyme, or genome editing-based approaches, the relatively transient nature of siRNA technology suggests that it may not provide the long-term VEGF suppression desired for treatment of diseases such as macular degeneration, proliferative diabetic retinopathy, or diabetic macular edema. Indeed,

this likely was a contributor to the clinical failures of the early bevasiranib siRNA constructs used to treat age-related macular degeneration [64]. In subsequent years, RNAi companies have developed chemically modified RNAs for their drugs, with modifications of multiple types (and at multiple sites) along the RNA strand to minimize immune stimulation, reduce off-target cleavage, and generally increase efficacy and duration of action. For example, the FDA-approved GIVLAARI™ and OXLUMO™ of Alnylam Pharmaceuticals both contain 44 ribose and 6 phosphate backbone modifications each. These recent entries show that substantially increased stability and longer residence times can be achieved by optimizing the backbone chemistry [21]; sustained *in vivo* efficacy for as long as 6 months has been demonstrated [22]. In the present work, the first two 5' nucleosides of the antisense strand contained 2' methoxy modifications in order to inhibit exonuclease cleavage and increase *in vivo* stability, which presumably contributed to the relatively long-lived activity observed for the single injection. The introduction of additional RNA modifications is an avenue for future work that might further enhance stability and extend activity of the formulation.

Confocal microscopy demonstrated the rapid fusion of the F-pSiNPs with two target cells of interest *in vitro* (**Figure 2.5A-B**). The fluorescent markers on the liposomal coating (Dil) and on the iRGD targeting peptide (5FAM) indicated successful fusion with the outer cellular membranes of both ARPE-19 cells and rabbit retinal microvascular endothelial cells; both the Dil and the FAM labels were seen predominately localized in the cell membranes. This is consistent with the established mechanism of uptake of this nanoparticle composition, wherein the lipid coating on the nanoparticle fuses to the cell membrane and is shed from the exterior

of the pSiNP, resulting in insertion of a mostly "bare" pSiNP into the cytosol [37].Furthermore, 72 hr after intravitreal injection in rabbit eyes, evidence of the lipid dye can be seen at the inner limiting membrane, at Müller glial cells and at the inner nuclear layer (**Figure 2.5A-B**), suggesting that at least some of the components, and likely some of the intact lipid-coated nanoparticles, are transported deeper into the retina.

The *in vivo* rabbit model used for PDR and DME exhibited retinal neovascularization and vascular leakage indicative of pathologic vessel growth associated with these diseases. The Müller cell toxin DL-a-aminoadipic acid (DL-AAA) was injected intravitreally and has been shown to induce the pathology of the model in the first 2 weeks [45-47] which was supported by the present findings (**Figure 2.6A, Figure 2.7**). Müller glial cells are specific to the retina and are responsible for protecting neurons, maintaining homeostasis and neuronal metabolic support [48]. They have been shown to undergo gliosis in PDR and in doing so contribute to the progression of the disease by the release of angiogenic cytokines such as VEGF [48, 49]. VEGF in turn promotes neovascular growth and induces vascular leakage [2, 3]. A single injection of DL-AAA exhibited a retinal neovascular pathology in rabbits from 2 to 65 weeks post injection [45, 46]. Prior studies with this model have shown that injection of the anti-VEGF drug aflibercept (Eylea[(c)], 0.5mg dose) was able to temporarily stop vascular leakage for 8 weeks, after which time recurrence of vascular leakage was observed [45, 46]. Those results demonstrated both the association of VEGF-A with vascular leakage and the stability of the pathology. Our data exhibited a comparable performance resulting in an inhibition of leakage up to 12 weeks (**Figure 2.6D**). These data correlated well with postmortem VEGF-A vitreous ELISA analyses

demonstrating a significant reduction in VEGF-A at both 1, 4 and 12 weeks after F-pSiNP treatment relative to untreated DL-AAA animals at the same timepoints (**Figure 2.6E**) and resulted in an 8.4-fold decrease in VEGF-A for the treated animals over sham control animals at 12 weeks, (p = 0.0262, n = 4 each).

It should be noted that the disease model, involving a dose of 80 µL of 80 mM DL-AAA, resulted in substantial incidences of retinal detachment (>50%) in the animals, a sign of severe disease that eliminates the utility of FA imaging. This incidence was substantially higher than the previously reported percentage of animals (20%) that experienced these adverse events [45]. The VEGF-A molecular analysis was performed using these animals with severe disease (*i.e.*, those with retinal detachments); thus, it is likely that the levels of VEGF-A reported in this work are an upper estimate, and VEGF-A expression in the animals used to quantify leakage (FA imaging) were likely lower. Animal welfare concerns precluded running of non-targeting controls on this model. Future work will include evaluating the model at lower doses of DL-AAA in order to minimize adverse retinal detachment events. While the present work showed that iRGD-targeted F-pSiNPs are highly effective at suppressing vascular leakage, establishing the overall feasibility of the approach, the questions of whether or not the iRGD targeting group is essential, and which cells can (or should) be targeted were not addressed.

This study was a first attempt at utilizing iRGD technology for the delivery of nanoparticles to retinal neovascular cells. The study established the feasibility of using a combination of a solid, but resorbable nanoparticle with cellular targeting and penetration innovations to overcome prior limitations of nucleic acid therapeutics for knocking down VEGF

expression. The positive results on arresting neovascularization and reducing vascular leakage in the rabbit model over a 3-month period indicates that this is a promising approach to treat debilitating eye diseases such as macular degeneration, proliferative diabetic retinopathy, or diabetic macular edema.

Acknowledgements

Chapter 2 is currently being prepared for submission for publication of the material. Grondek, J.F., Luo, C., Hu, D., Christman, K.L., Ruoslahti, E., and Sailor, M.J., Targeted Iron Oxide Nanoworms for Contrast Enhanced Magnetic Resonance Molecular Imaging of Fibrin Networks within Infarcted Myocardium. The dissertation author was the primary researcher and author of this material.

2.6 References

1. Lee, R., T.Y. Wong, and C. Sabanayagam, *Epidemiology of diabetic retinopathy, diabetic macular edema and related vision loss.* Eye Vis (Lond), 2015. **2**: p. 17.

2. Cai, J. and M. Boulton, *The pathogenesis of diabetic retinopathy: old concepts and new questions.* Eye (Lond), 2002. **16**(3): p. 242-60.

3. Campochiaro, P.A., *Ocular neovascularization.* J Mol Med (Berl), 2013. **91**(3): p. 311-21.

4. Rosenfeld, P.J., M.A. Windsor, W.J. Feuer, S.J.J. Sun, K.D. Frick, E.A. Swanson, and D. Huang, *Estimating Medicare and Patient Savings From the Use of Bevacizumab for the Treatment of Exudative Age-related Macular Degeneration.* Am J Ophthalmol, 2018. **191**: p. 135-139.

5. Writing Committee for the Diabetic Retinopathy Clinical Research, N., J.G. Gross, A.R. Glassman, L.M. Jampol, S. Inusah, L.P. Aiello, A.N. Antoszyk, C.W. Baker, B.B. Berger, N.M. Bressler, D. Browning, M.J. Elman, F.L. Ferris, 3rd, S.M. Friedman, D.M. Marcus, M. Melia, C.R. Stockdale, J.K. Sun, and R.W. Beck, *Panretinal Photocoagulation vs Intravitreous Ranibizumab for Proliferative Diabetic Retinopathy: A Randomized Clinical Trial.* JAMA, 2015. **314**(20): p. 2137-2146.

6. Mitchell, P., F. Bandello, U. Schmidt-Erfurth, G.E. Lang, P. Massin, R.O. Schlingemann, F. Sutter, C. Simader, G. Burian, O. Gerstner, A. Weichselberger, and R.s. group, *The RESTORE study: ranibizumab monotherapy or combined with laser versus laser monotherapy for diabetic macular edema.* Ophthalmology, 2011. **118**(4): p. 615-25.

7. Mitchell, P., P. Massin, S. Bressler, C.D. Coon, J. Petrillo, A. Ferreira, and N.M. Bressler, *Three-year patient-reported visual function outcomes in diabetic macular edema managed with ranibizumab: the RESTORE extension study.* Current Medical Research and Opinion, 2015. **31**(11): p. 1967-1975.

8. Heier, J.S., J.F. Korobelnik, D.M. Brown, U. Schmidt-Erfurth, D.V. Do, E. Midena, D.S. Boyer, H. Terasaki, P.K. Kaiser, D.M. Marcus, Q.D. Nguyen, G.J. Jaffe, J.S. Slakter, C. Simader, Y. Soo, T. Schmelter, R. Vitti, A.J. Berliner, O. Zeitz, C. Metzig, and F.G. Holz, *Intravitreal Aflibercept for Diabetic Macular Edema: 148-Week Results from the VISTA and VIVID Studies.* Ophthalmology, 2016. **123**(11): p. 2376-2385.

9. Heng, L.Z., O. Comyn, T. Peto, C. Tadros, E. Ng, S. Sivaprasad, and P.G. Hykin, *Diabetic retinopathy: pathogenesis, clinical grading, management and future developments.* Diabet Med, 2013. **30**(6): p. 640-50.

10. Singer, M.A., C.C. Awh, S. Sadda, W.R. Freeman, A.N. Antoszyk, P. Wong, and L. Tuomi, *HORIZON: an open-label extension trial of ranibizumab for choroidal neovascularization secondary to age-related macular degeneration.* Ophthalmology, 2012. **119**(6): p. 1175-83.

11. Rofagha, S., R.B. Bhisitkul, D.S. Boyer, S.R. Sadda, K. Zhang, and S.-U.S. Group, *Seven-year outcomes in ranibizumab-treated patients in ANCHOR, MARINA, and HORIZON: a multicenter cohort study (SEVEN-UP).* Ophthalmology, 2013. **120**(11): p. 2292-9.

12. Falavarjani, K.G. and Q.D. Nguyen, *Adverse events and complications associated with intravitreal injection of anti-VEGF agents: a review of literature.* Eye (Lond), 2013. **27**(7): p. 787-94.

13. Grunwald, J.E., M. Pistilli, E. Daniel, G.S. Ying, W. Pan, G.J. Jaffe, C.A. Toth, S.A. Hagstrom, M.G. Maguire, D.F. Martin, and G. Comparison of Age-Related Macular Degeneration Treatments Trials Research, *Incidence and Growth of Geographic Atrophy during 5 Years of Comparison of Age-Related Macular Degeneration Treatments Trials.* Ophthalmology, 2017. **124**(1): p. 97-104.

14. Semeraro, F., F. Morescalchi, F. Parmeggiani, B. Arcidiacono, and C. Costagliola, *Systemic adverse drug reactions secondary to anti-VEGF intravitreal injection in patients with neovascular age-related macular degeneration.* Curr Vasc Pharmacol, 2011. **9**(5): p. 629-46.

15. Bressler, N.M., W.T. Beaulieu, M.G. Maguire, A.R. Glassman, K.J. Blinder, S.B. Bressler, V.H. Gonzalez, L.M. Jampol, M. Melia, J.K. Sun, J.A. Wells, 3rd, and N. Diabetic Retinopathy Clinical Research, *Early Response to Anti-Vascular Endothelial Growth Factor and Two-Year Outcomes Among Eyes With Diabetic Macular Edema in Protocol T.* Am J Ophthalmol, 2018. **195**: p. 93-100.

16. Zhao, Y. and R.P. Singh, *The role of anti-vascular endothelial growth factor (anti-VEGF) in the management of proliferative diabetic retinopathy.* Drugs Context, 2018. **7**: p. 212532.

17. Ozcan, G., B. Ozpolat, R.L. Coleman, A.K. Sood, and G. Lopez-Berestein, *Preclinical and clinical development of siRNA-based therapeutics.* Adv Drug Deliv Rev, 2015. **87**: p. 108-19.

18. COBALT, *Safety & Efficacy Study Evaluating the Combination of Bevasiranib & Lucentis Therapy in Wet AMD; The purpose of this study is to compare the safety and effectiveness of bevasiranib given either every 8 weeks or every 12 weeks after an initial pre-treatment with 3 injections of Lucentis® (ranibizumab injection) compared to Lucentis® given every 4 weeks to people with wet AMD. Patients will be assigned at random (like tossing a coin) to receive one of three treatments options for 104 weeks; NCT00499590.* www.clinicaltrials.gov, 2014.

19. Kleinman, M.E., K. Yamada, A. Takeda, V. Chandrasekaran, M. Nozaki, J.Z. Baffi, R.J. Albuquerque, S. Yamasaki, M. Itaya, Y. Pan, B. Appukuttan, D. Gibbs, Z. Yang, K. Kariko, B.K. Ambati, T.A. Wilgus, L.A. DiPietro, E. Sakurai, K. Zhang, J.R. Smith, E.W. Taylor, and J. Ambati, *Sequence- and target-independent angiogenesis suppression by siRNA via TLR3.* Nature, 2008. **452**(7187): p. 591-7.

20. Kleinman, M.E., H. Kaneko, W.G. Cho, S. Dridi, B.J. Fowler, A.D. Blandford, R.J. Albuquerque, Y. Hirano, H. Terasaki, M. Kondo, T. Fujita, B.K. Ambati, V. Tarallo, B.D. Gelfand, S. Bogdanovich, J.Z. Baffi, and J. Ambati, *Short-interfering RNAs induce retinal degeneration via TLR3 and IRF3.* Mol Ther, 2012. **20**(1): p. 101-8.

21. Foster, D.J., C.R. Brown, S. Shaikh, C. Trapp, M.K. Schlegel, K. Qian, A. Sehgal, K.G. Rajeev, V. Jadhav, M. Manoharan, S. Kuchimanchi, M.A. Maier, and S. Milstein, *Advanced siRNA Designs Further Improve In Vivo Performance of GalNAc-siRNA Conjugates.* Mol Ther, 2018. **26**(3): p. 708-717.

22. Hu, B., L. Zhong, Y. Weng, L. Peng, Y. Huang, Y. Zhao, and X.J. Liang, *Therapeutic siRNA: state of the art.* Signal Transduct Target Ther, 2020. **5**(1): p. 101.

23. Nieto, A., H. Hou, S.W. Moon, M.J. Sailor, W.R. Freeman, and L. Cheng, *Surface Engineering of Porous Silicon Microparticles for Intravitreal Sustained Delivery of Rapamycin.* Invest. Ophthalmol. Vis. Sci., 2015. **56**(2): p. 1070-1080.

24. Nieto, A., H. Hou, M.J. Sailor, W.R. Freeman, and L. Cheng, *Ocular silicon distribution and clearance following intravitreal injection of porous silicon microparticles.* Exp. Eye Res., 2013. **116**: p. 161-168.

25. Hartmann, K.I., A. Nieto, E.C. Wu, W.R. Freeman, J.S. Kim, J. Chhablani, M.J. Sailor, and L.Y. Cheng, *Hydrosilylated Porous Silicon Particles Function as an Intravitreal Drug Delivery System for Daunorubicin.* J. Ocul. Pharmacol. Ther., 2013. **29**(5): p. 493-500.

26. Kashanian, S., F. Harding, Y. Irani, S. Klebe, K. Marshall, A. Loni, L. Canham, D.M. Fan, K.A. Williams, N.H. Voelcker, and J.L. Coffer, *Evaluation of mesoporous silicon/polycaprolactone composites as ophthalmic implants.* Acta Biomater., 2010. **6**(9): p. 3566-3572.

27. Low, S.P., N.H. Voelcker, L.T. Canham, and K.A. Williams, *The biocompatibility of porous silicon in tissues of the eye.* Biomaterials, 2009. **30**(15): p. 2873-80.

28. Joo, J., E.J. Kwon, J. Kang, M. Skalak, E.J. Anglin, A.P. Mann, E. Ruoslahti, S. Bhatia, and M.J. Sailor, *Porous Silicon-Graphene Oxide Core-Shell Nanoparticles for Targeted Delivery of siRNA to the Injured Brain.* Nanoscale Horiz., 2016. **1**: p. 407-414.

29. Baran-Rachwalska, P., N. Torabi-Pour, F.M. Sutera, M. Ahmed, K. Thomas, M.A. Nesbit, M. Welsh, C.B.T. Moore, and S.R. Saffie-Siebert, *Topical siRNA delivery to the cornea and anterior eye by hybrid silicon-lipid nanoparticles.* J. Control Release, 2020. **326**: p. 192-202.

30. Tong, W.Y., M. Alnakhli, R. Bhardwaj, S. Apostolou, S. Sinha, C. Fraser, T. Kuchel, B. Kuss, and N.H. Voelcker, *Delivery of siRNA in vitro and in vivo using PEI-capped porous silicon nanoparticles to silence MRP1 and inhibit proliferation in glioblastoma.* J. Nanobiotechnol., 2018. **16**.

31. Kafshgari, M.H., M. Alnakhli, B. Delalat, S. Apostolou, F.J. Harding, E. Makila, J.J. Salonen, B.J. Kuss, and N.H. Voelcker, *Small interfering RNA delivery by polyethylenimine-functionalised porous silicon nanoparticles.* Biomater. Sci., 2015. **3**(12): p. 1555-1565.

32. Zhang, M.Z., R. Xu, X.J. Xia, Y. Yang, J.H. Gu, G.T. Qin, X.W. Liu, M. Ferrari, and H.F. Shen, *Polycation-functionalized nanoporous silicon particles for gene silencing on breast cancer cells.* Biomaterials, 2014. **35**(1): p. 423-431.

33. Wan, Y., S. Apostolou, R. Dronov, B. Kuss, and N.H. Voelcker, *Cancer-targeting siRNA delivery from porous silicon nanoparticles.* Nanomedicine, 2014. **9**(15): p. 2309-2321.

34. Kang, J., J. Joo, E.J. Kwon, M. Skalak, S. Hussain, Z.G. She, E. Ruoslahti, S.N. Bhatia, and M.J. Sailor, *Self-Sealing Porous Silicon-Calcium Silicate Core-Shell Nanoparticles for Targeted siRNA Delivery to the Injured Brain.* Adv Mater, 2016. **28**(36): p. 7962-7969.

35. Kim, B., H.B. Pang, J. Kang, J.H. Park, E. Ruoslahti, and M.J. Sailor, *Immunogene therapy with fusogenic nanoparticles modulates macrophage response to Staphylococcus aureus.* Nat Commun, 2018. **9**(1): p. 1969.

36. Baran-Rachwalska, P., N. Torabi-Pour, F.M. Sutera, M. Ahmed, K. Thomas, M.A. Nesbit, M. Welsh, C.B.T. Moore, and S.R. Saffie-Siebert, *Topical siRNA delivery to the cornea and anterior eye by hybrid silicon-lipid nanoparticles.* Journal of Controlled Release, 2020. **326**: p. 192-202.

37. Kim, B., S. Sun, J.A. Varner, S.B. Howell, E. Ruoslahti, and M.J. Sailor, *Securing the Payload, Finding the Cell, and Avoiding the Endosome: Peptide-Targeted, Fusogenic Porous Silicon Nanoparticles for Delivery of siRNA.* Adv Mater, 2019. **31**(35): p. e1902952.

38. Torchilin, V.P., *Recent advances with liposomes as pharmaceutical carriers.* Nat Rev Drug Discov, 2005. **4**(2): p. 145-60.

39. Teesalu, T., K.N. Sugahara, and E. Ruoslahti, *Tumor-penetrating peptides.* Front Oncol, 2013. **3**: p. 216.

40. Ruoslahti, E., *Peptides as targeting elements and tissue penetration devices for nanoparticles.* Adv Mater, 2012. **24**(28): p. 3747-56.

41. Ruoslahti, E., *Tumor penetrating peptides for improved drug delivery.* Adv Drug Deliv Rev, 2017. **110-111**: p. 3-12.

42. Sugahara, K.N., T. Teesalu, P.P. Karmali, V.R. Kotamraju, L. Agemy, O.M. Girard, D. Hanahan, R.F. Mattrey, and E. Ruoslahti, *Tissue-penetrating delivery of compounds and nanoparticles into tumors.* Cancer Cell, 2009. **16**(6): p. 510-20.

43. Friedlander, M., C.L. Theesfeld, M. Sugita, M. Fruttiger, M.A. Thomas, S. Chang, and D.A. Cheresh, *Involvement of integrins alpha v beta 3 and alpha v beta 5 in ocular neovascular diseases.* Proc Natl Acad Sci U S A, 1996. **93**(18): p. 9764-9.

44. Fernandez-Robredo, P., S. Selvam, M.B. Powner, D.A. Sim, and M. Fruttiger, *Neuropilin 1 Involvement in Choroidal and Retinal Neovascularisation.* PLoS One, 2017. **12**(1): p. e0169865.

45. Cao, J., T.C. MacPherson, B.V. Iglesias, Y. Liu, N. Tirko, G.D. Yancopoulos, S.J. Wiegand, and C. Romano, *Aflibercept Action in a Rabbit Model of Chronic Retinal Neovascularization: Reversible Inhibition of Pathologic Leakage With Dose-Dependent Duration.* Invest Ophthalmol Vis Sci, 2018. **59**(2): p. 1033-1044.

46. Li, Y., J.M. Busoy, B.A.A. Zaman, Q.S.W. Tan, G.S.W. Tan, V.A. Barathi, N. Cheung, J.J. Wei, W. Hunziker, W. Hong, T.Y. Wong, and C.M.G. Cheung, *A novel model of persistent retinal neovascularization for the development of sustained anti-VEGF therapies.* Exp Eye Res, 2018. **174**: p. 98-106.

47. Shen, W., S. Li, S.H. Chung, and M.C. Gillies, *Retinal vascular changes after glial disruption in rats.* J Neurosci Res, 2010. **88**(7): p. 1485-99.

48. Bringmann, A. and P. Wiedemann, *Muller Glial Cells in Retinal Disease.* Ophthalmologica, 2012. **227**(1): p. 1-19.

49. Fletcher, E.L., J.A. Phipps, M.M. Ward, T. Puthussery, and J.L. Wilkinson-Berka, *Neuronal and glial cell abnormality as predictors of progression of diabetic retinopathy.* Current Pharmaceutical Design, 2007. **13**(26): p. 2699-2712.

50. Fu, Y.C. and Z.M. Xin, *Inhibited corneal neovascularization in rabbits following corneal alkali burn by double-target interference for VEGF and HIF-1alpha.* Biosci Rep, 2019. **39**(1).

51. Wu, D. and P. Yotnda, *Induction and testing of hypoxia in cell culture.* J Vis Exp, 2011(54).

52. Schneider, C.A., W.S. Rasband, and K.W. Eliceiri, *NIH Image to ImageJ: 25 years of image analysis.* Nature Methods, 2012. **9**(7): p. 671-675.

53. Sailor, M.J. and E.C. Wu, *Photoluminescence-Based Sensing With Porous Silicon Films, Microparticles, and Nanoparticles.* Advanced Functional Materials, 2009. **19**(20): p. 3195-3208.

54. Qin, Z.T., J. Joo, L. Gu, and M.J. Sailor, *Size Control of Porous Silicon Nanoparticles by Electrochemical Perforation Etching.* Particle & Particle Systems Characterization, 2014. **31**(2): p. 252-256.

55. Bantseev, V., P.E. Miller, E. Bentley, C. Schuetz, T.M. Streit, B.J. Christian, C. Farman, H. Booler, and E.A. Thackaberry, *Determination of a No-Observable Effect Level for Endotoxin Following a Single Intravitreal Administration to Dutch Belted Rabbits.* Invest Ophthalmol Vis Sci, 2017. **58**(3): p. 1545-1552.

56. Garba, A.O. and S.A. Mousa, *Bevasiranib for the treatment of wet, age-related macular degeneration.* Ophthalmol Eye Dis, 2010. **2**: p. 75-83.

57. Huang, X.N. and Y. Chau, *Investigating impacts of surface charge on intraocular distribution of intravitreal lipid nanoparticles.* Experimental Eye Research, 2019. **186**.

58. Liu, H.A., Y.L. Liu, Z.Z. Ma, J.C. Wang, and Q. Zhang, *A lipid nanoparticle system improves siRNA efficacy in RPE cells and a laser-induced murine CNV model.* Invest Ophthalmol Vis Sci, 2011. **52**(7): p. 4789-94.

59. Lee, J., N.K. Ryoo, H. Han, H.K. Hong, J.Y. Park, S.J. Park, Y.K. Kim, C. Sim, K. Kim, S.J. Woo, K.H. Park, and H. Kim, *Anti-VEGF PolysiRNA Polyplex for the Treatment of Choroidal Neovascularization.* Mol Pharm, 2016. **13**(6): p. 1988-95.

60. Liu, J., L. Luo, F. Xu, G. Li, J. Chen, L. Teng, Y. Li, and F. Sun, *Cyclic RGD Peptide Targeting Coated Nano Drug Co-Delivery System for Therapeutic Use in Age-Related Macular Degeneration Disease.* Molecules, 2020. **25**(21).

61. Wang, J.L., Y.L. Liu, Y. Li, W.B. Dai, Z.M. Guo, Z.H. Wang, and Q. Zhang, *EphA2 Targeted Doxorubicin Stealth Liposomes as a Therapy System for Choroidal Neovascularization in Rats.* Investigative Ophthalmology & Visual Science, 2012. **53**(11): p. 7348-7357.

62. Vasconcelos, A., E. Vega, Y. Pérez, M.J. Gómara, M.L. García, and I. Haro, *Conjugation of cell-penetrating peptides with poly(lactic-co-glycolic acid)-polyethylene glycol nanoparticles improves ocular drug delivery.* Int J Nanomedicine, 2015. **10**: p. 609-31.

63. Chu, Y., N. Chen, H. Yu, H. Mu, B. He, H. Hua, A. Wang, and K. Sun, *Topical ocular delivery to laser-induced choroidal neovascularization by dual internalizing RGD and TAT peptide-modified nanoparticles.* Int J Nanomedicine, 2017. **12**: p. 1353-1368.

64. Ehrlich, R.C., T. A, *siRNA: Set for a Comeback?* Retinal Physician, 2010.

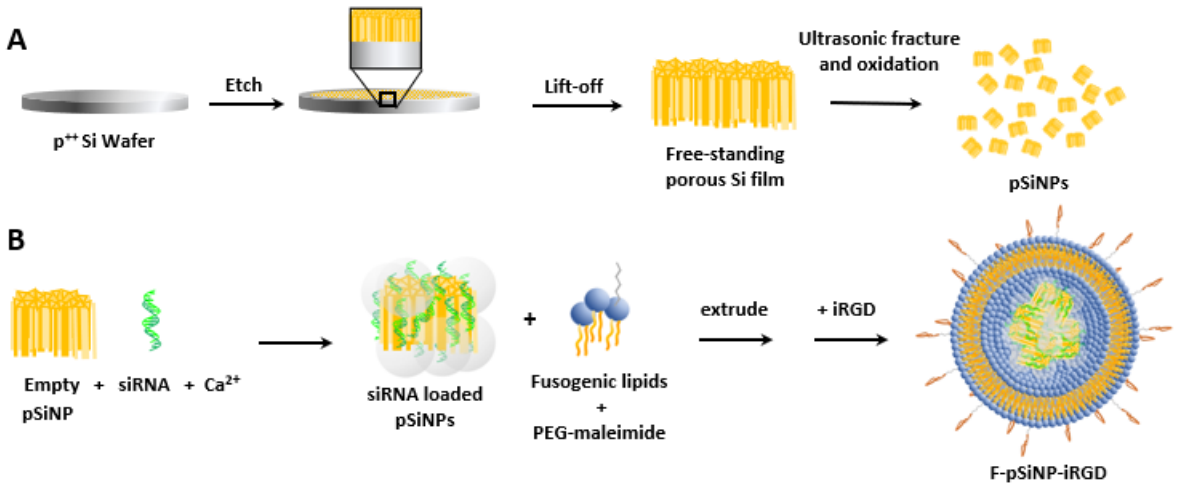

Figure 2.1. Schematic representation of the synthesis of the fusogenic porous silicon nanoparticles (F-pSiNPs) used in this work. **A.** Electrochemical anodization of a silicon wafer selectively etches silicon to generate a nanostructured mesoporous layer which is removed and subjected to ultrasonic fracture to produce the porous silicon nanoparticles (pSiNPs). **B.** The empty pSiNPs are loaded with an siRNA payload by means of a calcium ion-induced condensation reaction. The resulting siRNA-loaded pSiNPs are added to a fusogenic lipid mixture that also contains a PEG-2000 maleimide linker ("fusogenic lipids + PEG-maleimide"). Extrusion coats the solid pSiNP core with a fusogenic lipid layer. The iRGD targeting peptide (or a control peptide) is then grafted to the PEG-2000 linker *via* the pendant maleimide, generating the final ~200nm nanoparticle construct ("F-pSiNP-iRGD").

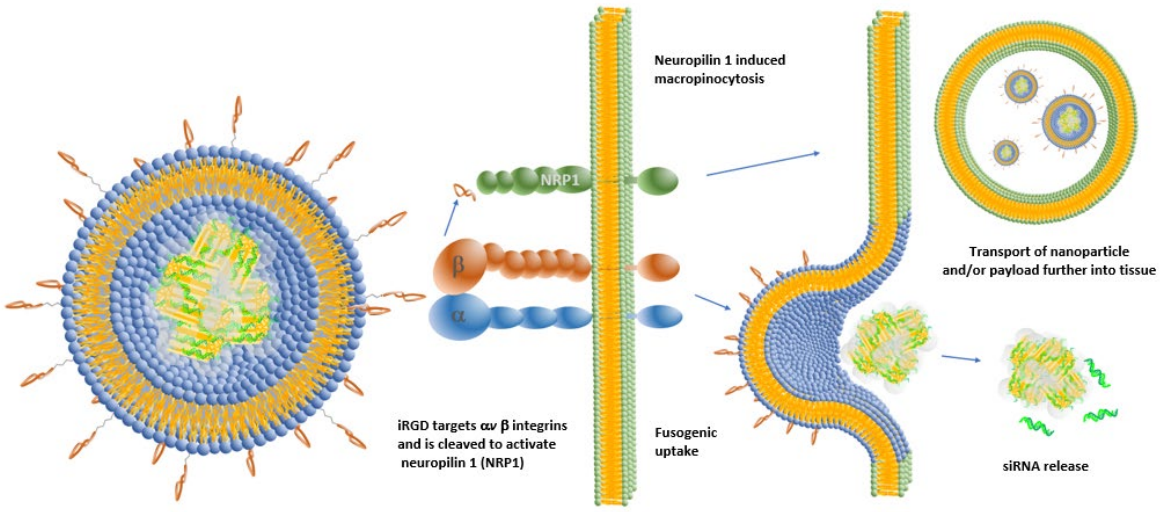

Figure 2.2. Schematic of the structure of iRGD-labeled, fusogenic porous silicon nanoparticles and proposed mechanisms for their cellular uptake. The iRGD targeting peptide is known to target αvβ integrins at the cell surface. Once bound to the cell surface, the nanoparticle can either be directly inserted into the cytosol by fusogenic uptake, or it can be taken up by macropinocytosis after enzymatic cleavage of the peptide, which activates a neuropilin uptake pathway.

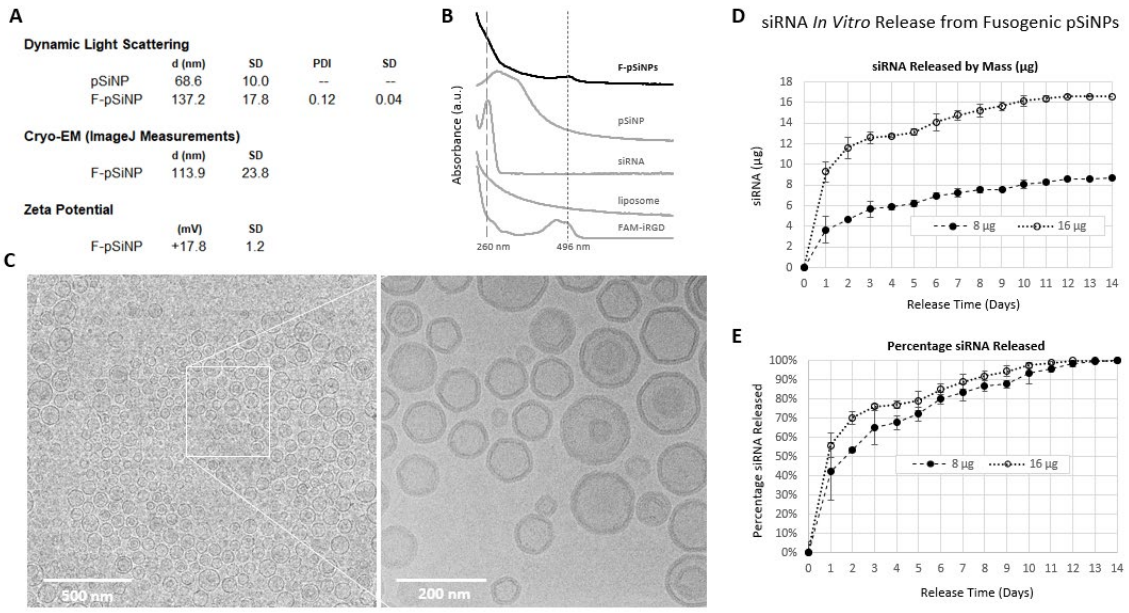

Figure 2.3. Characterization of fusogenic porous silicon nanoparticles (F-pSiNPs). **A**. Dynamic light scattering and ImageJ measurements from Cryogenic electron microscopy (Cryo-EM), and zeta potentials for F-pSiNPs. **B**. Absorbance spectra of F-pSiNPs and the synthesis components. **C**. Cryo-EM images, scale bar = 500 nm and 200 nm, at 10k and 33k magnification, respectively. **D-E**. *In vitro* release study of F-pSiNPs in PBS buffer (pH 7.4) at 37 °C under constant agitation. **D**. Temporal siRNA release curve, measured by absorbance, from two FNP samples at 1x and 2x the concentration that was used for *in vivo* injections. **E**. Same data from D, but converted to percentage of siRNA released from each F-pSiNP formulation as a function of time.

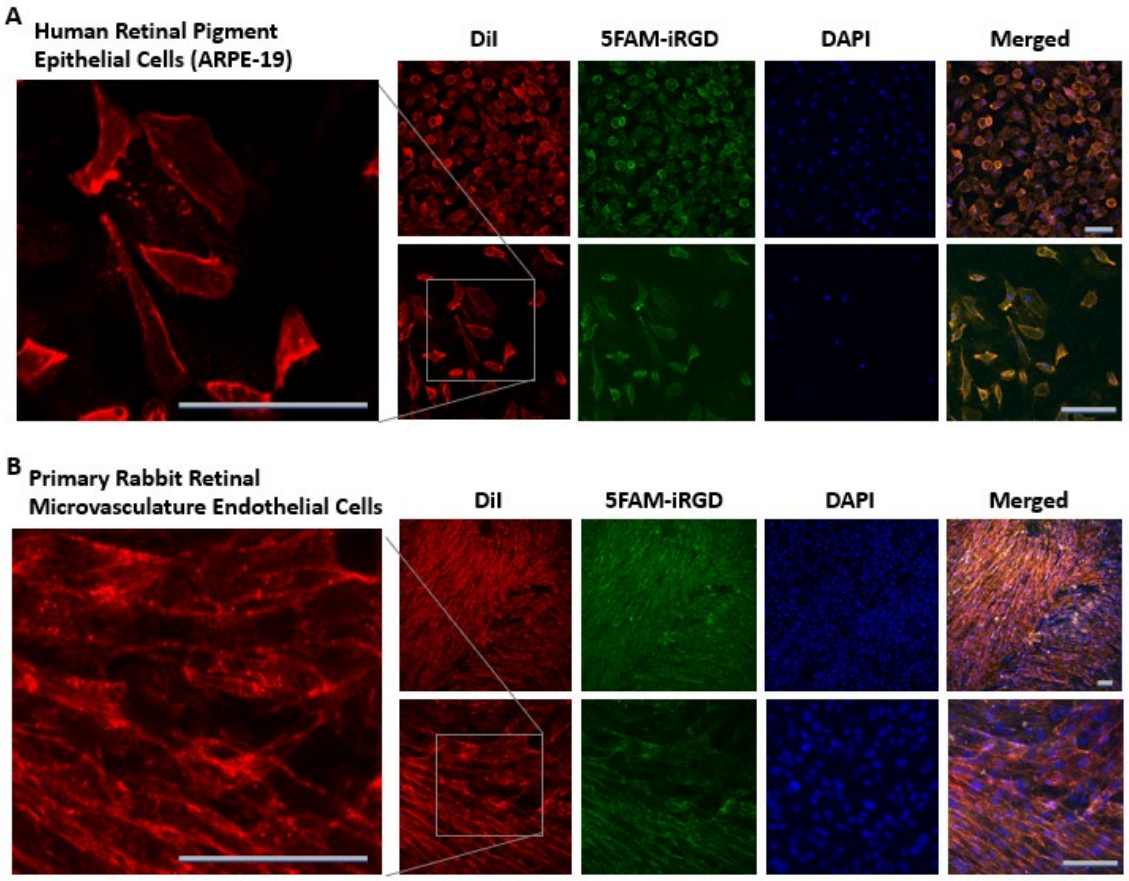

Figure 2.4. Confocal images of cells treated with iRGD-targeted fusogenic porous silicon nanoparticles *in vitro*, demonstrating the fusogenic nature of the construct: **A**. human retinal pigment epithelial cells (ARPE-19) and **B**. primary rabbit retinal microvasculature endothelial cells. The lipophilic fluorophore DiI (red) was incorporated into the fusogenic lipid coating, 5FAM (green) was covalently attached to the iRGD targeting peptide. DAPI (blue) was used to stain the cell nuclei. All particles were incubated with cells at confluency for 20 min at 37 °C followed by wash, 4% PFA and DAPI staining, Image **A**. is 20X magnification, with 40X with exploded views and **B**. is 10X, with 40X exploded views. The scale bars represent 100 µm.

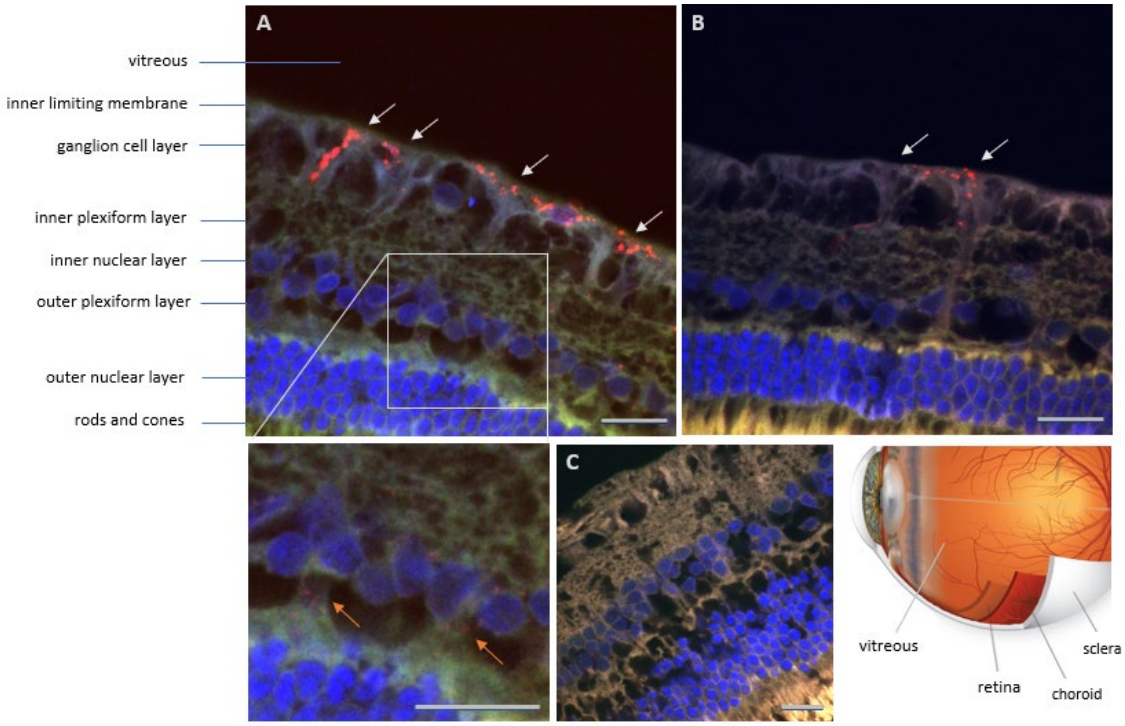

Figure 2.5. Confocal microscope images of rabbit eye histology sections 72 hr post-treatment with iRGD-targeted fusogenic porous silicon nanoparticles. **A-B**. F-pSiNPs loaded with the lipophilic fluorophore DiI (red), stained with DAPI nuclear stain (blue) and tissue autofluorescence (green) and **C**. sham treatment. The white arrows indicate particles taken up by Müller cells. The orange arrows indicate particles transported to the outer nuclear layer, scale bars = 20 µm. Lower right image shows a representation of the eye indicating the retinal layer.

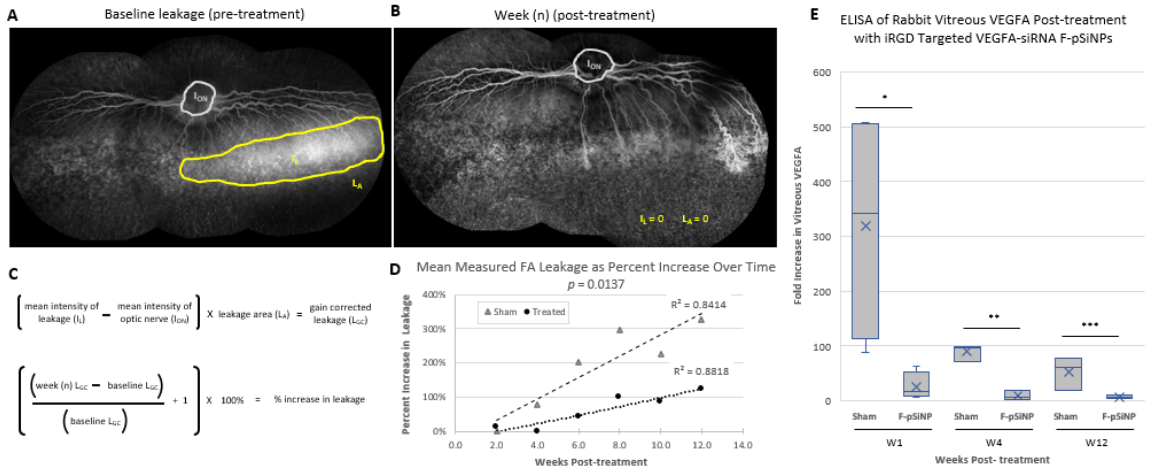

Figure 2.6. Mid-phase fluorescein angiography (FA) data for rabbit eyes injected with DL-α aminoadipic acid and treated with fusogenic porous silicon nanoparticles (F-pSiNPs) or sham treatment. **A**. Representative image of montaged FA leakage at two weeks post-disease induction (baseline) and **B**. (n) weeks post-treatment. Leakage area (LA) circled in yellow, intensity of leakage (IL) within the circle, and intensity of optic nerve (ION) within the grey circle. **C**. Mathematical relationships used to quantify leakage from FA images and analyzed with ImageJ for the regions of interest as shown in **A** and **B**, adjusted for gain using the region of the optic nerve within each montage, resulting in gain corrected leakage (LGC). **D**. Plot of the increase in the mean percent of corrected leakage from baseline *vs*. weeks post-treatment showing F-pSiNP-treated animals (circles) and sham BSS-treated animals (triangles), n = 5 treated and n = 4 sham, p = 0.0137 by repeated measurements. **E**. Postmortem ELISA of rabbit VEGF-A from vitreous from sham- or F-pSiNP-treated animals, sacrificed at each time point of 1-, 4- and 12-weeks post-treatment, * p = 0.0348, ** p = 0.0014, and *** p = 0.0262, n = 3 or 4 ea.

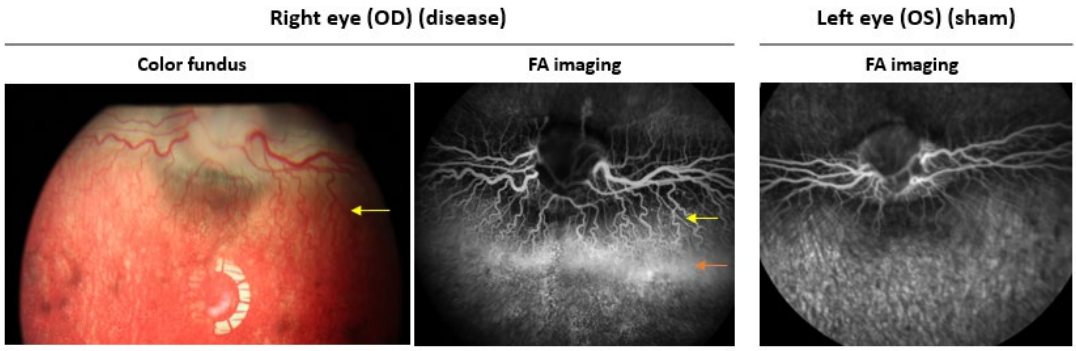

Figure 2.7. Color fundus and fluorescein angiography (FA) images of DL-AAA-injected right eye (OS) and FA image of balanced salt solution (BSS)-injected left eye (OS). Images taken at 2 weeks after disease induction, prior to fusogenic porous silicon nanoparticle treatment. The yellow arrows indicate the region of tortuous vessel development, and the orange arrow indicates leakage, relative to the OS control on the far right.

Chapter 3

Targeted Iron Oxide Nanoworms for Contrast-Enhanced Magnetic Resonance Molecular Imaging of Fibrin Networks within Infarcted Myocardium

3.1 Abstract

The emergence of targeted nanoparticles applied to contrast-enhanced magnetic resonance imaging (CE-MRI) affords a unique platform combining the safety associated with MRI with the logical design of diagnostic tools for *in vivo* imaging at the molecular level. We demonstrate long-circulating superparamagnetic iron oxide nanoworms (NWs) conjugated to the pentapeptide CREKA can target fibrin associated with an acute myocardial infarction for use as a T2-weighted cardiac magnetic resonance imaging (CMRI) contrast agent. We show that co-administration of this actively targeted CREKA-NW T2 agent with a passively targeted T1 agent (gadolinium-diethylenetriaminepentaacetic acid) can be used to highlight the region of fibrin relative to the total infarct in a rat myocardial infarction model.

3.2 Introduction

Myocardial infarction (MI) affects approximately a million people annually in the US [1]. Occlusion of the coronary arteries leads to hypoxia, nutrient depravation, and then reperfusion-induced oxidative stress upon revascularization therapies such as angioplasty [2]. The physiopathology of MI can be divided into three temporal stages: *Inflammation,* which occurs the at the onset of occlusion, induces cellular necrosis and low levels of apoptosis, and promotes fibrin-platelet clot formation; *proliferation,* which begins after approximately three days and is indicated by neovascularization in response to hypoxia, and fibroblast and myofibroblast remodeling of the extracellular matrix; and the final stage of *maturation*, which

appears at roughly seven days post-infarction where fibroblasts begin to dissipate and a collagen scar begins to form [2]. Myocardium constitutively express tissue factor, the protein mediator of the extrinsic clotting cascade, which results in fibrin deposition in infarcted myocardium [3]. These deposits begin to occur at the onset of ischemia (inflammation stage) and have been linked to late-stage scar formation [3].

Contrast enhanced cardiovascular magnetic resonance imaging (CE-CMRI) is an important emerging technique for imaging MI because it provides images of high spatial resolution in a relatively short period of time, with low risk to patient safety [4, 5]. Magnetic resonance contrast agents generally come in two classes: T1-weighted, longitudinal (or spin-lattice) agents, which result in bright signals and predominantly consist of gadolinium chelates; and T2-weighted, transverse (or spin-spin), contrast agents which result in dark signals and are usually composed of superparamagnetic iron oxide nanoparticles (SPIONs). Delayed enhancement CMRI (DE-CMRI), also called late gadolinium enhancement, is a method for cardiac perfusion imaging that is effective at discerning regions of infarcted myocardium from healthy tissue because the agent is preferentially retained in the infarcted tissues (9). Among the recent advances in synthesis methods for SPIONs [6-10], one formulation resulted in a filamentous chain of SPIONs dubbed nanoworms (NWs) [11]. NWs have been shown to elevate the T2 relaxation rate equating to a higher degree of MR contrast sensitivity, with an increased circulation half-life, lower immunogenicity, and a greater degree of targeted cellular uptake when compared to SPION spheres [11-14].

Myocardial infarction (MI) and cardiac remodeling have been the focus of several studies utilizing targeted CE-CMRI imaging agents in murine models of ischemia reperfusion [15-19]. In the present study, we focused on the pentapeptide CREKA (Cys-Arg-Glu-Lys-Ala) as the selective targeting agent. CREKA binds to fibrin, and while CREKA is better known as a tumor-targeting peptide [13, 20-22], the formation of fibrin networks upon acute cardiac tissue damage suggests CREKA could also be used to image fibrin formation induced by ischemic damage. Nanoparticles with pendant CREKA peptides have been used to target fibrin linked to atherosclerosis [23-28] and thrombosis [25, 29, 30] and CREKA has been used to target drug-containing nanoparticles [31] and stem cells to infarcted myocardium [32]. Of most relevance to the present study, CREKA has been conjugated to SPIONS for selective imaging of microthrombus formation within the myocardial vasculature 24 h after ischemia reperfusion surgery [29]. While this latter study demonstrated the ability of CREKA-SPIONs to bind to fibrin in circulating microthrombi in the vasculature, some questions remain. In particular, the specificity of binding relative to scrambled peptide controls, and whether or not the peptide-targeted nanoparticles can detect fibrin formation within the infarct, outside of the vasculature, are not known [29]. However, to date, no studies have validated the use of CREKA to image fibrin in the infarct area, and furthermore, no studies have conjugated CREKA to the nanoworm formulation of iron oxide nanoparticles, which would allow attachment of multiple copies of the targeting peptide to introduce multivalent interactions, which has been shown to increase the effective affinity of the CREKA-nanoparticle assembly for the target tissues [11]. The focus of this work was to develop a long circulating, targeted MI contrast agent to image the biological changes occurring in infarction, using fibrin networks as a proof of concept. We aimed to evaluate the potential of

using both a Gd-based, passively targeted T1 agent in concert with the actively targeted CREKA-NW T2 agent in order to capitalize on the benefits of both MR imaging modalities. As a noninvasive method to image fibrin deposition relative to the total infarcted myocardium, this approach has the potential to continuously monitor fibrin over the course of infarct remodeling while at the same time providing a comprehensive picture of the infarction. We show a statistically significant targeting of CREKA-NWs to infarct myocardium relative to a nontargeting control peptide KAKEC-NWs, and we demonstrate the co-administration of CREKA-NWs and Gd-DTPA for targeted T2 and passive T1 MR imaging of fibrin relative to the total area of infarction.

3.3 Methods

Materials: Ferric chloride hexahydrate >99% pure (Sigma), ferrous chloride tetrahydrate >99% pure (Sigma), dextran T20 (Pharmacosmos), sodium hydroxide (Sigma), epichlorohydrin (Sigma), ammonium hydroxide (Sigma), Cyanine 7 N-succinimidyl ester (Cy7-NHS) (Lumiprobe), 5k MW N-succinimidyl ester-polyethylene glycol-maleimide (NHS-PEG-Mal) (Nanocs), PBS pH 7.4 1X (Fisher Scientific), Gadolinium-diethylenetriaminepentaacetic acid (Gd-DTPA) (Sigma), succinimidyl 3-(2-pyridyldithio) propionate (SPDP) (Fisher Scientific), dithiolthreitol (DTT) (Fisher Scientific), G.E. MidiTrap G-25 columns (Sigma), Millipore Pellican Biomax-100 ultrafiltration (Sigma) were purchased from the indicated vendors. All peptides were synthesized by Biopeptides, Inc. Female Sprague-Dawley Rats with a mean weight of 220 g were purchased through the UCSD animal care facility. Isoflurane (Sigma), Tissue-Plus O.C.T. (Fisher Scientific), Heparin (Sigma), and Fatal-Plus were acquired through the UCSD controlled substances system.

Nanoworm Synthesis: NWs were synthesized as previously described [13, 20, 21], in summary, all solutions were cooled to between 4-6 °C and maintained under nitrogen, 0.12 mol ferric chloride hexahydrate in 0.5mL deionized H_2O (dH_2O) was added to 0.17 mol of 20K MW dextran in 9 mL dH_2O, followed by the addition of 0.06mol ferrous chloride tetrahydrate in 0.5 mL dH_2O, pH adjusted with 30% NH_4OH to ~pH 8, heated slowly to 75 ^oC over 1 hr followed by 75 ^oC for 75 min. The product was cooled to room temperature and filtered successively from 0.45 µm, 0.22 µm to 0.1 µm with syringe filters, followed by purification with Millipore Pellicon Biomax-100 ultrafiltration cassette using dH_2O until neutral pH was reached with a final volume of 10mL. The particles were then added to 50 mL 5N NaOH with 0.25 mL epichlorohydrin for crosslinking overnight, purified again with ultrafiltration to 10mL final volume, and aminated with the slow addition of 0.2 mL concentrated ammonium hydroxide, stirring for 24 h. The resulting particles were again purified with ultrafiltration to a 10mL final volume and filtered to 0.1 µm with a syringe filter and purified with a Sephadex G-25 size exclusion column. This resulted in a filamentous nanoparticle with a mean size distribution of ~100 nm. These particles were conjugated simultaneously to n-succinimidyl ester (NHS) cyanine-7 (Cy-7) conjugate and a heterobifunctional polyethylene glycol (NHS-PEG-maleimide) at 10X the iron concentration in a mol ratio of 2:1, followed by purification and the attachment of a targeting or control peptide *via* the terminal cysteine. The final peptide-Cy7-NWs were purified on a G-25 column in PBS at pH 7.4. The iron concentrations were determined by inductively coupled plasma optical emission spectroscopy (ICP-OES).

***In Vivo* Testing of Cy7-CREKA-Nanoworms:** All experiments in this study were performed in accordance with the guidelines established by the Institutional Animal Care and Use Committee at the University of California San Diego and the American Association for Accreditation of Laboratory Animal Care. Myocardial infarction (MI) were induced by occlusion-reperfusion surgery performed on female Sprague-Dawley rats [33, 34]. This is an established technique where, in brief, the left coronary artery is sutured closed for 25 min after which the suture is released, thus simulating an MI followed by reperfusion (i.e. angioplasty/stent). The animals were anaesthetized by nose cone isoflurane administration during all intravenous (IV) injections. 48 h after surgery the rats were IV injected with NWs at 2.0 mg/kg Fe for fluorescent imaging and 0.4 mg/kg Fe for MRI imaging through the tail vein, followed by 6 h of circulation. The animals were sacrificed with an intraperitoneal (IP) injection of Fatal-Plus. For T2 with T1-weighted MRI imaging the following series of injections were used: IV injection of NWs 0.4 mg/kg Fe with a 6 h circulation time, after which an IP injection of 200 µL of a 120mg/mL solution of Gd-DPTA in PBS pH 7.4 immediately prior to euthanasia.

Imaging: All imaging was performed on organs *ex vivo*. To avoid any freeze/thaw or prolonged storage effects all tissues were placed in PBS pH 7.4, stored on dry ice and imaged within 4 h for fluorescence using a G.E. *eXplore* Optix fluorescence system with a power setting of 800 and 1 mm resolution, using a Cy7 specific laser excitation wavelength and corresponding emission filter. Directly after fluorescence imaging the hearts were either embedded in Tissue-Plus optimum cutting temperature (O.C.T.) compound and fresh frozen or imaged with 7T MRI within 8 h of sacrifice, followed by embedding in O.C.T. MR imaging was performed using a 7T

Bruker scanner at the UCSD Center for Functional MRI (fMRI). The following scan parameters were used: rapid acquisition with relaxation enhancement (RARE), T2 :TE 16.8 ms, TR 3.0 s and T1 : TE 11.7 ms, TR 0.9 s. Transmission electron microscopy (TEM) was performed on a 120kV FEI SPIRIT. Dynamic light scattering (DLS) was data collected with a Malvern Zetasizer Nano.

Histology: Hearts were cryosectioned into 10 µm slices. Sections were hematoxylin and eosin (H&E) stained to confirm the presence of MI in each heart. Adjacent sections were imaged using a Nikon upright fluorescent microscope with Cy7 filter cube, 750 nm excitation filter and 773 nm emission filter, equipped with an infrared camera. DAPI stain was used to visualize nuclei.

Hemocompatibility: Testing was performed by the UCSD Murine Hematology and Coagulation Core Laboratory on a ST4 semi-automated mechanical coagulation instrument, Diagnostica Stago, NJ, using established protocols. CREKA-NWs and NWs alone were diluted in PBS pH 7.4 run at a final concentration of 0.026mg/mL, 0.052 mg/mL and 0.260 mg/mL against PBS and human normal plasma controls. The testing concentrations were based on the estimated blood pool concentration of NWs *in vivo*; 200 µL of 2.2 mg/mL Fe NWs and 17 mL average blood volume for a 220 g female Sprague-Dawley rat [35].

Statistical Analysis: Statistical analyses were performed using G*Power [36]. Data were analyzed *post hoc* using a two tailed t-test difference between independent means.

3.4 Results and Discussion.

The iron oxide NWs were synthesized and conjugated to the fibrin-targeting peptide CREKA and the near IR fluorophore Cyanine 7 (Cy7) as outlined in Scheme 1. The NWs exhibited a hydrodynamic diameter of 92.5 nm, with SD +/- 5.11 nm (n = 3) by dynamic light scattering, and transmission electron microscopy confirmed the nanoworm morphology, (**Figure 3.1A-B**). The CREKA-Cy7-NWs were initially tested for targeting *ex vivo* on heart tissue sections harvested from rats euthanized 48 h post-ischemia reperfusion surgery (**Figure 3.2C-D**). Fluorescence imaging confirmed that the CREKA-Cy7-NWs specifically targeted regions of infarction, and this was verified by hematoxylin and eosin (H&E) staining; the infarction is indicated in Figure 3.1C-D by dark red staining areas of fibrin deposition and high nuclei density associated with acute inflammation.

To address the potential concern CREKA-NWs could induce clotting due to their fibrin binding properties, NWs with and without CREKA were subjected to hemocompatibility testing, (**Table 3.1**) [22, 37]. Both the NWs alone and CREKA-NWs did not show significant procoagulant or anticoagulant properties in human plasma when compared to PBS control at 1X, 2X and 10X the concentration of 26 μg/mL Fe, Table S1. The range of Fe concentrations tested was determined by estimation of the concentration that would result from injection of a rat (blood volume of 17 mL [35]) with a 200 μL dose of NWs containing 2.2 mg/mL Fe. This dose corresponds to an injection of 1.8 mg of NWs per kg of animal body mass.

The efficacy of CREKA targeting was next evaluated *in vivo* in a rat MI model. Here we used the Cy7 fluorescent label, (**Figure 3.2**), to follow the fate of the nanoparticles *in vivo*. A 200 µL dose consisting of either CREKA-Cy7-NWs, KAKEC-Cy7-NWs control, or PBS control were injected *via* the tail vein of rats 48 h after having undergone ischemia reperfusion surgery. The total Fe content in the NW injections was 0.44mg. After six h of circulation the rats were euthanized, and their organs were harvested and imaged with an *eXplore* Optix imaging system, (**Figure 3.3A-E**). Cross-sections were H&E stained to confirm the presence of MI in each heart (Figure 2A-B). The PBS and KAKEC-Cy7-NWs controls showed little observable fluorescence above tissue background whereas the CREKA-Cy7-NW hearts had high signal at the location of MI, confirming specific targeting of the CREKA species, (**Figure 3.3A-D**). CREKA-Cy7-NWs were also injected into a non-infarct control rat to test for non-specific binding, resulting in no significant fluorescence signal, (Figure 2C). The heart, spleen, kidneys, lungs and liver were imaged for each animal, both to confirm the tail vein injections had properly delivered the dose and to observe the biodistribution, (**Figure 3.3E**), where the tissue fluorescence presented in the Figure is representative of all animals tested. The highest degree of fluorescence was observed in the spleen and liver, as is typical for ~100 nm nanoparticles [38]. Heart sections imaged by fluorescence microscopy and compared to adjacent H&E-stained sections supported the hypothesis that the CREKA-modified NWs selectively home to the infarcted tissues *in vivo*, (**Figure 3.3F**). Cumulative data from *ex vivo* fluorescence imaging of excised hearts with CREKA-Cy7-NWs (n = 13) or KAKEC-Cy7-NWs (n = 10) with background subtraction using PBS injection controls showed significant targeting of CREKA (signal ± SD = 43.4 ± 5.7 vs 16.8 ± 14.7 for CREKA vs KAKEC, p = 0.001, (**Figure 3.3G**). These animals were randomly selected after infarct surgery

to avoid infarct size bias. After *ex vivo* fluorescence imaging, the rat hearts were imaged with a 7 Tesla (7T) Bruker MRI system. The 7T magnetic field yields a higher resolution, when compared to the 1.5T or 3T typically used for human imaging. Using a T2-weighted rapid acquisition with relaxation enhancement (RARE) pulse sequence with relaxation time (TR) of 3s and echo time (TE) of 16.8 ms, dark contrast was observed within hearts of the CREKA-Cy7-NW-injected animals (**Figure 3.4A**). The contrast was seen through successive images, and it was co-localized with infarct myocardium as confirmed by H&E staining (**Figure 3.4A-B**), and the presence of fibrin (**Figure 3.4C**). No negative contrast was observed in the KAKEC-Cy7-NW non-targeting peptide control animals (**Figure 3.4D-F**). These data confirm the *in vivo* targeting of NWs to fibrin within the infarcted myocardium.

Finally, we sought to determine if MR imaging of both CREKA-Cy7-NWs and Gd-DPTA could be used to enhance the ability to image fibrin in the context of a total infarct. For this set of experiments, 0.2mmol kg $^{-1}$ Gd-DTPA was co-injected IP with heparin-pentobarbital 6h after IV injection of peptide-Cy7-NWs. This allowed for the slow uptake of Gd-DTPA and blood saturation at the time of death, where an IV injection would be cleared too rapidly from the blood stream to be imaged post-mortem. T1-weighted imaging was performed using a RARE sequence with a TE of 11.7 ms and TR of 0.9 s and T2-weighted imaging with the same parameters as previously indicated. Within the hearts of the CREKA-Cy7-NW injected animals, negative contrast can be seen with T2-weighted imaging and a region of positive contrast can be seen corresponding to the total infarct region with T1-weighted imaging, as confirmed by H&E staining (**Figure 3.5A**). The KAKEC-Cy7-NW control exhibited no negative contrast in the

infarct region of the T2-weighted images and positive contrast in the T1-weighted images corresponding to the infarct as confirmed by H&E staining (**Figure 3.5B**). The band of negative contrast within the CREKA-Cy7-NWs co-localized with the band of fibrin, stained bright red in the H&E sections, supporting the fibrin specificity for the CREKA-Cy7-NWs (**Figure 3.5A**). The region of positive contrast visible in the infarct of the T2-weighted images is an artifact from the presence of Gd-DTPA; the positive contrast is absent in CREKA-Cy7-NWs (-) Gd-DTPA control heart (**Figure 3.6**). Thus, the combination of T1 and T2 imaging provides a temporal window into fibrin formation within infarcted myocardium.

3.5 Conclusions

Magnetic resonance imaging of myocardial fibrin deposition in early stages of ventricular remodeling by combining T2-responsive targeted nanoworms with T1-responsive Gd-DTPA provides a complementary source of information in molecular imaging. The CREKA-NW GD-DTPA MRI dual imaging system demonstrates the potential for simultaneous monitoring of the changes in fibrin and total infarct volume over the course of the healing process, and this concept may also be applicable to probing other molecular changes of scientific or clinical interest.

Acknowledgements

Chapter 3 is currently being prepared for submission for publication of the material. Grondek, J.F., Huffman, K., Cavichini, M., Warter, A., Kalaw, F.G.P., Lee, E.J., Fan, R., Cheng, L., Freeman, W.R., and Sailor, M.J., Treatment of Retinal Neovascularization in a Rabbit Model with a Fusogenic Porous Silicon Nanoparticle Containing Vascular Endothelial Growth Factor siRNA. The dissertation author was the primary researcher and author of this material.

3.6 References

1. Virani, S.S., A. Alonso, E.J. Benjamin, M.S. Bittencourt, C.W. Callaway, A.P. Carson, A.M. Chamberlain, A.R. Chang, S. Cheng, F.N. Delling, L. Djousse, M.S.V. Elkind, J.F. Ferguson, M. Fornage, S.S. Khan, B.M. Kissela, K.L. Knutson, T.W. Kwan, D.T. Lackland, T.T. Lewis, J.H. Lichtman, C.T. Longenecker, M.S. Loop, P.L. Lutsey, S.S. Martin, K. Matsushita, A.E. Moran, M.E. Mussolino, A.M. Perak, W.D. Rosamond, G.A. Roth, U.K.A. Sampson, G.M. Satou, E.B. Schroeder, S.H. Shah, C.M. Shay, N.L. Spartano, A. Stokes, D.L. Tirschwell, L.B. VanWagner, C.W. Tsao, E. American Heart Association Council on, C. Prevention Statistics, and S. Stroke Statistics, *Heart Disease and Stroke Statistics-2020 Update: A Report From the American Heart Association.* Circulation, 2020. **141**(9): p. e139-e596.

2. Frangogiannis, N.G., *The mechanistic basis of infarct healing.* Antioxid Redox Signal, 2006. **8**(11-12): p. 1907-39.

3. Rauch, U., *Tissue factor and cardiomyocytes.* Thromb Res, 2012. **129 Suppl 2**: p. S41-3.

4. Saraste, A., S. Nekolla, and M. Schwaiger, *Contrast-enhanced magnetic resonance imaging in the assessment of myocardial infarction and viability.* J Nucl Cardiol, 2008. **15**(1): p. 105-17.

5. Pennell, D.J., *Cardiovascular magnetic resonance.* Circulation, 2010. **121**(5): p. 692-705.

6. Hyeon, T., S.S. Lee, J. Park, Y. Chung, and H.B. Na, *Synthesis of highly crystalline and monodisperse maghemite nanocrystallites without a size-selection process.* J Am Chem Soc, 2001. **123**(51): p. 12798-801.

7. Sun, S. and H. Zeng, *Size-controlled synthesis of magnetite nanoparticles.* J Am Chem Soc, 2002. **124**(28): p. 8204-5.

8. Park, J., K. An, Y. Hwang, J.G. Park, H.J. Noh, J.Y. Kim, J.H. Park, N.M. Hwang, and T. Hyeon, *Ultra-large-scale syntheses of monodisperse nanocrystals.* Nat Mater, 2004. **3**(12): p. 891-5.

9. Dadfar, S.M., K. Roemhild, N.I. Drude, S. von Stillfried, R. Knuchel, F. Kiessling, and T. Lammers, *Iron oxide nanoparticles: Diagnostic, therapeutic and theranostic applications.* Adv Drug Deliv Rev, 2019. **138**: p. 302-325.

10. Hasegawa, M. and S. Hokkoku, *Magnetic iron oxide-dextran complex and process for its production* in *USPTO*, USPTO, Editor. 1978, Meito Sangyo Kabushiki Kaisha: United States.

11. Park, J.H., G. von Maltzahn, L. Zhang, M.P. Schwartz, E. Ruoslahti, S.N. Bhatia, and M.J. Sailor, *Magnetic Iron Oxide Nanoworms for Tumor Targeting and Imaging.* Adv Mater, 2008. **20**(9): p. 1630-1635.

12. Gossuin, Y., S. Disch, Q.L. Vuong, P. Gillis, R.P. Hermann, J.H. Park, and M.J. Sailor, *NMR relaxation and magnetic properties of superparamagnetic nanoworms.* Contrast Media Mol Imaging, 2010. **5**(6): p. 318-22.

13. Park, J.H., G. von Maltzahn, L. Zhang, A.M. Derfus, D. Simberg, T.J. Harris, E. Ruoslahti, S.N. Bhatia, and M.J. Sailor, *Systematic surface engineering of magnetic nanoworms for in vivo tumor targeting.* Small, 2009. **5**(6): p. 694-700.

14. Hossaini Nasr, S., A. Tonson, M.H. El-Dakdouki, D.C. Zhu, D. Agnew, R. Wiseman, C. Qian, and X. Huang, *Effects of Nanoprobe Morphology on Cellular Binding and Inflammatory Responses: Hyaluronan-Conjugated Magnetic Nanoworms for Magnetic Resonance Imaging of Atherosclerotic Plaques.* ACS Appl Mater Interfaces, 2018. **10**(14): p. 11495-11507.

15. Weissleder, R., A.S. Lee, B.A. Khaw, T. Shen, and T.J. Brady, *Antimyosin-labeled monocrystalline iron oxide allows detection of myocardial infarct: MR antibody imaging.* Radiology, 1992. **182**(2): p. 381-5.

16. Sosnovik, D.E., E.A. Schellenberger, M. Nahrendorf, M.S. Novikov, T. Matsui, G. Dai, F. Reynolds, L. Grazette, A. Rosenzweig, R. Weissleder, and L. Josephson, *Magnetic resonance imaging of cardiomyocyte apoptosis with a novel magneto-optical nanoparticle.* Magn Reson Med, 2005. **54**(3): p. 718-24.

17. Sosnovik, D.E., E. Garanger, E. Aikawa, M. Nahrendorf, J.L. Figuiredo, G. Dai, F. Reynolds, A. Rosenzweig, R. Weissleder, and L. Josephson, *Molecular MRI of cardiomyocyte apoptosis with simultaneous delayed-enhancement MRI distinguishes apoptotic and necrotic myocytes in vivo: potential for midmyocardial salvage in acute ischemia.* Circ Cardiovasc Imaging, 2009. **2**(6): p. 460-7.

18. Helm, P.A., P. Caravan, B.A. French, V. Jacques, L. Shen, Y. Xu, R.J. Beyers, R.J. Roy, C.M. Kramer, and F.H. Epstein, *Postinfarction myocardial scarring in mice: molecular MR imaging with use of a collagen-targeting contrast agent.* Radiology, 2008. **247**(3): p. 788-96.

19. Wildgruber, M., I. Bielicki, M. Aichler, K. Kosanke, A. Feuchtinger, M. Settles, D.C. Onthank, R.R. Cesati, S.P. Robinson, A.M. Huber, E.J. Rummeny, A.K. Walch, and R.M. Botnar, *Assessment of myocardial infarction and postinfarction scar remodeling with an elastin-specific magnetic resonance agent.* Circ Cardiovasc Imaging, 2014. **7**(2): p. 321-9.

20. Park, J.H., et al., *Magnetic Iron Oxide Nanoworms for Tumor Targeting and Imaging.* Advanced Materials, 2008. **20**: p. 1630–1635.

21. Palmacci, S. and L. Josephson, *Synthesis of polysaccharide covered superparamagnetic oxide colloids* in *USPTO*, USPTO, Editor. 1993, Advanced Magnetics, Inc.: United States.

22. Simberg, D., T. Duza, J.H. Park, M. Essler, J. Pilch, L. Zhang, A.M. Derfus, M. Yang, R.M. Hoffman, S. Bhatia, M.J. Sailor, and E. Ruoslahti, *Biomimetic amplification of nanoparticle homing to tumors.* Proc Natl Acad Sci U S A, 2007. **104**(3): p. 932-6.

23. Peters, D., M. Kastantin, V.R. Kotamraju, P.P. Karmali, K. Gujraty, M. Tirrell, and E. Ruoslahti, *Targeting atherosclerosis by using modular, multifunctional micelles.* Proc Natl Acad Sci U S A, 2009. **106**(24): p. 9815-9.

24. Hamzah, J., V.R. Kotamraju, J.W. Seo, L. Agemy, V. Fogal, L.M. Mahakian, D. Peters, L. Roth, M.K. Gagnon, K.W. Ferrara, and E. Ruoslahti, *Specific penetration and accumulation of a homing peptide within atherosclerotic plaques of apolipoprotein E-deficient mice.* Proc Natl Acad Sci U S A, 2011. **108**(17): p. 7154-9.

25. Wen, A.M., Y. Wang, K. Jiang, G.C. Hsu, H. Gao, K.L. Lee, A.C. Yang, X. Yu, D.I. Simon, and N.F. Steinmetz, *Shaping bio-inspired nanotechnologies to target thrombosis for dual optical-magnetic resonance imaging.* J Mater Chem B, 2015. **3**(29): p. 6037-6045.

26. Poon, C., J. Gallo, J. Joo, T. Chang, M. Banobre-Lopez, and E.J. Chung, *Hybrid, metal oxide-peptide amphiphile micelles for molecular magnetic resonance imaging of atherosclerosis.* J Nanobiotechnology, 2018. **16**(1): p. 92.

27. Deshpande, D., S. Kethireddy, F. Gattacceca, and M. Amiji, *Comparative pharmacokinetics and tissue distribution analysis of systemically administered 17-beta-estradiol and its metabolites in vivo delivered using a cationic nanoemulsion or a peptide-modified nanoemulsion system for targeting atherosclerosis.* J Control Release, 2014. **180**: p. 117-24.

28. Yoo, S.P., F. Pineda, J.C. Barrett, C. Poon, M. Tirrell, and E.J. Chung, *Gadolinium-Functionalized Peptide Amphiphile Micelles for Multimodal Imaging of Atherosclerotic Lesions.* ACS Omega, 2016. **1**(5): p. 996-1003.

29. Song, Y., Z. Huang, J. Xu, D. Ren, Y. Wang, X. Zheng, Y. Shen, L. Wang, H. Gao, J. Hou, Z. Pang, J. Qian, and J. Ge, *Multimodal SPION-CREKA peptide based agents for molecular imaging of microthrombus in a rat myocardial ischemia-reperfusion model.* Biomaterials, 2014. **35**(9): p. 2961-70.

30. Gormley, C.A., B.J. Keenan, J.A. Buczek-Thomas, A. Pessoa, J. Xu, F. Monti, P. Tabeling, R.G. Holt, J.O. Nagy, and J.Y. Wong, *Fibrin-Targeted Polymerized Shell Microbubbles as Potential Theranostic Agents for Surgical Adhesions.* Langmuir, 2019. **35**(31): p. 10061-10067.

31. Huang, Z., Y. Song, Z. Pang, B. Zhang, H. Yang, H. Shi, J. Chen, H. Gong, J. Qian, and J. Ge, *Targeted delivery of thymosin beta 4 to the injured myocardium using CREKA-conjugated nanoparticles.* Int J Nanomedicine, 2017. **12**: p. 3023-3036.

32. Chen, J., Y. Song, Z. Huang, N. Zhang, X. Xie, X. Liu, H. Yang, Q. Wang, M. Li, Q. Li, H. Gong, J. Qian, Z. Pang, and J. Ge, *Modification with CREKA Improves Cell Retention in a Rat Model of Myocardial Ischemia Reperfusion.* Stem Cells, 2019. **37**(5): p. 663-676.

33. Huang, N.F., R.E. Sievers, J.S. Park, Q. Fang, S. Li, and R.J. Lee, *A rodent model of myocardial infarction for testing the efficacy of cells and polymers for myocardial reconstruction.* Nat Protoc, 2006. **1**(3): p. 1596-609.

34. Singelyn, J.M., P. Sundaramurthy, T.D. Johnson, P.J. Schup-Magoffin, D.P. Hu, D.M. Faulk, J. Wang, K.M. Mayle, K. Bartels, M. Salvatore, A.M. Kinsey, A.N. Demaria, N. Dib, and K.L. Christman, *Catheter-deliverable hydrogel derived from decellularized ventricular extracellular matrix increases endogenous cardiomyocytes and preserves cardiac function post-myocardial infarction.* J Am Coll Cardiol, 2012. **59**(8): p. 751-63.

35. Probst, R.J., J.M. Lim, D.N. Bird, G.L. Pole, A.K. Sato, and J.R. Claybaugh, *Gender differences in the blood volume of conscious Sprague-Dawley rats.* J Am Assoc Lab Anim Sci, 2006. **45**(2): p. 49-52.

36. Faul, F., E. Erdfelder, A.G. Lang, and A. Buchner, *G*Power 3: A flexible statistical power analysis program for the social, behavioral, and biomedical sciences.* Behavior Research Methods, 2007. **39**(2): p. 175-191.

37. Simberg, D., W.M. Zhang, S. Merkulov, K. McCrae, J.H. Park, M.J. Sailor, and E. Ruoslahti, *Contact activation of kallikrein-kinin system by superparamagnetic iron oxide nanoparticles in vitro and in vivo.* J Control Release, 2009. **140**(3): p. 301-5.

38. Moghimi, S.M., A.C. Hunter, and J.C. Murray, *Long-circulating and target-specific nanoparticles: theory to practice.* Pharmacol Rev, 2001. **53**(2): p. 283-318.

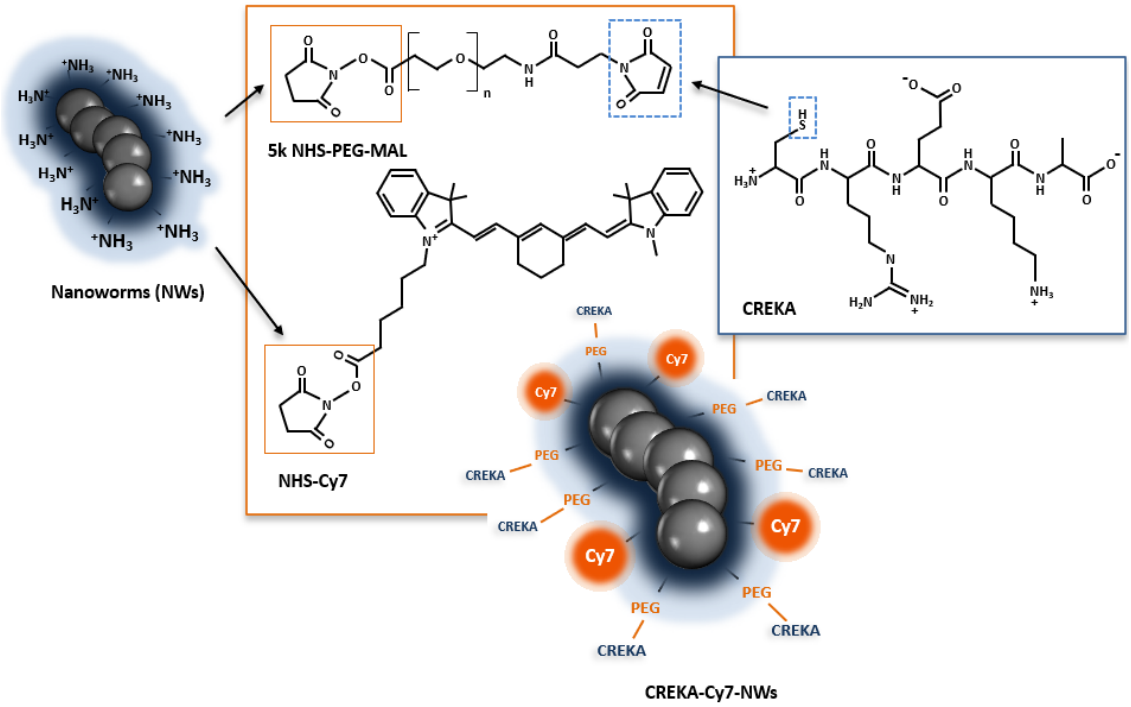

Figure 3.1. Chemistry used in this study to attach the Cy7 fluorophore and targeting peptides to iron oxide nanoworms (NWs). **A.** Dextran-coated superparamagnetic iron oxide nanoworms display a highly positive amine surface chemistry after crosslinking with epichlorohydrin and subsequent amination with ammonium hydroxide. To these surface amines, NHS ester chemistry is used to simultaneously attach **B.** N-succinimidyl ester (NHS)-5K MW poly(ethylene glycol)-maleimide and **C.** NHS-Cy7 fluorophore. **D.** The pendant maleimide on the linker from **B.** is conjugated to the thiol on the N-terminal cysteine of the CREKA peptide (or to the C-terminal cysteine on the KAKEC control peptide, not shown). **E.** The resulting CREKA-Cy7 FeO NWs.

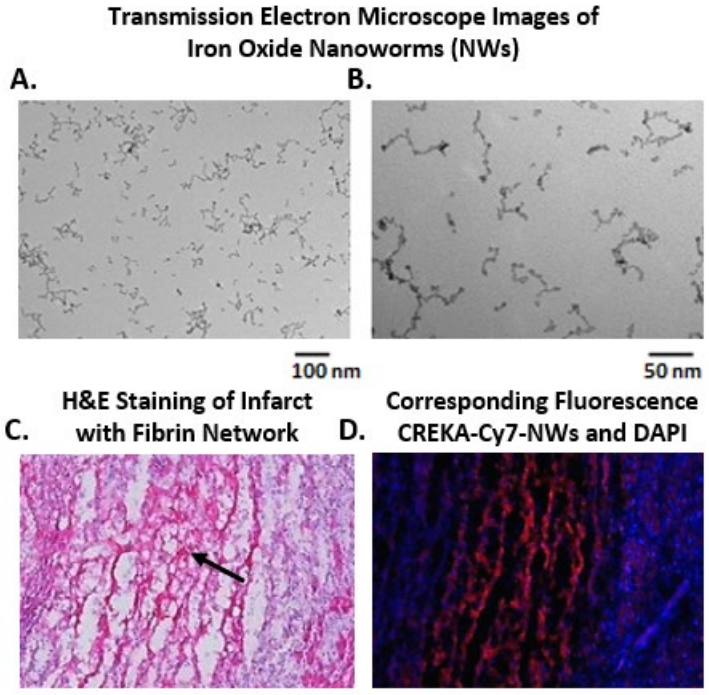

Figure 3.2. Transmission electron microscope (TEM) images of the iron oxide nanoworms (NWs) used in this study: **A.** 25k X magnification and **B.** 60k X magnification, and fluorescence microscopy data evaluating *ex vivo* targeting of NWs conjugated with Cy7-CREKA and incubated on sections of infarcted rat hearts. **C.** H&E staining of sectioned heart at 5 X magnification. Arrow indicates region of fibrin which stains a darker red than the surrounding tissue. **D.** Corresponding fluorescence images showing Cy7 fluorescence (red) and DAPI (blue) at 5 X magnification.

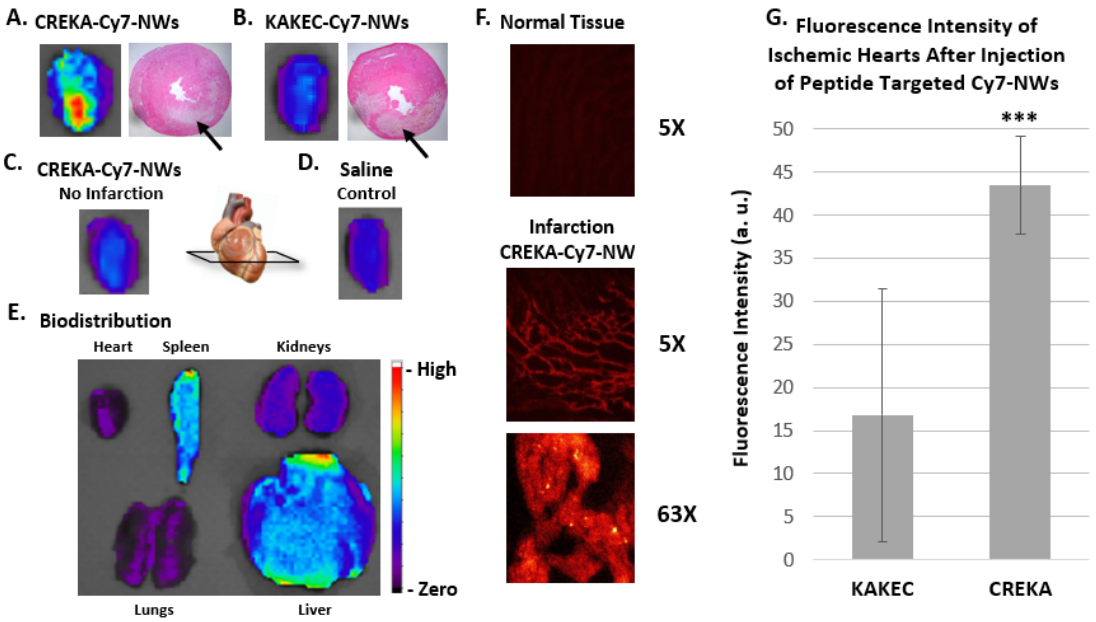

Figure 3.3. Nanoworm (NW) targeting of myocardial infarction in rats. *Ex vivo* fluorescence imaging of excised hearts with Cy7-NWs conjugated to **A.** CREKA, **B.** KAKEC peptide control, **C.** CREKA (no infarction), and **D.** Saline control. **A.** and **B.** show H&E staining of heart sections of the same hearts confirming infarction, indicated by the black arrows in each inset. **E.** Representative major organ biodistribution of the peptide-Cy7-NWs. The highest level of fluorescence was seen in the spleen and liver. **F.** Fluorescence microscope images (Cy7 channel) of heart sections adjacent to the H&E sections showing normal tissue autofluorescence control at 5 X magnification and infarcted tissue with *in vivo* targeted CREKA-Cy7-NWs at 5 X and 63 X magnification **G.** *Ex vivo* fluorescence imaging of excised hearts with Cy7-NWs conjugated to CREKA (n = 13) or KAKEC peptide control (n = 10); Average intensity analysis from ImageJ, the error bars represent standard deviation; ***p = 0.001

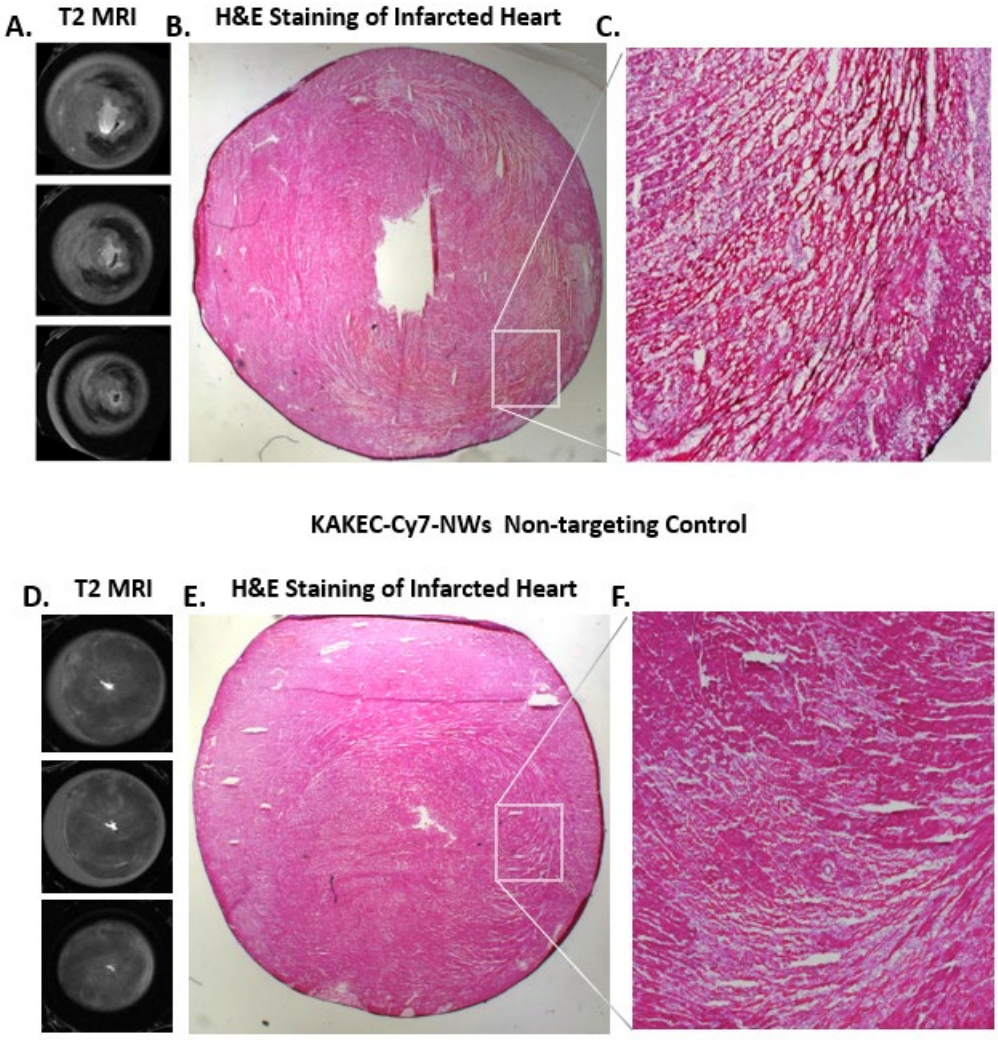

Figure 3.4. Nanoworm (NW) targeting of myocardial infarction in rats. **A.** T2 RARE MRI images of a heart with CREKA-NWs, shown as negative contrast, with successive images descending toward the apex, **B.** H&E staining of the heart from **A.** showing an infarct pattern similar to the MRI negative contrast, and **C.** a magnified image of **B.** showing the presence of fibrin (dark red) within the infarct region. **D-F.** show MRI images and histology with KAKEC-NW control peptide.

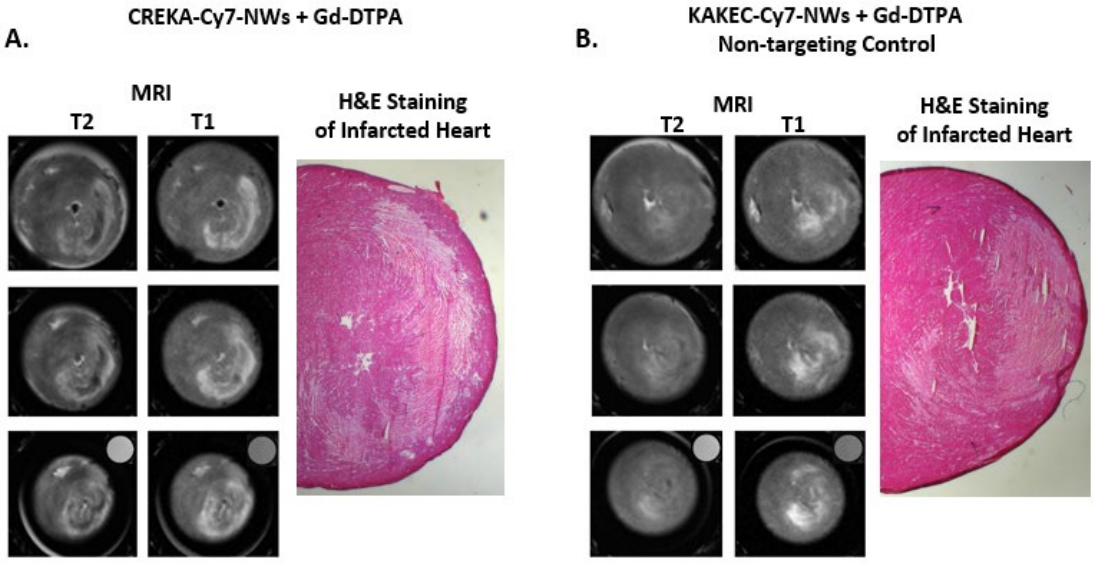

Figure 3.5. *In vivo* nanoworm (NW) targeting of myocardial infarction in rats with Gd-DTPA enhancement. **A.** RARE T2 and T1 MRI images of a heart with CREKA-NWs, shown as negative contrast in the T2 images and passive accumulation of Gd-DTPA shown as positive contrast in the T1 image set with successive images descending toward the apex; with H&E staining of the heart the adjacent heart showing an infarct pattern similar to the MRI positive contrast. **B.** Control experiment, similar to **A.**, but using control KAKEC-NWs. The circular insets are an internal contrast control containing PBS.

Table 3.1. Hemocompatibility of CREKA-Nanoworms (NWs). Clotting time, in seconds, testing NWs with and without pendant CREKA using the intrinsic, activated particle thromboplastin, and extrinsic, prothrombin, clotting cascades. (*) Concentrations are based on the in vivo injection of 200µL of 2.2mg/mL Fe divided by the estimated average 220g Sprague-Dawley rat blood volume of 17mL. Data collected using ST4 semi-automated mechanical coagulation instrument.

Table S3.1. CREKA-Nanoworms Hemocompatibility Testing

			Activated Partial Thromboplastin Coagulation Time (sec)			Prothrombin Coagulation Time (sec)		
			aPTT			PT		
			duplicates		mean	duplicates		mean
		Human Plasma	31.0	30.7	30.9	11.7	12.0	11.9
		PBS control	33.7	33.7	33.7	12.2	12.2	12.2
Fe* (ug/ml)	Relative Conc.							
26	1X	NWs	33.5	33.8	33.7	11.8	12.0	11.9
52	2X	NWs	33.6	33.1	33.4	12.6	12.2	12.4
260	10X	NWs	34.7	35.0	34.9	12.5	12.8	12.7
26	1X	CREKA-NWs	32.2	32.7	32.5	11.9	12.1	12.0
52	2X	CREKA-NWs	32.7	32.5	32.6	11.9	12.2	12.1
260	10X	CREKA-NWs	31.7	32.2	32.0	11.8	12.2	12.0

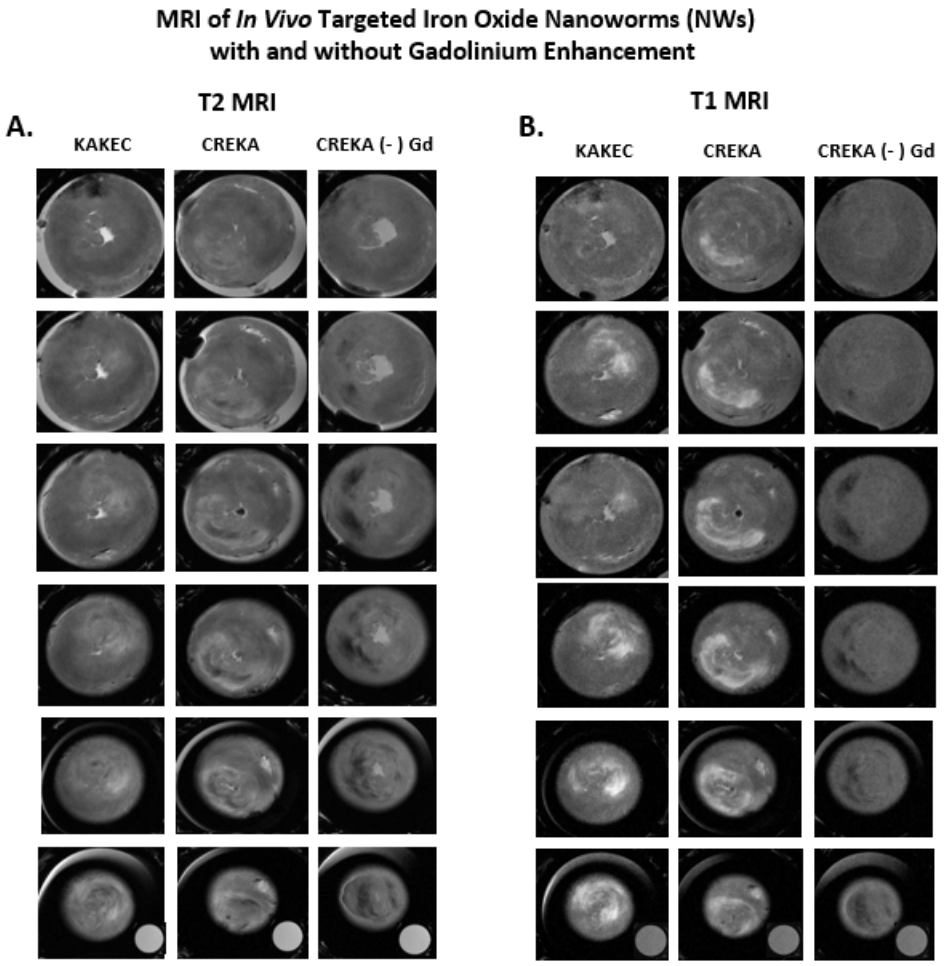

Figure 3.6. *In vivo* nanoworm (NW) targeting of myocardial infarction in Sprague-Dawley rats. **A.** T2 RARE MRI images of heart with CREKA-Cy7-NWs or KAKEC-Cy7-Control NWs shown as negative contrast and **B.** T1 RARE MRI images of passive accumulation of Gd-DTPA shown as positive contrast representing the total area of infarction. Successive images are descending toward the apex of the hearts. The circular insets are an internal contrast control containing PBS and run with each experiment.